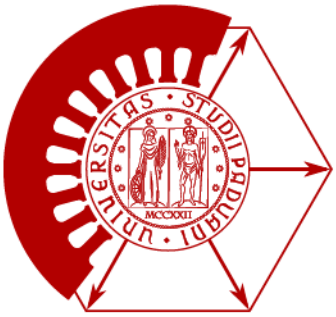

UNIVERSITY OF PADOVA

Department of Industrial Engineering

PhD School of Industrial Engineering
Electrical Energy Engineering
Cycle XXXI

High Performance Synchronous Reluctance Machines: Design and Applications

Director of Ph.D. school:
Prof. Paolo Colombo

Curriculum coordinator:
Prof. Roberto Turri

Supervisor:
Prof. Nicola Bianchi

Ph.D. candidate: **Yawei Wang**

30 Sept. 2018

Contents

Preface

This Preface describes the background and motivation of the thesis. The contents of each Chapter are briefly summarized. Finally, a list of publications during the Ph.D. period is reported.

Background

As one of the oldest machine topologies, the concept of synchronous reluctance (REL) machine can be traced back as early as 1900s. During the last century, remarkable progress had been made in the development of REL machines. In the last 20 years, particularly, the REL machines have attracted more and more attention in both academic and industrial fields. Without permanent magnets and rotor bars, the rotor construction of the REL machine is more robust than either permanent magnet (PM) machines or induction machines (IMs). In addition, it achieves the merits of low cost, low maintenance, and high reliability. All these features reveal the REL machine to be an attractive alternative to the widely used machine topologies. Therefore, the investigation of REL machines is essential, and specific applications will be of great interest.

In particular, the design of the REL machine will be focused on electric vehicle (EV) applications. It is remarkable that the popularity of EVs and hybrid electric vehicles (HEVs) is expanding significantly in the last decade. The electric motor, being one of the key devices, determines the main performance of the electrical mobility. Among various machine topologies, the interior permanent magnet (IPM) motor has been recognized as the most promising candidate. It accounts for over 80 % of EV and HEV markets at present, and even a higher percentage is expected in the near future. On the other hand, some challenges are related to IPM motors, i.e., high production cost, vulnerability to short-circuit fault, high back electromagnetic force (EMF) at high speed and high risk of irreversible demagnetization. Most importantly, a worldwide concern about the price volatility and availability of rare-earth magnets is growing. Therefore, many researchers are focused on investigating alternative non-rare-earth traction drives, and the REL machine is considered to be the substitute.

The second application is related to the self-excited synchronous reluctance generator (SERG) for isolated wind applications. In the last decades, wind energy is increasingly utilized around the world, and the demand of wind power systems grows rapidly. Among wind power generators, in particular, low power installations arouse

special interests recently, especially for applications in urban and remote areas. As is well known, PM generators and double-fed induction generators have been widely used as wind turbine generators. On the other hand, they are either too expensive or complicated, so that they are not suitable for small wind turbine generation systems. The squirrel-cage induction generator with capacitor excitation, known as self-excited induction generator (SEIG) seems very promising. It offers certain advantages, such as low cost, robustness, reduced size, absence of DC source for excitation and low maintenance requirements. However, the variable frequency affected by load and excitation capacitors makes the performance prediction quite difficult. Fortunately, the SERG has been demonstrated to provide an alternative solution. It has almost all the advantages of the SEIG and, in addition, the frequency is directly proportional to the rotor speed. In addition, it achieves very low rotor loss due to the absence of rotor bars. Therefore, further investigations on SERG are required from scientific point of view.

Aim of the research

The aim of this study will firstly discuss the design methodology of the REL machine. Detailed geometry analysis of the rotor structure will be provided, which aims to suggest an automatic drawing procedure. Such a procedure will be used to rapidly analyze the impact of some rotor parameters on the machine performance, in order to provide a guideline for the preliminary design of the REL machine. After that, as a practical example, a REL motor according to the dimension of a commercial motor will be designed. Certain design procedures will be followed, and optimization will also be carried out. The performance comparison between the optimized REL motor and the commercial product will be given. Merits and defects of the REL machine for EV application will be highlighted.

The study on SERG will start with the recognition of the steady-state performance, both analytically and experimentally. Then the conditions for the initial self-excitation process of SERG will be investigated. The possibility to adopt self-excited PM-assisted reluctance generator will also be dealt with, and the performance comparison with SERG will be made. Referring to wind applications, the method to maintain the generated voltage constant at variable speeds will be proposed. Finally, the prediction of the "optimal capacitor and resistor combination" that achieves the maximum utilization of the mechanical power produced by the wind turbine will be presented.

Outline of the thesis

Hereafter, the contents of each Chapter are briefly described:

Chapter 1 illustrates the development history, basic concepts, definitions and performance characteristics of the REL machines. In particular, the reason to choose TLA type REL machine with multiple flux-barriers is explained. The basic concept and equations of the PM-assisted reluctance (PMAREL) machine are also introduced, and the commonly adopted current control strategies are presented.

Chapter 2 provides a detailed parametric analysis of the rotor geometry for both REL and PMAREL machines, suggesting an automatic modeling and simulating procedure. Some useful equations are given, and the tuning steps are suggested in order to achieve the high performance design. The effects of some rotor parameters on the machine performance are also analyzed.

Chapter 3 proposes a design procedure to optimize the REL motor according to the dimension of Lexus LS 600h motor. An analytical calculation of slot area is innovatively derived to obtain the optimal split ratio, and differential evolution (DE) algorithm is used for rotor optimization. The performance comparison between the optimized REL motor and the interior permanent magnet (IPM) motor is then carried out. The performance improvements with PMs into the optimized REL rotor are also investigated.

Chapter 4 develops an analytical model for the steady-state operation of the SERG, considering no-load and resistive load conditions. Some experiments are carried out to verify the analytical results. Conditions to ensure a stable self-excitation process in SERG are investigated. The assisting of the PMs on the performance improvement of SERG is also discussed.

Chapter 5 proposes the method of active and reactive power (PQ) balances to predict the operating point of SERG, which considers the cross-saturation effect. The procedure to determine the values of capacitors for voltage regulation at variable speeds is presented. The prediction of the "optimal capacitor and resistor combination" that achieves the highest usage of wind power is also discussed.

List of publications

Several parts of this Ph.D. thesis have been presented by the author during his Ph.D. period in international conferences and journals. Hereafter the publications are listed in a chronological order:

- **Yawei Wang**, Giacomo Bacco, and Nicola Bianchi, "Geometry analysis and optimization of PM-assisted reluctance motors," in *2016 XXII International Conference on Electrical Machines (ICEM)*, Lausanne, Switzerland, Sept. 2016, pp. 1756-1762, DOI: 10.1109/ ICELMACH.2016.7732761.
- **Yawei Wang** and Nicola Bianchi, "Investigation of self-excitation in reluctance generators," in *2017 IEEE International Electric Machines Drives Conference (IEMDC)*, Miami, FL, USA, May 2017, DOI: 10.1109/IEMDC.2017.8002303.
- **Yawei Wang**, Nicola Bianchi, Silverio Bolognani, and Luigi Alberti, "Synchronous motors for traction applications," in *2017 International Conference of Electrical and Electronic Technologies for Automotive*, Turin, Italy, Jun. 2017, DOI: 10.23919/EETA.2017.7993210.
- **Yawei Wang**, Giacomo Bacco, and Nicola Bianchi, "Geometry analysis and optimization of PM-assisted reluctance motors," *IEEE Transactions on Industry Applications*, vol. 53, no. 5, pp. 4338-4347, Sept. 2017, DOI: 10.1109/TIA.2017.2702111.

- **Yawei Wang** and Nicola Bianchi, "Investigation of self-excited synchronous reluctance generators," *IEEE Transactions on Industry Applications*, vol. 54, no. 2, pp. 1360-1369, Mar. 2018, DOI: 10.1109/TIA.2017.2781645.
- **Yawei Wang** and Nicola Bianchi, "Analysis of self-excited PM-assisted reluctance generators," *IEEE Transactions on Energy Conversion*, vol. 33, no. 2, pp. 877-885, Mar. 2018, DOI: 10.1109/TEC.2017.2779044.
- **Yawei Wang**, Mattia Filippini, Giacomo Bacco, and Nicola Bianchi, "Parametric design and optimization of magnetic gears with differential evolution method," in *2018 IEEE XXIII International Conference on Electrical Machines (ICEM)*, Alexandroupoli, Greece, Sept. 2018, DOI: 10.1109/ICELMACH.2018.8507160.
- **Yawei Wang**, Mattia Filippini, Nicola Bianchi, and Piergiorgio Alotto, "A review on magnetic gears: topologies, computational models, and design aspects," in *2018 IEEE XXIII International Conference on Electrical Machines (ICEM)*, Alexandroupoli, Greece, Sept. 2018, DOI: 10.1109/ICELMACH.2018.8507204.
- **Yawei Wang** and Nicola Bianchi, "Modeling and investigation of self-excited reluctance generators for wind applications," in *2018 IEEE Energy Conversion Congress and Exposition (ECCE)*, Portland, USA, Sept. 2018.
- **Yawei Wang** and Nicola Bianchi, "Performance analysis of self-excited reluctance generating system using power balance," *IEEE Transactions on Energy Conversion*, **in press**, DOI: 10.1109/TEC.2018.2880835.

Chapter 1

Overview of REL Machines

Recently, the synchronous reluctance (REL) machines have attracted more and more attention in both academic and industrial fields. The purpose of this Chapter is to make an overview on REL machines, in terms of development history, basic concepts, definitions and performance characteristics. After that, a comparison among the classical REL rotor structures, namely salient-pole (SP) type, axially-laminated anisotropy (ALA) type and transversely-laminated anisotropy (TLA) type are carried out, highlighting the advantages of the TLA type with multiple flux-barriers. Finally, the basic concept and equations of the PM-assisted reluctance (PMAREL) machine are introduced, and the commonly adopted current control strategies are presented.

1.1. History of REL machines

THE concept of synchronous reluctance (REL) machine can be traced back as early as 20th century. Among the others, the REL motor with salient-pole (SP) rotor is one of the oldest types of electric machines, in which the wounded excitation coils are removed. Unlike the switched reluctance machines, SP type rotor operates synchronously with the stator frequency. Besides, rotating field exists in the SP type REL machine, which permits smooth torque and low noise.

During the last century, remarkable progress had been made in the development of REL machines. In 1923 [1], Kostko introduced a reluctance rotor construction, named reaction synchronous motor, with separated sections roughly along the lines of the direct field, which is shown in Fig. 1.1(a). This divided rotor conception substantially became the basis for the following rotor designs, and attracted the efforts of a considerable number of researches.

Latter on in 1966 [2], the axially-laminated anisotropy (ALA) rotor construction was proposed by Cruickshank, as shown in Fig. 1.1(b). In this case, the magnetic laminations are bent to produce high permeability paths in the direction of the laminations and low permeability paths normal to the laminations. It is verified to improve the REL machine performance by dramatically increasing the saliency ratio. The following investigations revealed that REL motors with the highest saliency ratio are obtained with the ALA

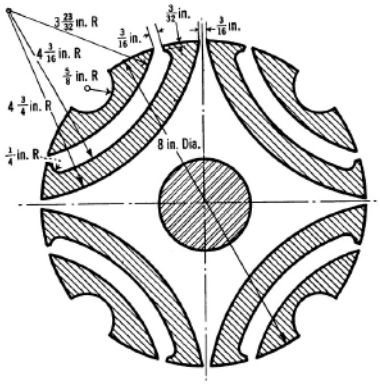

(a) Kostko's rotor in 1923 [1].

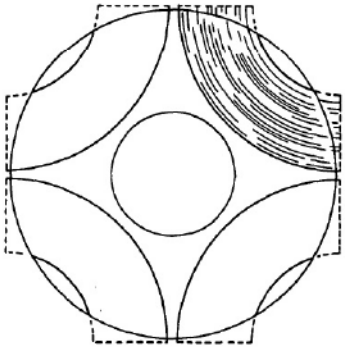

(b) Cruickshank's rotor in 1966 [2].

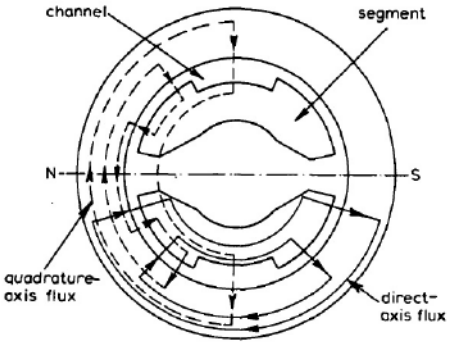

(c) Lawrenson's rotor in 1967 [7].

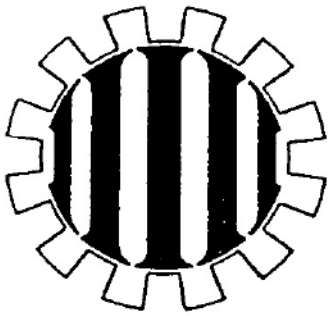

(d) Marongiu's rotor in 1991 [8].

Figure 1.1: Key development steps of REL machines.

designs [3–5]. The experimentally obtained saliency ratios are in the range of 10 to 21 [5, 6].

Almost at the same period, the segmental rotor, which is also called transversely-laminated anisotropy (TLA) rotor, was described by Lawrenson [7]. As shown in Fig. 1.1(c), the segments are made by magnetic laminations, providing the low reluctance paths. On the contrary, the high reluctance paths are blocked by the air part between segments. A single flux-barrier REL motor was designed by Miller [9], while the torque capability is quite low due to the poor anisotropy. In [8], it is suggested that "best" REL machine is a segmented one, with a limited number of segments per pole for the perspective of rotor iron losses. The resultant multiple-segment (or alternatively, multiple flux-barrier) rotor is shown in Fig. 1.1(d). This type of REL machines have been intensively studied in literature, and different flux-barrier shapes were proposed [10, 11].

With the development of REL technologies, the comparisons with induction machines (IMs) and permanent magnet (PM) machines are always of great interest [3, 12, 13]. Lipo [12] and Vagati [3] demonstrated, by means of analysis, that the REL machine may be capable of better torque production than the IM. It is concluded that the efficiency and power density of the REL machine are higher than that of IM, but the power factor is lower [10, 14]. For a precise performance comparison, each machine has to be separately designed, since the ratio of stator inner diameter to the outer diameter

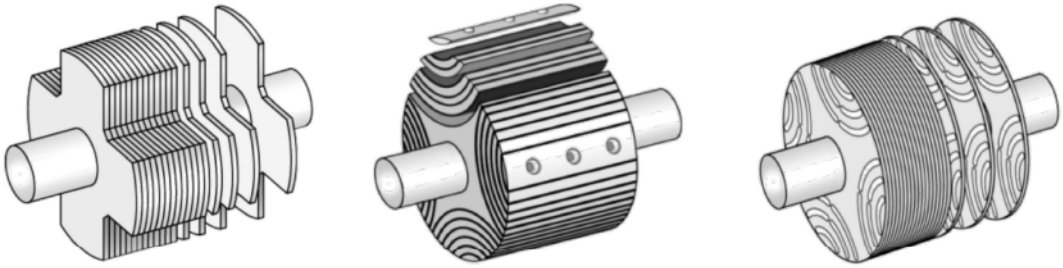

(a) Rotor structure with salient-pole.

(b) Axially laminated rotor structure.

(c) Transversely laminated rotor structure.

Figure 1.2: Main structures of the REL rotor.

can be quite different.

Vagati [8,15] and Kamper [14,16] made important contributions to the design aspects of REL machines. A mathematical modeling of a distributed anisotropy REL machine was proposed in [8], considering the slot effect. Simple mathematical equations were derived in [15], so as to introduce a general design approach. Effect of rotor dimensions and cross magnetization on L_d and L_q inductances of REL machines were investigated in [16]. The finite element analysis (FEA) method was used directly with optimization algorithms to achieve a multiple objective optimization of REL machine [14].

Some researchers are focused on the torque behavior of REL machines. An analytical model to predict torque behavior was proposed in [17], considering stator slotting and skewing effect. It is proved that skewing or using selected rotor steps can be adopted to reduce ripple but not completely. The selection of n_r, which refers to the equivalent distributed separation points along the rotor surface, has significant effect on torque ripple [18]. The n_r value to achieve the minimum torque ripple must be properly related to the n_s value, that is, to the number of stator slots per pole pair. Other methods to reduce the torque ripple, such as shifting the magnetic pole center of each pole [19], or using asymmetrical flux-barrier design [20], are also proposed.

During the last decade, some commercial productions of REL machines have been emerged. One of the most notable of these comes from ABB, initially in 2012. REL machines ratings ranging from 5.5 to 315 kW are now available for industrial applications [21]. Therefore, the investigation of REL machines is essential, and particular applications will be of great interest.

1.2. Basic concepts and definitions of REL machines

1.2.1. Machine structure

The stator of the REL machine is basically the same as that of IM or PM machines, which consists of iron laminations and phase windings. The windings are generally three-phase, properly distributed in order to produce a sinusoidal magneto motive force (MMF) in the airgap.

As aforementioned, the reluctance rotor can be classified into three types, namely SP type, ALA type and TLA type. The simplest one is the SP type, as shown in

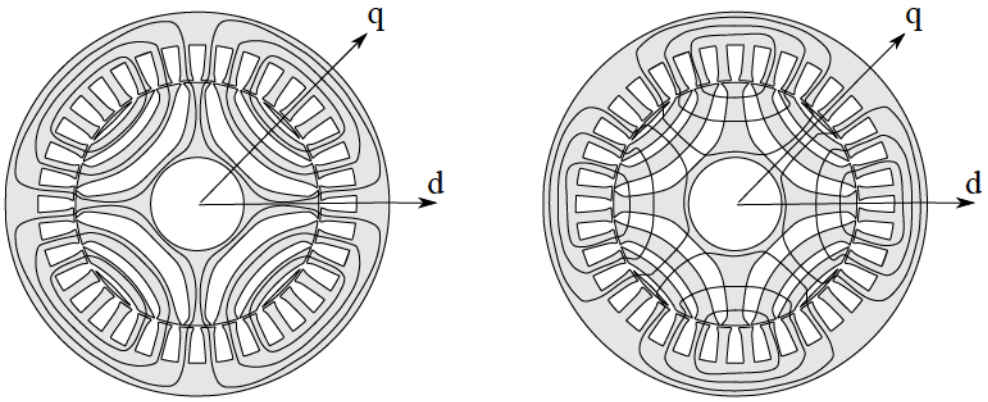

(a) d-axis flux lines. (b) q-axis flux lines.

Figure 1.3: Flux lines in d- and q-axis paths.

Fig. 1.2(a). This construction can be easily manufactured, while it is not suitable for high torque density. Detailed explanations will be given in Section 1.4.1. In addition, the SP type is related to the challenges of high torque ripple, high acoustic noise and vibration, due to the local saturation effect.

A typical ALA rotor construction is described in Fig. 1.2(b), where the silicon steel sheets are bent to be laminated in the axial direction. The iron laminations are separated by thin layers of insulating material. The pole holders are generally used to maintain the laminations. This type of rotor creates really high anisotropy. Unfortunately, this construction is vulnerable to elevate the iron losses in the rotor, limiting its efficiency advantages. More importantly, the significant manufacture complexity and difficulty in rotor skewing have seriously hindered its commercialization opportunities [22].

The TLA rotor (shown in Fig. 1.2(c)) is preferable, in practice, since it is suitable for industrial manufacturing. In this case, the rotor laminations can be punched as a whole, which is the same as the other traditional machines. In addition, the rotor can be easily skewed to reduce torque ripple. The flux-barrier shapes can be specially designed suitable for different applications. Therefore, only TLA type of REL machine is considered in this thesis.

1.2.2. Equivalent circuit model

Generally speaking, two distinct reference axes exist in most motors, the direct axis (d-axis) and the quadrature axis (q-axis). They are perpendicular in terms of electric degrees. In REL machines, particularly, the d-axis corresponds to the high permeability path, while the q-axis corresponds to the low permeability path. As an example, the d- and q-axis flux lines in different paths of a four-pole REL machine are shown in Fig. 1.3. The two axes are also identified in this figure.

According to the d-q reference frame, equations of the REL machine in the transient

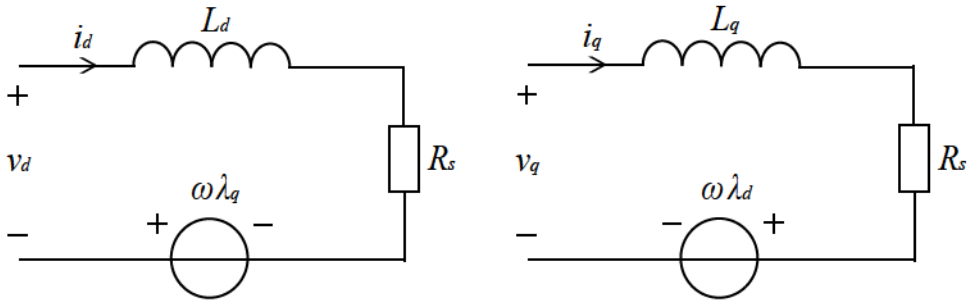

(a) d-axis circuit. (b) q-axis circuit.

Figure 1.4: Equivalent circuits of the REL machine in d-q reference frame.

state, neglecting iron losses, are given as

$$\begin{cases} v_d = R_s i_d + \dfrac{d\lambda_d}{dt} - \omega\lambda_q \\ v_q = R_s i_q + \dfrac{d\lambda_q}{dt} + \omega\lambda_d \end{cases} \tag{1.1}$$

$$\begin{cases} \lambda_d = L_d i_d \\ \lambda_q = L_q i_q \end{cases} \tag{1.2}$$

where v_d, v_q, λ_d, λ_q and i_d, i_q represent the d- and q-axis voltages, flux linkages and currents, respectively. R_s is the phase stator resistance, ω is the electrical angular speed. L_d and L_q represent the d- and q-axis apparent inductances. In REL machines, L_d and L_q vary with phase current due to different levels of saturation. Equations (1.1) are derived as

$$\begin{cases} v_d = R_s i_d + L_d \dfrac{di_d}{dt} - \omega L_q i_q \\ v_q = R_s i_q + L_q \dfrac{di_q}{dt} + \omega L_d i_d \end{cases} \tag{1.3}$$

This model is represented by the equivalent circuit shown in Fig. 1.4. The steady-state versions of these voltage equations can be easily extracted from (1.3) by setting time derivative terms to zero. Therefore, equations in (1.3) become

$$\begin{cases} V_d = R_s I_d - \omega L_q I_q \\ V_q = R_s I_q + \omega L_d I_d \end{cases} \tag{1.4}$$

where V_d, V_q and I_d, I_q represent the d- and q-axis voltages and currents in steady-state conditions.

The phasor diagram representative of the REL machine, neglecting stator resistance, is indicated in Fig. 1.5. φ represents the angle between the terminal voltage and current, α_i^e refers to as phase angle between the current and the d-axis (*i.e.*, current phase angle), and δ is the phase angle between the flux linkage and the d-axis. The d-axis current I_d is also called the "magnetizing" current, while the q-axis current I_q is called the "torque" current. The voltage vector leads the current vector of a quite large angle φ, which causes a low power factor in the REL motor, as will be discussed in the following.

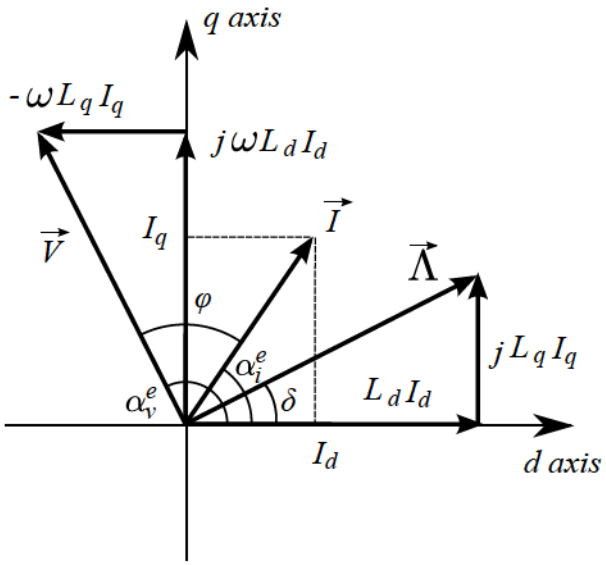

Figure 1.5: Phasor diagram representative of the REL machine.

1.3. REL machine performance analysis

1.3.1. Torque behavior

The *d*-*q* representation leads to the following general expression for the average torque developed in a REL machine:

$$T_{em} = \frac{3}{2}p(L_d - L_q)i_d i_q = \frac{3}{2}pL_q(\xi - 1)i_d i_q \tag{1.5}$$

where p is the number of pole-pairs. ξ is known as the "saliency ratio", which is one of the most important parameters in REL machines. It is defined as follows:

$$\xi = \frac{L_d}{L_q} \tag{1.6}$$

Since L_d is higher than L_q in REL machines, the saliency ratio is always higher than 1. Besides, i_d and i_q must have the same polarity to contribute a positive torque. It is also noticed that only the reluctance torque is available in REL machines, causing possible lower torque density than PM machines.

The REL motor is commonly current controlled, where the *d*- and *q*-axis currents are combined to get the desirable torque. In order to have a direct insight into the torque production characteristics of the REL machine, it is helpful to use the dq current plain in which i_d is plotted along the horizontal axis and i_q is plotted along the vertical axis. As an example shown in Fig. 1.6, different current circles are recognized. From the torque equation in (1.5), it is easy to calculate the optimal current phase angle (which is 45°), in absence of magnetic saturation, at which the torque–per–Ampere becomes the maximum. The maximum torque–per–Ampere (MTPA) trajectory is a straight line described by the dashed line in Fig. 1.6. When magnetic saturation is considered, the constant-torque loci differ from the symmetric hyperbolic shapes and become the curves

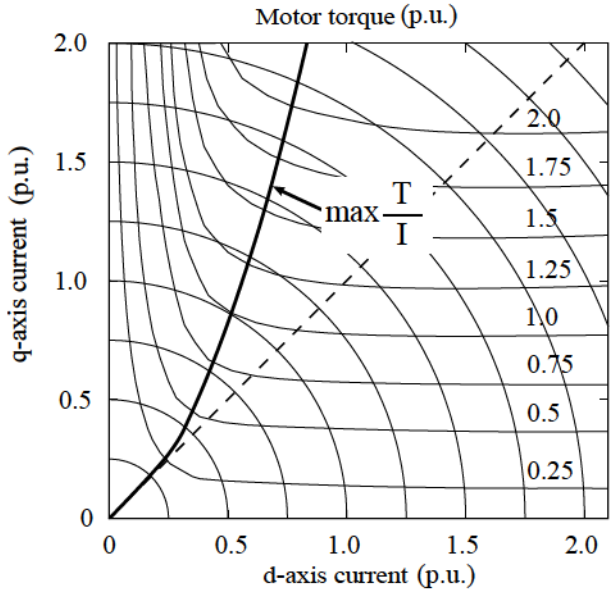

Figure 1.6: Torque map in the i_d-i_q plane, together with the MTPA trajectories without and including the effect of magnetic saturation, which are represented in dashed straight line and bold solid line, respectively.

shown in Fig. 1.6. In this case, α_i^e tends to increase and the MTPA trajectory becomes the bold solid line in the figure.

1.3.2. Power factor

The power factor (PF) is defined as

$$\cos\varphi = \frac{\omega_m T_{em}}{\frac{1}{2} m V I} \tag{1.7}$$

where ω_m is the mechanical angular speed, m is the number of phase, V and I are peak phase voltage and current, as shown in Fig. 1.5. If the stator resistance is neglected, this equation can be derived, by using (1.4) – (1.6), as [4]

$$\cos\varphi = (\xi - 1)\sqrt{\frac{\sin 2\alpha_i^e}{2(\xi^2 \cot\alpha_i^e + \tan\alpha_i^e)}} \tag{1.8}$$

Supposing $\tan\alpha_i^e = t$, then

$$\cos\varphi = (\xi - 1)\sqrt{\frac{t^2}{(t^2+1)(t^2+\xi^2)}} \tag{1.9}$$

Taking the derivative with respect to t, the maximum PF is obtained

$$\cos\varphi_{(max)} = \frac{\xi - 1}{\xi + 1} \tag{1.10}$$

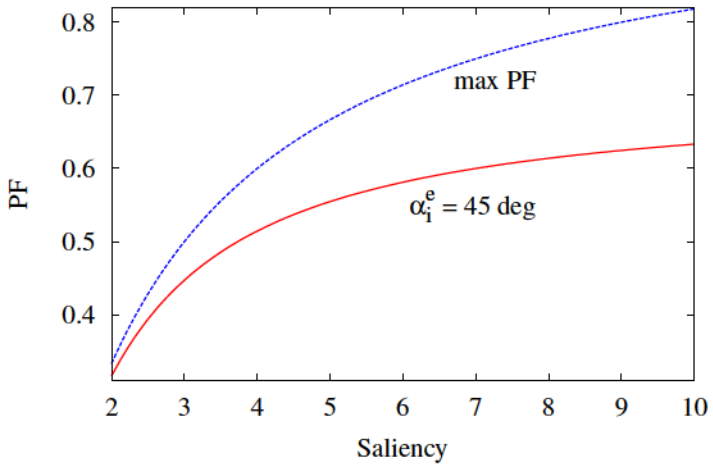

Figure 1.7: Power factor versus the saliency ratio ξ, without considering magnetic saturation.

with $t = \sqrt{\xi}$. It is noticed that the PF is a function of saliency ratio ξ. The larger the saliency ratio, the higher the maximum PF.

Alternatively, if the MTPA trajectory is followed, the PF becomes

$$\cos\varphi = (\xi - 1)\sqrt{\frac{1}{2(\xi^2 + 1)}} \tag{1.11}$$

where the iron saturation is neglected, and $\alpha_i^e = 45°$.

Fig. 1.7 shows the PF versus the saliency ratio curve neglecting magnetic saturation. The lower curve reports the PF when the current vector is operated along the MTPA trajectory, while the upper curve refers to the operating conditions along the maximum PF trajectory. The operation along the MTPA trajectory exhibits lower PF. It is also evident that the PF of the REL machine is quite low. More specifically, the maximum achievable PF is slightly higher than 0.8 referring to a saliency ratio of 10. The low PF leads to a high volt-ampere rating of the inverter.

1.4. Comparison of different rotor topologies

As aforementioned, the performance of the REL machine highly depends on the d- and q-axis inductances. The torque capability is proportional to $(L_d - L_q)$, while the PF is determined by the saliency ratio ξ. The machine performance would be quite poor in terms of torque and PF unless the rotor is properly designed. From the development history of REL machines, considerable attention has been paid to improving rotor design. In this section, the existed rotor structures are theoretically analyzed, in order to explain the trend of REL rotors.

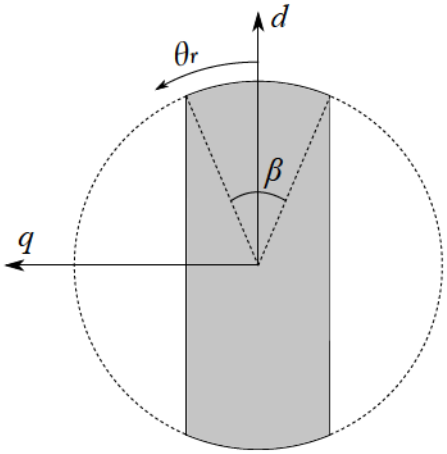

Figure 1.8: Sketch of a two-pole SP type REL rotor.

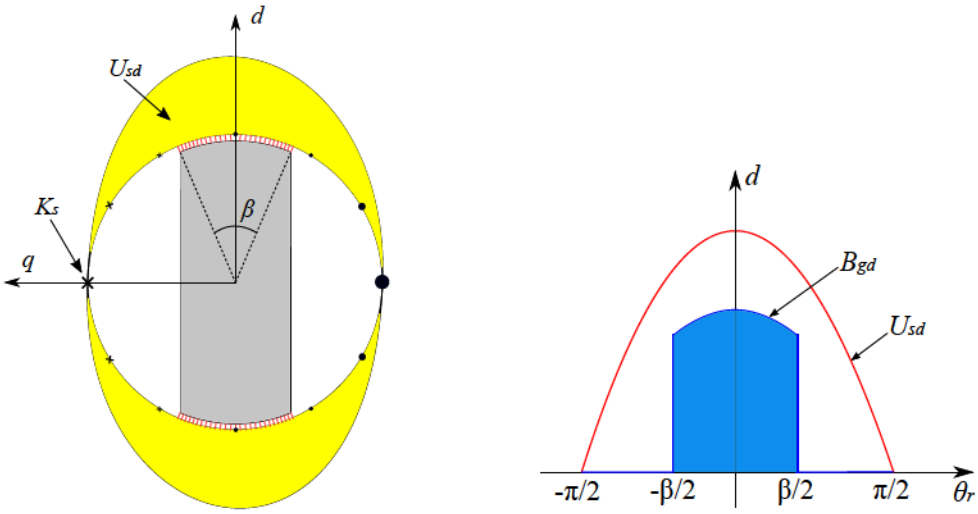

(a) Stator magnetic potential distribution.

(b) Flux density distribution.

Figure 1.9: Stator magnetic potential and flux density distributions of SP type REL machine due to d-axis currents.

1.4.1. Salient-pole rotor

The sketch of a two-pole SP type REL rotor is shown in Fig. 1.8. For simplicity, the flux is assumed to be existed only in correspondence of arc β, which is the polar arc in Fig. 1.8. The iron losses are neglected and only the fundamental harmonic of MMF is considered.

If only the magnetic field due to the stator d-axis current is considered, the corresponding stator magnetic potential distribution is plotted as Fig. 1.9(a), which can be expressed by [23]

$$U_{sd}(\theta_r) = -\frac{D}{2p}\hat{K}_s \cos(p\theta_r) \tag{1.12}$$

for a $2p$-pole machine, where $\hat{K}_s$ is the amplitude of linear current density, expressed as

$$\hat{K}_s = \frac{3k_w N_s \hat{I}}{\pi D} \tag{1.13}$$

where k_w is the winding factor of the fundamental harmonic, N_s is the number of series conductors per phase, $\hat{I}$ is phase current peak value, D is stator inner diameter, and θ_r indicates the mechanical angle in the rotor reference frame (see Fig. 1.8).

The radial flux density distribution in the airgap, produced by the d-axis current, results

$$B_{gd}(\theta_r) = \frac{\mu_0}{g}\left[U_r(\theta_r) - U_{sd}(\theta_r)\right] = \frac{\mu_0}{g}\frac{D}{2p}\hat{K}_s \cos(p\theta_r) \tag{1.14}$$

where μ_0 is the permeability constant, g is the mechanical air gap length. The rotor magnetic potential $U_r(\theta_r)$ equals to zero for the SP type. The flux density distribution is highlighted by the blue area in Fig. 1.9(b). The fundamental component of the Fourier series expansion of this distribution is

$$\hat{B}_{gd1} = \frac{4p}{\pi}\int_0^{\frac{\beta}{2}} B_{gd}(\theta_r)\cos(p\theta_r)d\theta_r = \frac{p}{\pi}\frac{\mu_0}{g}\frac{D}{2p}\hat{K}_s\left[\beta + \frac{1}{p}\sin(p\beta)\right] \tag{1.15}$$

The corresponding flux is

$$\Phi_{d1} = \frac{DL_{stk}}{p}\hat{B}_{gd1} \tag{1.16}$$

where L_{stk} is active stack length. The flux linkage is

$$\Lambda_{d1} = \frac{k_w N_s}{2}\Phi_{d1} \tag{1.17}$$

Finally, the d-axis inductance is computed by dividing the flux linkage by the stator d-axis current, which becomes

$$L_d = \frac{3p}{\pi^2}\mu_0\left(\frac{k_w N_s}{2p}\right)^2 \frac{DL_{stk}}{g}\left[\beta + \frac{1}{p}\sin(p\beta)\right] \tag{1.18}$$

When only q-axis current is considered, the corresponding stator magnetic potential distribution is plotted in Fig. 1.10(a), which can be expressed as

$$U_{sq}(\theta_r) = -\frac{D}{2p}\hat{K}_s \sin(p\theta_r) \tag{1.19}$$

The radial flux density distribution in the airgap, produced by the q-axis current, results

$$B_{gq}(\theta_r) = \frac{\mu_0}{g}\left[U_r(\theta_r) - U_{sq}(\theta_r)\right] = \frac{\mu_0}{g}\frac{D}{2p}\hat{K}_s \sin(p\theta_r) \tag{1.20}$$

The flux density distribution is again highlighted by the blue area in Fig. 1.10(b). Of course, the distribution is different from Fig. 1.9(b). The fundamental component is derived as

$$\hat{B}_{gq1} = \frac{4p}{\pi}\int_0^{\frac{\beta}{2}} B_{gq}(\theta_r)\sin(p\theta_r)d\theta_r = \frac{p}{\pi}\frac{\mu_0}{g}\frac{D}{2p}\hat{K}_s\left[\beta - \frac{1}{p}\sin(p\beta)\right] \tag{1.21}$$

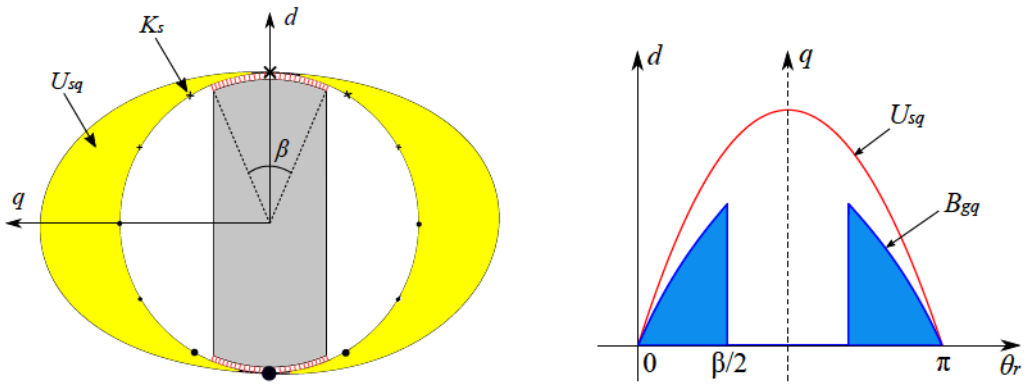

(a) Stator magnetic potential distribution. (b) Flux density distribution.

Figure 1.10: Stator magnetic potential and flux density distribution of SP type REL machine due to q-axis currents.

Similarly, the q-axis inductance results

$$L_q = \frac{3p}{\pi^2}\mu_0 \left(\frac{k_w N_s}{2p}\right)^2 \frac{DL_{stk}}{g}\left[\beta - \frac{1}{p}\sin(p\beta)\right] \tag{1.22}$$

Therefore, the difference between the d- and q-axis inductances are obtained by subtracting (1.22) from (1.18)

$$(L_d - L_q) = \frac{6}{\pi^2}\mu_0 \left(\frac{k_w N_s}{2p}\right)^2 \frac{DL_{stk}}{g}\sin(p\beta) \tag{1.23}$$

It is found that the inductance difference is proportional to $\sin(p\beta)$. Referring to (1.5), the output torque reaches the maximum when the inductance difference is maximized. As a consequence, the SP type REL machine achieves the maximum torque with $\beta = \pi/(2p)$, which implies that the salient-pole occupies 50 % of the pole pitch.

The saliency ratio can be derived by the ratio of (1.18) and (1.22)

$$\xi = \frac{L_d}{L_q} = \frac{\beta + \frac{1}{p}\sin(p\beta)}{\beta - \frac{1}{p}\sin(p\beta)} \tag{1.24}$$

where $\xi \approx 4.5$ with $\beta = \pi/(2p)$. From the point of view of saliency ratio, it would be dramatical large with very small value of β, as plotted in Fig. 1.11 for a two-pole SP type REL machine. However, this incredible saliency ratio exists only under the previous assumptions. In addition, low β will cause reduction in torque capability, as demonstrated by (1.23).

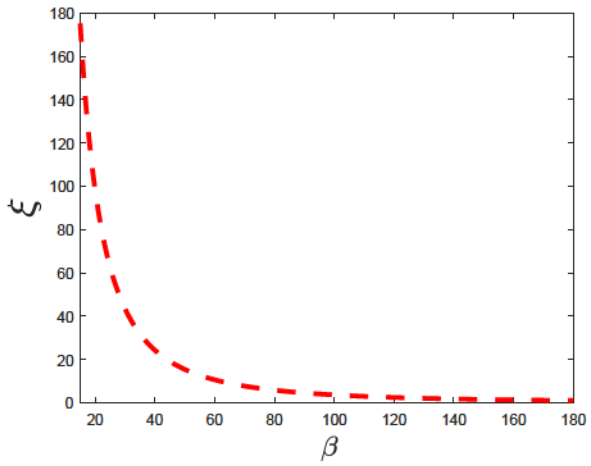

Figure 1.11: Variation of saliency ratio ξ with β for a two-pole SP type REL machine.

1.4.2. Multiple flux-barrier rotor

The REL machine with multiple flux-barrier rotor has been proposed several years ago, but only in recent years it is becoming more and more attractive. From the number of segments point of view, the ALA rotor structure can also be regarded as multiple flux-barrier rotor when the barrier number is greatly increased. In the following, the analysis is carried out on a generalized multiple flux-barrier rotor.

Similar to the previous analysis, some hypotheses are made:

1. The stator is slot-less and only the fundamental harmonic MMF is considered.
2. Iron loss and magnetic saturation is neglected.
3. Leakage inductances are disregarded.

Referring to the d-axis inductance, the same calculation procedure as the SP type machine can be carried out. The main difference is that the flux exists along almost the whole rotor surface, as shown in Fig. 1.12. The calculated L_d can be represented as

$$L_d = \frac{3}{\pi}\mu_0 \left(\frac{k_w N_s}{2p}\right)^2 \frac{DL_{stk}}{g} \tag{1.25}$$

It is the same expression as the magnetizing inductance (L_m) of the IM. Generally speaking, it is very difficult to increase this inductance within the mechanical and thermal limitations. Therefore, the design goal to obtain high machine performance is to reduce L_q, in other words, to block the q-axis flux as much as possible.

Obviously, the ideal situation is that a non-magnetic rotor is assumed. The calculated q-axis inductance is [5]:

$$L_{qmin} = \frac{3}{\pi}\mu_0 \frac{(k_w N_s)^2}{2p} L_{stk} \tag{1.26}$$

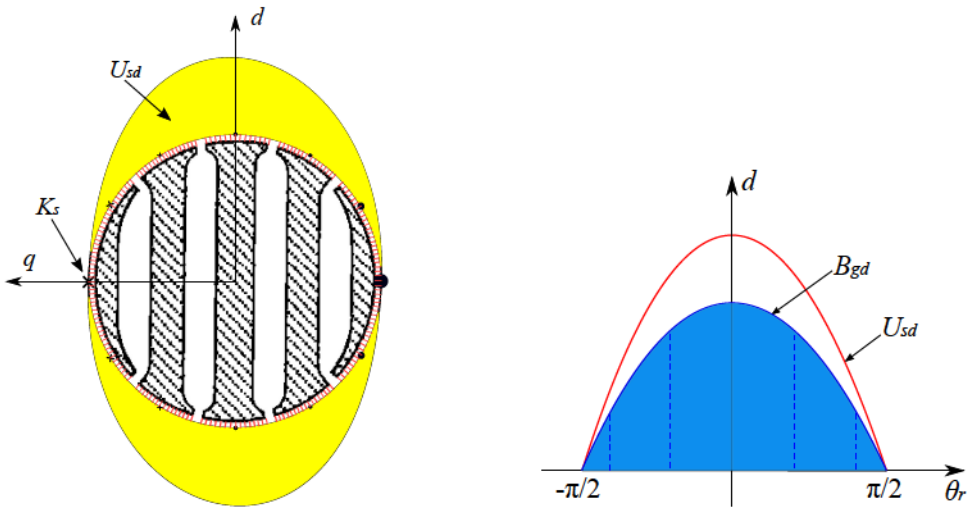

(a) Stator magnetic potential distribution. (b) Flux density distribution.

Figure 1.12: Stator magnetic potential and flux density distributions of multiple flux-barrier REL machine due to d-axis currents.

which is independent of the rotor diameter. It is also noticed that L_{qmin} is inversely proportional to pole-pair number, in contrast, L_d is inversely proportional to p^2. Then, the ideal saliency ratio is defined as:

$$\xi_{ideal} = \frac{D}{2pg} \tag{1.27}$$

which clearly shows that the ideal saliency ratio decreases with the increase of p. (1.27) gives the theoretical upper limit of the achievable saliency ratio with a given rotor geometry. It should be noted that the actual saliency ratio is always lower than ξ_{ideal}, due to iron saturation, stator leakage inductances and so on.

A more precise method to calculate L_q is proposed by Vagati [15, 23]. Theoretically, L_q is split into two components L_{qc} and L_{qf}, corresponding to "circulating" flux and "flowing through" flux (shown in Fig. 1.13(a)), respectively. The generic k-th segment is evidenced, as defined by the electrical angles θ_k and θ_{k+1}. Using (1.19), the average value U_{sk} of stator magnetic potential over the angular interval $\Delta\theta_k$ is calculated as

$$U_{sk} = -\frac{D}{2p}\hat{K}_s \frac{1}{\Delta\theta_k}\int_{\theta_k}^{\theta_{k+1}} \sin(p\theta_r)d(p\theta_r) = \frac{D}{2p}\hat{K}_s f_k \tag{1.28}$$

where

$$f_k = \frac{\cos(\theta_{k+1}) - \cos(\theta_k)}{\Delta\theta_k} \tag{1.29}$$

When a q-axis MMF is applied, the k-th segment will have a constant value of magnetic potential U_{rk}. This value is slightly lower than U_{sk}, as shown in Fig. 1.13(b). Referring to U_{sk}, it is supposed to be

$$U_{rk} = \frac{D}{2p}\hat{K}_s r_k \tag{1.30}$$

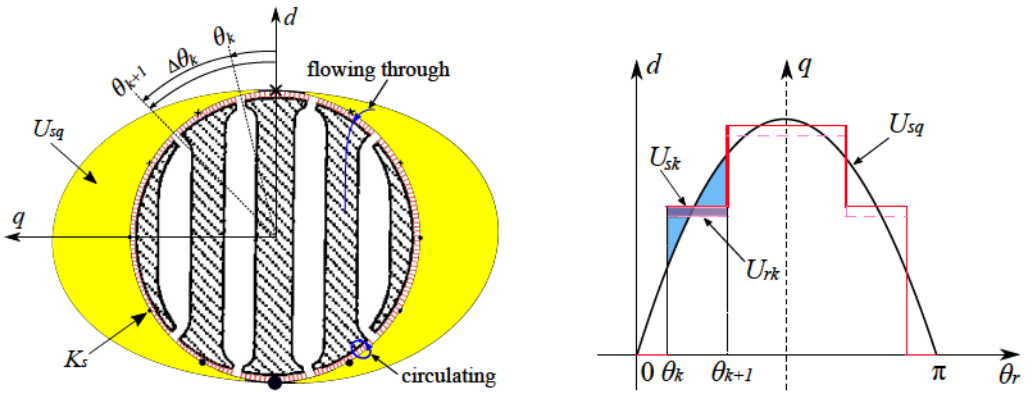

(a) Stator magnetic potential distribution.

(b) Stator and rotor magnetic potential.

Figure 1.13: Stator and rotor magnetic potential distribution of multiple flux-barrier REL machine due to q-axis currents.

where r_k is a constant value, which can be computed from the magnetic equivalent circuit [23].

The radial flux density in the airgap, produced by the "circulating" flux, results

$$B_{gqc}(\theta_r) = \frac{\mu_0}{g}\left[U_{sk} - U_{sq}(\theta_r)\right] = \frac{\mu_0}{g}\frac{D}{2p}\hat{K}_s\left[f_k + \sin(p\theta_r)\right] \tag{1.31}$$

Then

$$\hat{B}_{gqc1} = \frac{4p}{\pi}\int_0^{\frac{\pi}{2p}} B_{gqc}(\theta_r)\sin(p\theta_r)d\theta_r = \frac{4p}{\pi}\frac{\mu_0}{g}\frac{D}{2p}\hat{K}_s\left(\frac{\pi}{4p} - \frac{1}{p}\sum_k f_k^2\Delta\theta_k\right) \tag{1.32}$$

$$L_{qc} = \frac{3}{\pi}\mu_0\left(\frac{k_w N_s}{2p}\right)^2\frac{DL_{stk}}{g}\left(1 - \frac{4}{\pi}\sum_k f_k^2\Delta\theta_k\right) \tag{1.33}$$

By dividing (1.25), it is obtained that

$$\frac{L_{qc}}{L_d} = 1 - \frac{4}{\pi}\sum_k f_k^2\Delta\theta_k \tag{1.34}$$

The ratio L_{qc}/L_d does not related to pole-pair, but it rapidly decreases as the number of flux-barrier is increased. In other words, the multiple flux-barrier design, instead of one or two barriers per pole, is preferable to achieve high saliency ratio.

Regarding to the flowing through contribution, the resulted radial flux density in the airgap is

$$B_{gqf}(\theta_r) = \frac{\mu_0}{g}\left(U_{rk} - U_{sk}\right) = \frac{\mu_0}{g}\frac{D}{2p}\hat{K}_s\left(r_k - f_k\right) \tag{1.35}$$

Then L_{qf} is derived as

$$L_{qf} = \frac{3}{\pi}\mu_0\left(\frac{k_w N_s}{2p}\right)^2\frac{DL_{stk}}{g}\frac{4}{\pi}\sum_k\left[f_k\left(f_k - r_k\right)\Delta\theta_k\right] \tag{1.36}$$

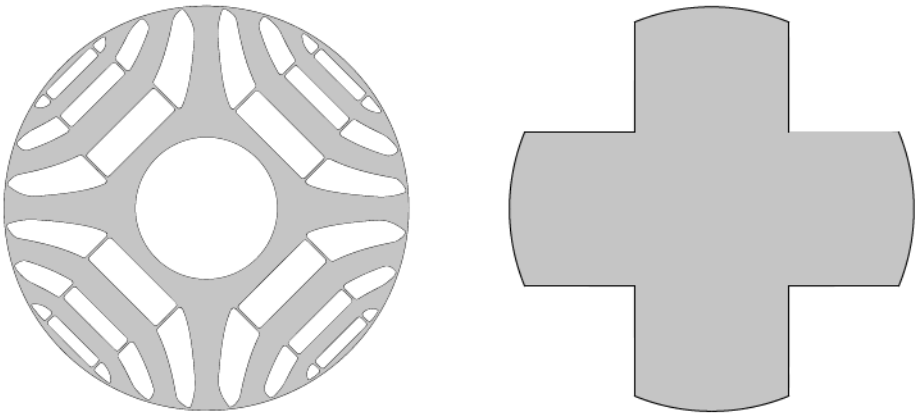

(a) Multiple flux-barrier rotor in [24]. (b) SP type rotor structure.

Figure 1.14: Comparison of different rotor structures.

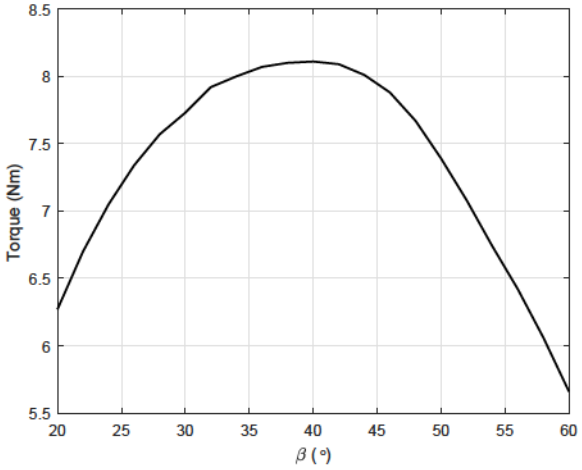

Figure 1.15: Torque variation with β for an SP type REL machine.

Finally, the ratio of L_{qf} to L_d is

$$\frac{L_{qf}}{L_d} = \frac{4}{\pi}\sum_k \left[f_k\left(f_k - r_k\right)\Delta\theta_k\right] = \frac{8}{\pi}\frac{pg}{D}\sum_k f_k\varphi_k \tag{1.37}$$

where φ_k is the per-unit flux, which is proportional to $(f_k - r_k)$ [23]. This ratio depends on the flux-barrier shape and, more importantly, the pole-pair p. Since L_{qc}/L_d does not depend on p, it is easy to find that the lower the p number, the higher the saliency ratio will be. But in the practice design, the choice of pole-pair number is a trade-off among stator yoke design, the saliency ratio and the mechanical reliability.

In order to compare the two rotor topologies, the multiple flux-barrier rotor in [24] is replaced by an SP type rotor, as shown in Fig. 1.14. The SP type machine is simulated by FEA, considering different rotor shapes with variable polar arc β. Fig. 1.15 shows the average torque variation with β. The average torque reaches the maximum where β is around 40°. Actually, if saturation is neglected, β is 45° to achieve the maximum torque for a four-pole machine. By using the same current amplitude (the current angle

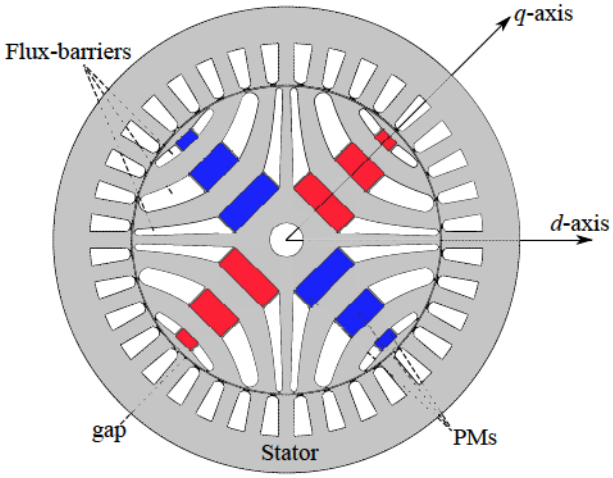

Figure 1.16: Cross-section of PMAREL motor.

is different), the achievable maximum torque of the SP type REL machine is about 8.1 Nm, while the reported torque in [24] is 11.3 Nm. This confirms the low torque density of the SP type REL machine. Besides, it is noticed in the simulation that the torque ripple of the SP one is dramatical higher than that of the multiple flux-barrier one.

1.5. PM-assisted synchronous reluctance machines

As mentioned before, the PF of the REL machine is fairly low. Usually, this drawback can be compensated by insetting PMs into rotor flux-barriers. This configuration is called PM-assisted synchronous reluctance (PMAREL) machine, as shown in Fig. 1.16. The high anisotropic rotor allows cost-effective ferrite magnets instead of rare-earth PMs to be used, so as to reduce the machine cost. Unlike the regular interior PM (IPM) machine, the torque of the PMAREL machine is mainly dominated by the reluctance torque component due to the high rotor saliency.

The PMs are introduced to increase the PF of the REL machine. According to the reference frame, the PMs produce a flux linkage along the negative q-axis to compensate the flux linkage $L_q I_q$, as depicted in Fig. 1.17. Since the voltage vector is rotated towards the current vector, the PF increases. Therefore, the flux linkages of the PMAREL machine are computed as:

$$\begin{cases} \lambda_d = L_d i_d \\ \lambda_q = L_q i_q - \Lambda_m \end{cases} \tag{1.38}$$

where Λ_m is the flux linkage due to PMs. The average torque is calculated as:

$$T_{em} = \frac{3}{2} p \left[\Lambda_m i_d + (L_d - L_q) \, i_d i_q \right] \tag{1.39}$$

Despite of the same reluctance torque as (1.5), a PM torque component is added in the PMAREL motor. The machine torque density is improved only if the two torque components have the same sign, which is obtained when the q-axis current component

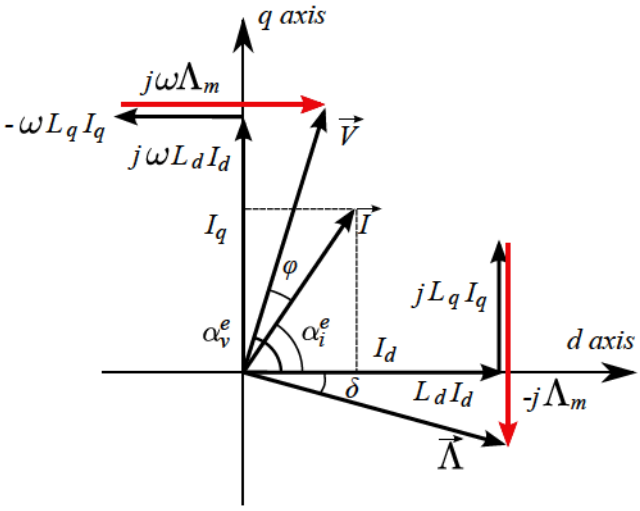

Figure 1.17: Phasor diagram representative of the PMAREL machine.

is positive. The d- and q-axis currents can be freely controlled to obtain the desirable torque. Actually, the performance of the PMAREL machine strongly depends on the current vector control strategy.

1.5.1. MTPA control

Within the current limit (I_{max}), the current vector is controlled to achieve MTPA. In theory, the MTPA trajectory is obtained from the derivative of torque equation (1.39) with respect to the current phase angle. Making the derivative equals to 0, the optimal current vector angle of MTPA trajectory satisfies the following relationship:

$$\alpha_i^e = \sin^{-1}\left(\frac{\sqrt{\Lambda_m^2 + 8(L_d - L_q)^2 I^2} - \Lambda_m}{4(L_d - L_q)I}\right) \tag{1.40}$$

When Λ_m equals to 0, the PMAREL machine becomes a pure REL machine, and α_i^e keeps constant (45°). Same result is obtained in Section 1.3.1.

In case of iron saturation, FEA simulations are required. Similarly, the optimal current vector angle is chosen when the torque achieves the maximum under given current amplitude. As an example, the MTPA trajectory is shown from point O to point B in Fig. 1.18.

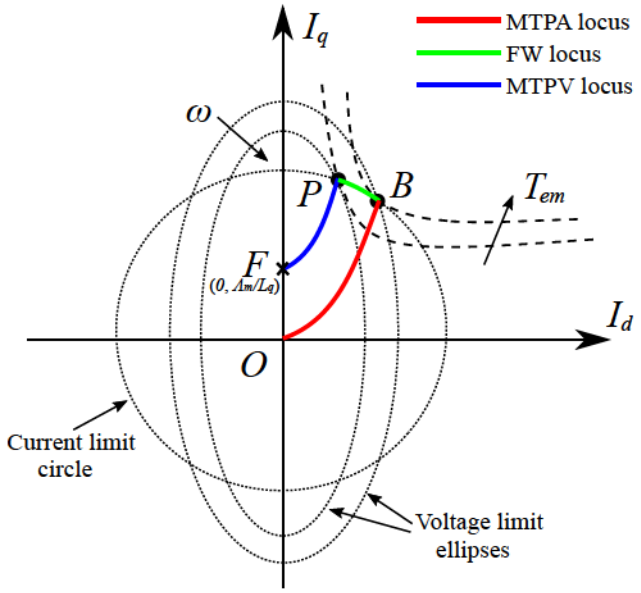

Figure 1.18: Circle diagram of a PMAREL motor drive.

1.5.2. FW control

From (1.38), the flux linkage of the PMAREL machine under steady-state condition is given by

$$\Lambda = \sqrt{(L_d I_d)^2 + (L_q I_q - \Lambda_m)^2} \tag{1.41}$$

When the stator resistance is ignored, the phase voltage is calculated as

$$V = \omega\Lambda = \omega\sqrt{(L_d I_d)^2 + (L_q I_q - \Lambda_m)^2} \tag{1.42}$$

It is described by ellipses in the i_d-i_q plane, as shown in Fig. 1.18. When the stator flux is kept constant, the locus described by the current vector in the i_d-i_q plane is an ellipse with center $(0, \Lambda_m/L_q)$. When the speed increases (but is less than the rated value), the voltage increases proportionally to guarantee the same stator flux, till the voltage limit (V_{max}) is reached. So the constant-flux locus is also the limit-voltage locus. When the operating speed exceeds its rated value, the stator flux has to be reduced to keep constant the voltage at its limit value, and consequently the weakened-flux locus and the voltage-limit locus shrink. The d-axis current, which is the main flux in the machine, is decreased by increasing the current phase angle α_i^e. This technique is called the "flux weakening (FW)". The current amplitude remains the same, so that the current vector moves along the current limit circle, as shown from point B to point P in Fig. 1.18. The d- and q-axis currents are derived as the following equations, under the limits of both voltage and current (V_{max} and I_{max}):

$$\begin{cases} I_q = \dfrac{\Lambda_m L_q - \sqrt{(\Lambda_m L_q)^2 - \left(L_q^2 - L_d^2\right)\left(\Lambda_m^2 - \frac{V_{max}^2}{\omega^2} + I_{max}^2 L_d^2\right)}}{L_q^2 - L_d^2} \\ I_d = \sqrt{I_{max}^2 - I_q^2} \end{cases} \tag{1.43}$$

1.5.3. MTPV control

Referring to the phasor diagram of the PMAREL machine in Fig. 1.17, the flux linkage can be represented as

$$\begin{cases} \Lambda_d = \Lambda \cos\delta = L_d I_d \\ \Lambda_q = \Lambda \sin\delta = L_q I_q - \Lambda_m \end{cases} \tag{1.44}$$

Substituting to the torque equation, (1.39) becomes

$$T_{em} = \frac{3}{2} p \frac{\Lambda_m \Lambda \cos\delta}{L_d} + \frac{3}{2} p(\xi - 1) \frac{\Lambda \cos\delta \left(\Lambda \sin\delta + \Lambda_m\right)}{L_d} \tag{1.45}$$

The maximum torque–per–flux linkage control, which is the equivalent to the maximum torque–per–Voltage (MTPV) control, can be achieved by setting $\frac{dT_{em}}{d\delta} = 0$, obtaining

$$\frac{2(\xi - 1)}{\xi} \Lambda \sin^2\delta + \Lambda_m \sin\delta - \frac{\xi - 1}{\xi} \Lambda = 0 \tag{1.46}$$

it is solved as

$$\sin\delta = \frac{-\Lambda_m + \sqrt{\Lambda_m^2 + 2a^2}}{2a} \tag{1.47}$$

where $a = 2(\xi - 1)\Lambda/\xi$. After that, the d- and q-axis currents can be obtained from (1.44).

The MTPV trajectory shows the tangent points of torque loci and voltage ellipses. Following the FW trajectory, when the current limit circle, the voltage limit ellipse and the MTPV trajectory intersect, as shown by point P in Fig. 1.18, the operation of the machine moves to MTPV control. In this region, the current vector angle α_i^e increases, while the current amplitude decreases with the increasing speed. Finally, the machine can be operated at infinite speed theoretically.

Actually, the MTPV operation happens only if $\Lambda_m < L_q I_{max}$ [21]. When the PM flux linkage is quite high, *i.e.*, $\Lambda_m > L_q I_{max}$, the center of the ellipses is outside the current limit, and no crossing point exists between MTPV trajectory and the current limit circle.

1.6. Conclusion

This Chapter mainly reviews the development history, basic equations and performance characteristics of REL machines. It is noticed that the REL machine performance is highly depended on saliency ratio. Looking back the development history of REL machines, the improvement of saliency ratio is of vital importance. Comparing with the SP and ALA rotor types, the TLA rotor type with multiple flux-barriers achieves relatively high saliency ratio, low rotor loss and low torque ripple. Therefore, it is chosen to be designed and analyzed in the next Chapters.

The inset PMs in the rotor flux-barrier help to improve the power factor and torque density of the REL machine. The methodologies of current vector control, in terms of MTPA control, FW control and MTPV control, are also introduced for the following use.

Chapter 2

Design Methodology of REL Machines

The REL machines have been more and more attractive in recent years. Since the stator can be made of conventional laminations of IMs or PM machines, the most challengeable part of REL machine design lies on the rotor structure. This Chapter provides a detailed parametric analysis of the rotor geometry for both REL and PMAREL machines, in order to suggest an automatic design. The shape of flux-barriers is selected to achieve both high d-axis inductance and low q-axis inductance, so as to obtain high output torque and high power factor. Methods to properly design the geometry of barrier ends and PMs are adopted. Some tuning steps are suggested in order to achieve the high performance design. After that, such a procedure is used to rapidly analyze the impact of some parameters on the machine performance so as to give a design guideline. At last, the demagnetization limit of a PMAREL machine under overload operation is analyzed.

2.1. Suitable shape of flux-barriers

FROM the torque expression of the REL machine in (1.5), it is observed that the output torque is proportional to the difference between the d-axis inductance (L_d) and the q-axis inductance (L_q). Therefore, it is extremely important to design the rotor geometry so as to increase such a difference. In the following part, the design objective is to maximize the d-axis inductance, and simultaneously, minimize the q-axis inductance.

In the TLA type REL machine with multiple flux-barriers, the d-axis flux passes through the whole iron paths while the q-axis flux is blocked by flux-barriers. To achieve the design goal, the d-axis flux should flow the iron parts smoothly, while the q-axis flux should be blocked as much as possible. This requires the flux-barrier shape to be parallel to the d-axis flux lines, and perpendicular to the q-axis flux lines. When cross-coupling effect is ignored, the d-axis flux lines are completely perpendicular to the q-axis flux lines. As a result, the aim is to design the flux-barrier lines approximately along d-axis flux lines.

Without considering iron saturation, the behavior of the d-axis flux in a two-pole rotor can be regarded as an inviscid, incompressible fluid flow around a circular cylinder. This is described analytically by a simple mathematical equation, which is called stream

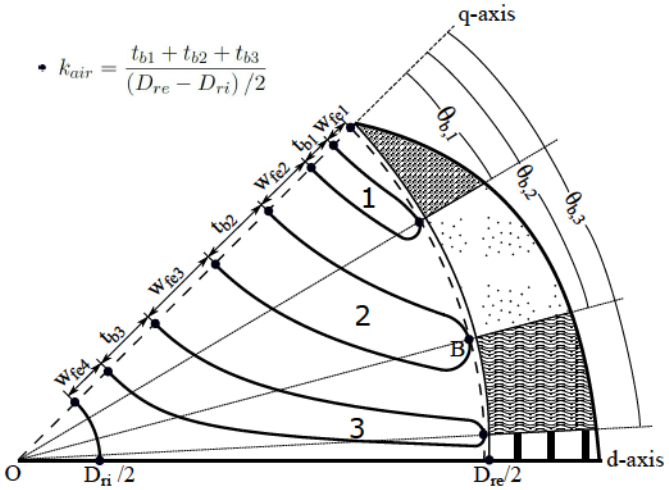

Figure 2.1: Parameter definitions on the rotor and d-axis flux density distribution.

function [25]:

$$\psi(\rho,\xi) = \left(\rho - \frac{\rho_0^2}{\rho}\right)\sin\xi \tag{2.1}$$

where ρ_0 is the radius of the cylinder, ρ and ξ are radial coordinate and angular coordinate in the polar coordinate system, respectively. The streamlines, who represent the d-axis flux lines, are obtained by the contour of different values of ψ. For a given streamline, the stream function $\psi(\rho,\xi)$ is constant. By using conformal mapping technique, the following stream function is derived to describe the d-axis flux distribution in a $2p$-pole rotor [26]:

$$\Psi(r,\theta) = \frac{\sin(p\theta)\left[\left(\frac{2r}{D_{ri}}\right)^{2p} - 1\right]}{\left(\frac{2r}{D_{ri}}\right)^{p}} \tag{2.2}$$

where r is the radius, θ is the mechanical angle from the d-axis, D_{ri} is the rotor inner diameter. Ψ is called potential factor in the following text. Since different streamlines have different values of Ψ, only these streamlines with their potential factors known are visualized. Therefore, the flux-barrier boundaries can be obtained.

According to (2.2), the potential factor is computed once the radial and angular coordinates (r, θ) of one point on the streamline is determined. Obviously, the angular coordinates of the points on the q-axis, as highlighted in Fig. 2.1, are easily obtained. Therefore, they are chosen as the "main points" to calculate the potential factors. The remaining problem is to determine the radial coordinates of these points, which are related to the width of flux-barriers and iron paths. To this purpose, the insulation ratio k_{air} is firstly defined (as shown in Fig. 2.1):

$$k_{air} = \frac{\sum_{i=1}^{N_b} t_{bi}}{(D_{re}-D_{ri})/2} = \frac{\sum_{i=1}^{N_b} t_{bi}}{\sum_{i=1}^{N_b} t_{bi} + \sum_{i=1}^{N_b+1} w_{fei}} \tag{2.3}$$

where t_{bi} is the width of the i-th flux-barrier, w_{fei} is the width of the i-th iron path, N_b is the number of barriers, D_{re} is the rotor outer diameter. Detailed definition of the parameters are shown in Fig. 2.1. The insulation ratio assumes an important role to limit the saturation of the iron paths, as will be described in Section 2.6. Once k_{air} is defined, the total widths of the flux-barriers and iron paths are determined, respectively.

The next step is to calculate the width of each iron path and flux-barrier individually. The width of each iron path is computed according to the flux density distribution of the d-axis flux. This allows to select the iron path widths to be proportional to the amount of d-axis flux flowing through them. Assuming a sinusoidal waveform of the flux density in the airgap, as shown in Fig. 2.1, the flux passing through each iron channel is represented as:

$$\begin{cases} B_1 = \int_0^{\theta_{b,1}} \hat{B}_d \sin(p\theta) d\theta \\ B_2 = \int_{\theta_{b,1}}^{\theta_{b,2}} \hat{B}_d \sin(p\theta) d\theta \\ \dots \\ B_i = \int_{\theta_{b,i-1}}^{\theta_{b,i}} \hat{B}_d \sin(p\theta) d\theta \\ \dots \\ B_{N_b+1} = \int_{\theta_{b,N_b}}^{\frac{\pi}{2}} \hat{B}_d \sin(p\theta) d\theta \end{cases} \tag{2.4}$$

where $\hat{B}_d$ is the amplitude of the flux density, and $\theta_{b,i}$ is the barrier end angle of the i-th flux-barrier. The average flux density in the i-th iron channel $B_{avg,i}$ is given by:

$$B_{avg,i} = \frac{1}{\theta_{b,i} - \theta_{b,i-1}} \int_{\theta_{b,i-1}}^{\theta_{b,i}} \hat{B}_d \sin(p\theta) d\theta \tag{2.5}$$

with $1 \leqslant i \leqslant N_b$, and

$$B_{avg,N_b+1} = \frac{2}{\pi - 2\theta_{b,N_b}} \int_{\theta_{b,N_b}}^{\frac{\pi}{2}} \hat{B}_d \sin(p\theta) d\theta \tag{2.6}$$

The width of each iron path is proportional to its corresponding average flux density, and therefore

$$w_{fei} = \frac{(D_{re} - D_{ri})(1 - k_{air}) B_{avg,i}}{2 \sum_{i=1}^{N_b} B_{avg,i} + B_{avg,N_b+1}} \tag{2.7}$$

The width of each flux-barrier should be designed to minimize the q-axis flux as much as possible, by means of the total insulation. The stator magnetic potential distribution due to q-axis currents is shown in Fig. 2.2(a). Similar to the flux density, the average value of stator magnetic potential in front of each flux-barrier is:

$$U_{avg,i} = \frac{1}{\theta_{b,i} - \theta_{b,i-1}} \int_{\theta_{b,i-1}}^{\theta_{b,i}} \hat{U}_q \cos(p\theta) d\theta \tag{2.8}$$

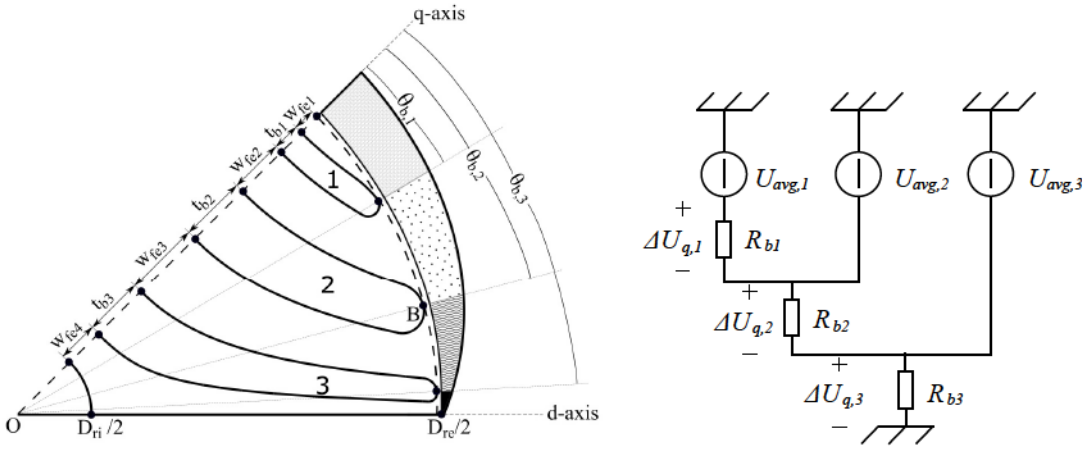

(a) Stator magnetic potential distribution. (b) Magnetic circuit.

Figure 2.2: Stator magnetic potential distribution due to q-axis currents and the corresponding magnetic circuit.

with $1 \leqslant i \leqslant N_b$, and $\hat{U}_q$ is the amplitude of magnetic potential. From (2.8) the difference of average stator magnetic potential between consecutive flux-barriers can be expressed as

$$\Delta U_{q,i} = U_{avg,i} - U_{avg,i+1} \tag{2.9}$$

with $1 \leqslant i \leqslant N_b - 1$, and

$$\Delta U_{q,N_b} = U_{avg,N_b} \tag{2.10}$$

Referring to Fig. 2.2(b), $\Delta U_{q,i}$ represents the magnetic voltage drop across the i-th flux-barrier once the air-gap magnetic voltage drop is disregarded. From the derivations given in [15], the following relationship is found for the flux-barrier width that achieves the lowest L_q:

$$\frac{t_{bk}}{t_{bh}} = \frac{\Delta U_{q,k}}{\Delta U_{q,h}} \sqrt{\frac{l_{b,k}}{l_{b,h}}} \approx \frac{\Delta U_{q,k}}{\Delta U_{q,h}} \sqrt{\frac{\theta_{b,k}}{\theta_{b,h}}}, \quad k \neq h \tag{2.11}$$

where $l_{b,k}$ is the length of the k-th flux-barrier, with the approximation of $l_{b,k} = \theta_{b,k} D_{re}$. Therefore, the width of each flux-barrier is

$$\begin{cases} t_{b1} = t_{b1} \\ t_{b2} = t_{b1} \dfrac{\Delta U_{q,2}}{\Delta U_{q,1}} \sqrt{\dfrac{\theta_{b,2}}{\theta_{b,1}}} \\ \dots \\ t_{bi} = t_{b1} \dfrac{\Delta U_{q,i}}{\Delta U_{q,1}} \sqrt{\dfrac{\theta_{b,i}}{\theta_{b,1}}} \\ \dots \\ t_{bN_b} = t_{b1} \dfrac{\Delta U_{q,N_b}}{\Delta U_{q,1}} \sqrt{\dfrac{\theta_{b,N_b}}{\theta_{b,1}}} \end{cases} \tag{2.12}$$

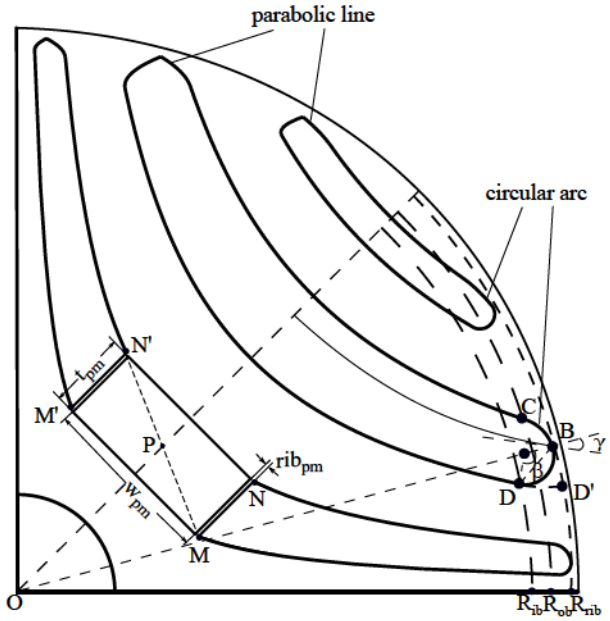

Figure 2.3: Shape comparison of different barrier ends (parabolic shape on the upper left and circular shape on the bottom right [27]) and definition of PM geometry.

The superposition of these equations results to the total flux-barrier length. Thus the value of t_{b1} can be obtained, which is

$$t_{b1} = \frac{(D_{re} - D_{ri})\, k_{air}}{2 \sum_{i=1}^{N_b} \frac{\Delta U_{q,i}}{\Delta U_{q,1}} \sqrt{\frac{\theta_{b,i}}{\theta_{b,1}}}} \tag{2.13}$$

After that, the width of the i-the flux-barrier is calculated from (2.12) by substituting (2.13).

After obtaining w_{fei} from (2.7) and t_{bi} from (2.12), the radial coordinates of the "main points" on the q-axis are obtained geometrically. Then the potential factors are calculated from (2.2). In order to draw the whole flux-barrier line, the coordinates of other points on the streamline need to be determined. The radial coordinate of any point on a certain streamline is expressed as

$$r\,(\theta, \Psi) = \left(\frac{D_{ri}}{2}\right) \sqrt[p]{\frac{\Psi + \sqrt{\Psi^2 + 4\sin^2\,(p\theta)}}{2\sin\,(p\theta)}} \tag{2.14}$$

It is noticed that the angular coordinate is essential to determine the radial coordinate. Starting from the "main points" on the q-axis, the angular coordinate reduces with the increasing radius. To obtain the minimum angle, the limit point of each streamline (that is, when the streamline ends and the barrier end starts, i.e., point D in Fig. 2.3) needs to be determined. This point is posed to be the intersection between the streamline and the limit circle, whose radius is R_{ib} for inner barrier boundary or R_{ob} for outer barrier boundary.

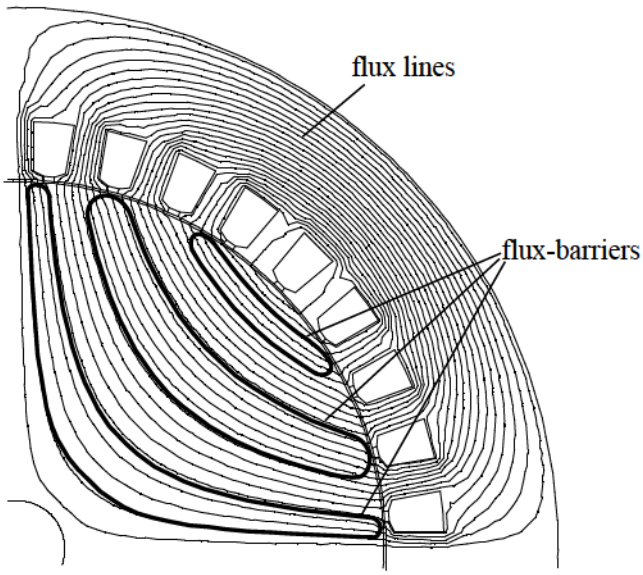

Figure 2.4: Comparison of d-axis flux lines and streamlined flux-barriers.

R_{ib} is calculated according to the following steps. Firstly, the point on the streamline with the radius of R_{rib} is determined (whose radius equals to rotor radius minus rib thickness, as shown by D' in Fig. 2.3). Then, the streamline which flows through the barrier end point B is obtained, together with the slope of the streamline at point B. The angle γ between this slope and the line OB is computed geometrically. Therefore, R_{ib} is experientially given by:

$$R_{ib} = R_{rib} - BD' \cos\gamma \tag{2.15}$$

By using R_{ib}, the angular coordinate of point D on the streamline is obtained. Then the coordinates of other points on the streamline are determined from (2.14). Finally, the flux-barrier lines can be drawn. Fig. 2.4 shows the flux lines (in thin curves) of a machine excited by d-axis current only, without any flux-barriers in the rotor. In comparison, the streamline flux-barrier shape is highlighted by the bold curves. It is verified that the flux-barrier shape approaches the d-axis flux lines, as expected.

2.2. Selection of the barrier ends

The iron ribs have a strong influence on the performance of REL machines. At the same time, the shape of barrier ends has to be carefully designed, to avoid stress concentration on the ribs.

Parabolic line can be used to draw the flux-barrier ends (shown in the upper left half of Fig. 2.3), and its equation is easily assumed as:

$$y = ax^2 + bx + c \tag{2.16}$$

Substituting the coordinate of points B and D in Fig. 2.3, and the slope of point D, coefficients a, b and c are calculated. Then the parabolic line can be drawn. However,

Table 2.1: Performance Comparison of the Machines with Three Different Barrier Ends

	T_{avg} (Nm)	Torque ripple
Parabolic line	327	27.6%
Circle arc	330	23.2%
Mixed	330	21.7%

this kind of barrier ends contain some sharp points (shown in the upper left half of Fig. 2.3), which are harmful especially for machines operated at high speed.

The ideal shape of barrier ends would be circular arc, from mechanical point of view (shown in the bottom right half of Fig. 2.3) [27]. With the coordinate of point B and D, the angle between line BD and OB can be calculated, together with the central angle β (shown in Fig. 2.3). In this way, the circular arc between point B and D can be drawn easily. However, some factors may limit to use the circular arc, such as the distance of BD' and the central angle β, and it is not always possible to draw such a barrier-end. In this case, parabolic lines are still used when the circular arcs are not well suited.

In order to compare the electromagnetic performance of different barrier ends, three rotors are designed with hyperbola, circle and mixed approach, respectively. Table 2.1 shows the performance of three machines. It is observed that all the considered solutions produce almost the same output torque. Considering the sharp points in parabolic lines, it is better to use circular or mixed barrier ends.

2.3. Drawing of the PMs

In PMAREL machine, the shape of PMs is commonly rectangular for simple manufacture. When PMs are introduced, the starting points to draw the streamlines are no longer on the q-axis. Referring to Fig. 2.3, the starting points become M and N, which are determined by PM width w_{pm}, rib thickness rib_{pm} and the stream function. The center point P of the flux-barrier is determined by using point M, point N and its symmetrical point N'. Supposing the PM is placed with the same center point as the flux-barrier, it is easy to draw the shape of PM by using w_{pm} and PM thickness t_{pm}. Besides, when the width of PM equals zero, the PMAREL rotor is automatically reduced to a pure REL rotor.

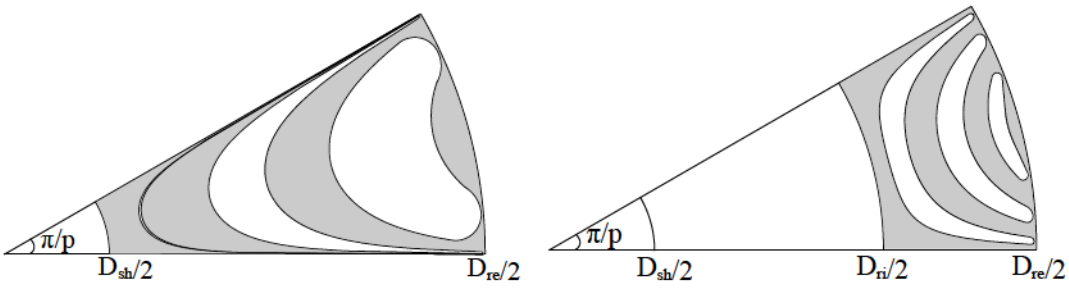

(a) Inner rotor diameter without control. (b) Inner rotor diameter with limit (2.17).

Figure 2.5: Comparison of machine models without and with inner rotor diameter control.

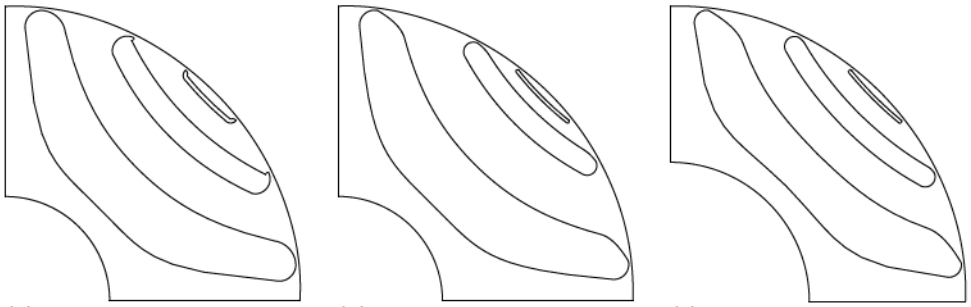

(a) Rotor model without modification. (b) Rotor model with changing w_{fe} only. (c) Rotor model with changing w_{fe} and D_{ri}.

Figure 2.6: Comparison of rotor shapes without and with modifications.

2.4. Modification procedures (suggested tricks)

As said above, the selection of the geometry of the flux-barrier and its ends are key points in the REL machine design. In order to draw a rotor with proper shape, some geometric tricks can be carried out.

At the beginning, the inner rotor diameter (for drawing) is adjusted, especially in case of high number of poles. Fig. 2.5 shows the comparison between machine models without and with inner rotor diameter limit. To get a proper rotor design, a limit value of the inner rotor diameter should be provided. Equation (2.17) gives the condition used for the inner rotor diameter, fixing the total rotor length to be lower than 1.2 times of the half pole pitch:

$$D_{ri} > D_{re} - 1.2\frac{\pi D_{re}}{2p} \tag{2.17}$$

The total rotor length is $(D_{re} - D_{ri})/2$ and the half pole pitch is $(\pi D_{re})/(4p)$ in Fig. 2.5(a). Using (2.17), it is possible to avoid too small inner rotor diameter, with a consequent improper drawing.

The second tricky action deals with the flux-barrier end point B. Generally speaking, the position of point B should be located between the upper and lower streamlines of its corresponding flux-barrier, as shown in Fig. 2.3. In some situations, point B could be outside of these two lines, causing sharp points in the rotor laminations. Thus, actions

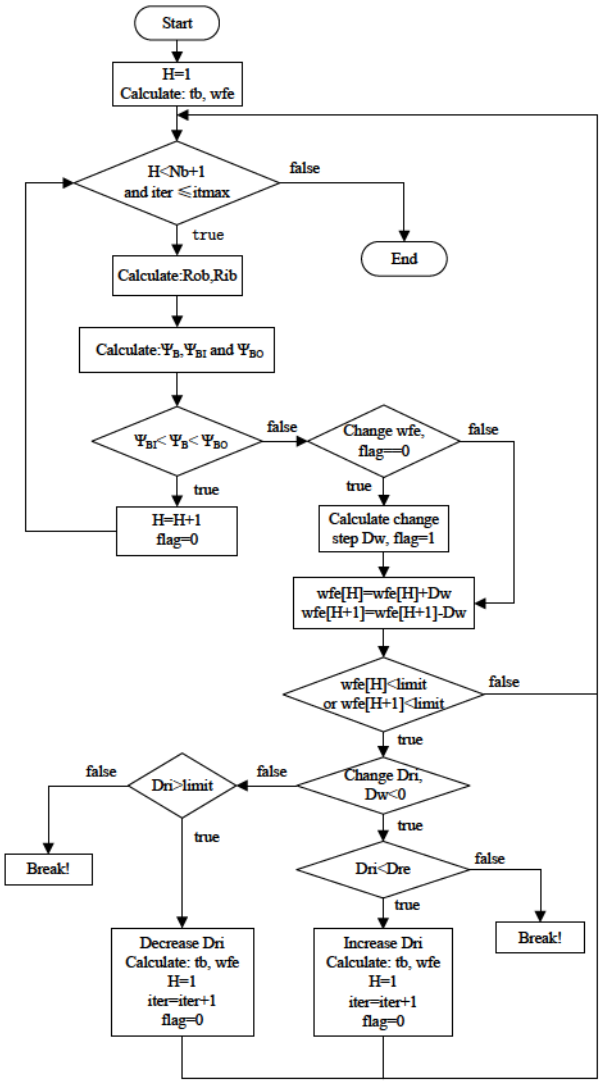

Figure 2.7: Modification procedure for changing w_{fe} and D_{ri}.

should be taken to check the position of point B. It is calculated that the outer the streamline, the larger the potential factor. Therefore, it is a good way to check the position of the point B by comparing the potential factors with the upper and lower barrier lines.

If point B is outside of these two barrier lines (as shown in Fig. 2.6(a), the first and the second flux-barrier end points are outside of their corresponding barrier lines), firstly, the width of each iron path (w_{fe}) between flux-barriers is modified in order to obtain a proper barrier shape. The step of change D_w is calculated by the distance of BD', as shown in Fig. 2.3. If w_{fe} at H-th iron path is increased by D_w, then w_{fe} at (H+1)-th iron path needs to be reduced by D_w (as described in Fig. 2.7). The obtained rotor model is plotted in Fig. 2.6(b).

Unfortunately, this change does not always work properly, because the width of each iron path cannot be too small so as to avoid saturation of the iron path. If w_{fe} reaches

Table 2.2: Main Dimensions of the Designed Motor

Design parameters	Value	Unit
Stator outer diameter	270	mm
Stator inner diameter	148.5	mm
Tooth width	8.3	mm
Back iron thickness	28.9	mm
Airgap thickness	0.5	mm
Active stack length	308	mm

its limit value, then the rotor inner diameter D_{ri} is changed (as shown in Fig. 2.6(c)). The sign symbol of D_w determines whether to increase or decrease D_{ri}. After changing D_{ri}, the widths of each iron and barrier part need to be recalculated iteratively. After a fixed number of steps, if point B is still outside the flux-barrier lines, the angle of the flux-barrier is forced to be within the flux-barrier lines. Detailed procedure of this modification is illustrated in Fig. 2.7.

According to the rotor geometry analysis above, codes have been written to draw the REL machine model automatically. After that, FEA simulations are carried out to calculate the machine performance. Referring to the stator lamination of a standard induction machine, a REL machine is designed with $Q_s = 36$ slots and $2p = 4$ poles. The main dimensions are given in Table 2.2. The total length of the stator laminations is 314 mm, and the stacking factor is 0.98. The stator slot fill factor is fixed to be 0.4. Thanks to the automatic model drawing procedure, some analyses are carried out on the key parameters of the rotor structure. The results are reported hereafter as a design guideline.

2.5. Number of flux-barriers

Since the number of flux-barriers has a significant effect on the output torque of the REL machine, the number of flux-barriers is investigated first. During this optimization process, the insulation ratio is kept constant. For simplicity, the barrier end angles for different barrier numbers are calculated in the following steps. As analyzed in [18], to reduce the torque ripple in the REL machine, the number of separation points per pole pair (n_r) is deduced by:

$$n_r = n_s \pm 4 \tag{2.18}$$

where $n_s = Q_s/p$ is the number of stator slots per pole pair. The separation points are equal-space distributed along the rotor periphery. In this case, with 36 slots and 4 poles, $n_s = 18$, and thus, n_r is calculated to be 14 or 22. According to these separation points, barrier end angles can be easily obtained. For $n_r = 14$, the barrier end angles are 25.71°, 51.43° and 77.14°, while for $n_r = 22$, the barrier end angles are 16.36°, 32.73°, 49.09°, 65.45° and 81.82°. Fig. 2.8 represents reference symbols for the barriers with different barrier end angles. With A, B, C for the barriers in the configuration on

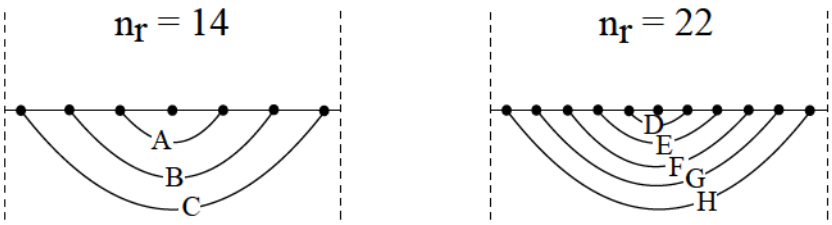

Figure 2.8: Reference symbols for the barriers with different barrier end angles.

Table 2.3: Comparison of REL Motors with Three Barriers per Pole for Possible Barrier Angle Combinations

Selection of barriers	T_{avg} (Nm)	Torque ripple
D, F, H	321	21%
D, G, H	312	62%
E, F, G	320	73%
E, F, H	329	21%
E, G, H	325	41%
F, G, H	324	14%
A, B, C	330	22%

the left ($n_r = 14$) and D, E, F, G, H for the barriers in the configuration on the right ($n_r = 22$).

For a given number of flux-barriers, it is possible to select different barrier end angles. For example, referring to three barriers per pole, there are 10 combinations. It is difficult to draw some of them according to the limits imposed to the geometry. Table 2.3 shows the comparison of REL machine with three barriers per pole for feasible barrier end angle combinations. For the same number of barriers, the torque ripple significantly changes according to the barrier end angles, while the average torque remains almost the same. The last two combinations in Table 2.3 seem to be proper choices when three barriers per pole are used, according to rotor model shown in Fig. 2.9. It is worth noticing that, even if the angles are selected by means of (2.18), the results are completely different if some flux-barriers are removed.

Considering manufacturing and mechanical limits, only a number of flux-barriers up to four is considered. Proper choices of barrier end angles for one, two and four barriers is represented in Table 2.4. Comparing Table 2.3 and Table 2.4, it can be seen that with the increase of the number of barriers, the average torque yields an increase, but this increment becomes lower and lower with the number of flux-barriers. Therefore, a solution with three or four barrier layers per pole is recommended in practical design, which is also verified in [28, 29].

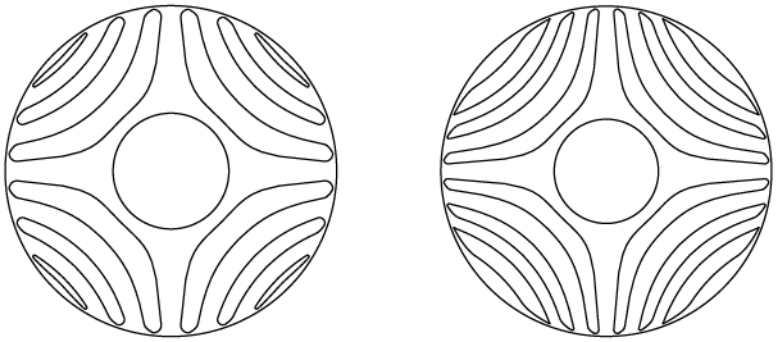

Figure 2.9: Rotor models of proper barrier end angles with three barriers per pole (ABC on the left and FGH on the right).

Table 2.4: Proper Choices of Barrier End Angles for One, Two and Four Flux-Barriers per Pole

N_b	Selection of barriers	T_{avg} (Nm)	Torque ripple
1	B	265	16%
1	G	273	28%
2	B, C	318	14%
2	F, H	314	24%
4	D, F, G, H	333	12%
4	E, F, G, H	336	40%

2.6. Insulation ratio

The aim of this section is to analyze the impact of k_{air}, which is defined in (2.3). Generally speaking, it plays an important role to limit the saturation of the rotor iron paths [30]. Fig. 2.10 shows the rotor geometry corresponding to two different values of k_{air} (**0.35** and **0.6**, respectively). It is seen that the higher k_{air}, the thinner the iron paths are, and also the higher saturation in the rotor is.

Under the rated operating condition, Fig. 2.11 shows the behaviors of L_d, L_q, torque, power factor, efficiency and stator core losses of the REL machine as a function of k_{air}. With the increase of k_{air} the main variation is the decrease of L_d, while only a slight decrease of L_q is observed. Since the value of L_q is relatively small, the torque mainly varies according to L_d. Hence, there is not an actual benefit in increasing the flux-barrier width. When k_{air} increases, the rotor iron paths become thinner, so that the flux density in the stator is reduced, and thus, the iron losses are reduced as well. On the contrary, both efficiency and power factor do not present considerable variations with k_{air}. Similar results are also obtained and confirmed in [30].

On the other hand, k_{air} is also suggested to be chosen according to the stator slot width to slot pitch ratio, so as to get the machine equally saturated in both stator and rotor.

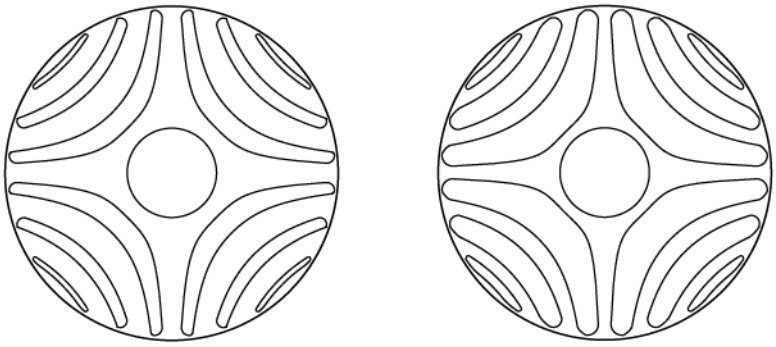

Figure 2.10: Rotors with different k_{air}: 0.35 (left) and 0.6 (right).

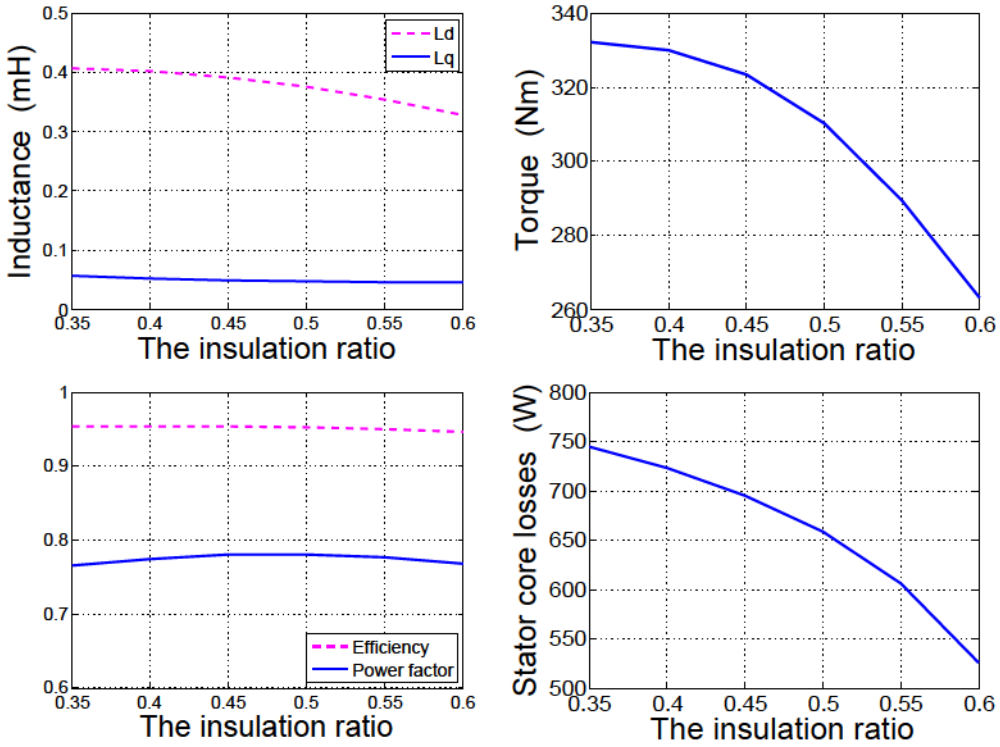

Figure 2.11: Behaviors of L_d, L_q, torque, power factor, efficiency and stator core losses of REL machines versus different k_{air}.

2.7. PM width

As mentioned in the Section 1.5, PMs can be introduced to improve the performance of the REL machine. The PM used here is ferrite magnet, which has a low residual magnetic flux density but with significant low price (the residual magnetic flux density is 0.314T). The PM thickness in each barrier is considered to be the same as the corresponding flux-barrier width. Table 2.5 shows the comparison of PMAREL machines with different PM widths. The width of PMs is represented as the percentage of the corresponding barrier length. As expected, PMs not only contribute to the average torque, but also increase the power factor. In general, the higher the PM width, the higher the torque and power factor. It is verified in [24] that after inserting PMs into the

Table 2.5: Comparison of PMAREL Motors with Different Widths of PMs

PMs Width	Λ_m (mVs)	T_{cog} (mNm)	T_{avg} (Nm)	Torque ripple	γ (deg)	PF
25%	6.9	24.5	340	19.3%	67	0.792
50%	18.1	174.2	351	20.4%	65	0.835
75%	29.6	450.0	363	20.2%	63	0.874
100%	42.2	694.4	386	20.4%	61	0.914

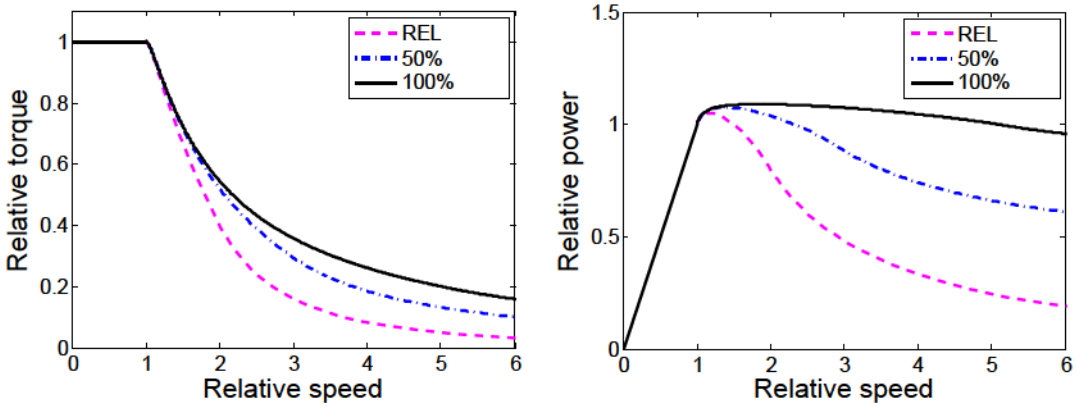

Figure 2.12: Comparison of PMAREL machines with different widths of PMs for flux weakening operation.

REL machine, the average torque increases around 7%, and the power factor increases from 0.83 to 0.88 when the output torque is 10 Nm. Besides, the current angle (γ) corresponding to the MTPA operating point slightly reduces with the increase of PMs, which is also verified by the experimental results in [24].

The effect of the PM width on flux weakening capability is shown in Fig. 2.12. The current phasor angle is varied when the machine speed is higher than the rated speed, so that the terminal voltage could be kept at the limit value. Torque, power and speed are represented in p.u.. Dealing with high speed, the output power of the REL machine drops quickly while the PMAREL machine with all barriers filled by PMs shows no significant drop even operated at 6 times of the rated speed. More specifically, the wider the PM width, the better the flux weakening capability. PMAREL machines with other PM widths are also investigated, and the same trend is obtained. This conclusion was verified in [24] by experimental results. The REL and PMAREL machines are with the same geometry, but the PMAREL one shows wider constant power speed range (about 2 times of the REL one), exhibiting better flux-weakening capability.

In the following, the PM width equal to 25% of the corresponding barrier length is selected as an example. To investigate the effect of the inset PMs on the flux lines, the flux lines of the REL and PMAREL machines under different operating conditions are reported in Fig. 2.13. Fig. 2.13(a) and Fig. 2.13(b) show the flux lines due to d-axis current only, while Fig. 2.13(c) and Fig. 2.13(d) show the flux lines with rated current in the maximum torque angle. Due to the low residual flux density of ferrite magnets,

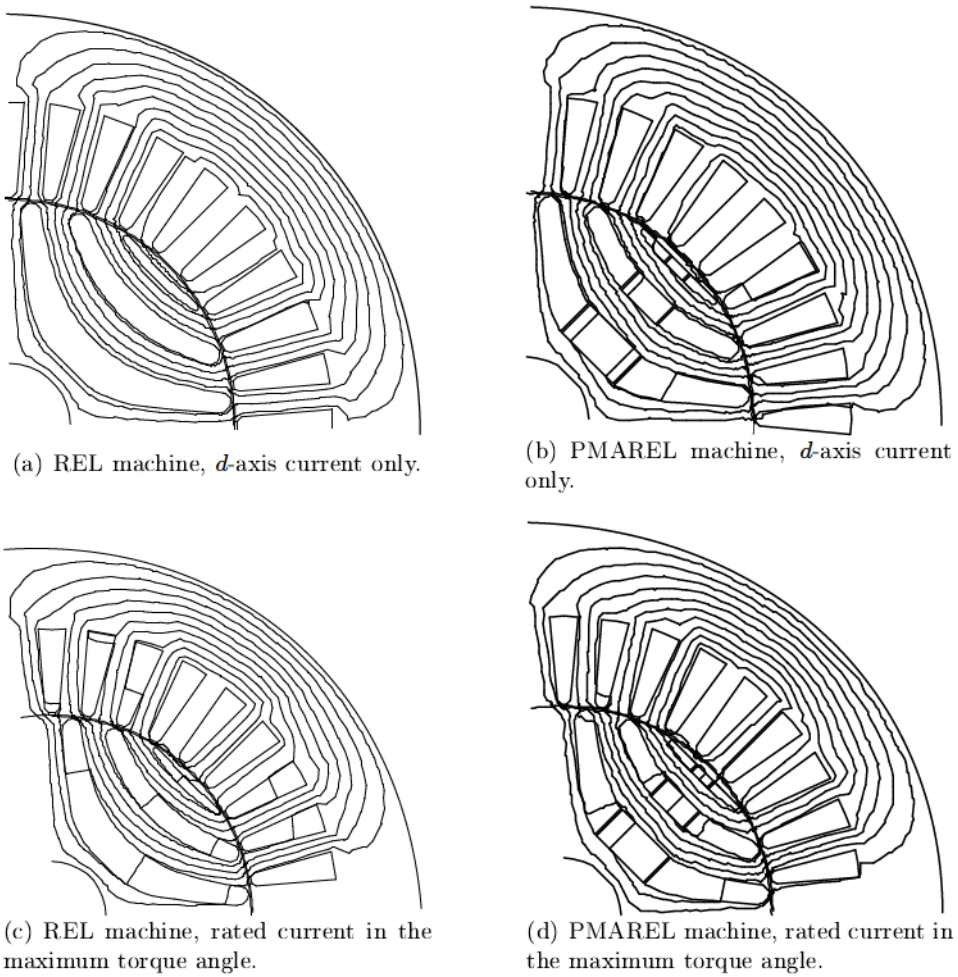

(a) REL machine, *d*-axis current only.

(b) PMAREL machine, *d*-axis current only.

(c) REL machine, rated current in the maximum torque angle.

(d) PMAREL machine, rated current in the maximum torque angle.

Figure 2.13: Flux lines in the REL and PMAREL machines under different operating conditions.

the effect of the PMs is low.

2.8. PM demagnetization

For the PMAREL machine, the flux density of PM operating point has to be computed to check the possibility of PM demagnetization. This computation is based on the worst operation condition, which means that all the stator current produces a flux totally against the PM flux (namely demagnetizing current). Firstly, the no-load flux density of the PMAREL motor is simulated, as shown in Fig. 2.14(a). After that, the flux density of the REL motor (with PMs removed) is computed with the demagnetizing current, as shown in Fig. 2.14(b). Then the PM operating points are obtained by adding these two situations together.

In the specific case under study, it is verified that at the rated current, the minimum flux density of PMs in the three flux-barriers are 0.071T, 0.172T and 0.133T, respectively. This means that all the operating points of the PMs are above the knee point

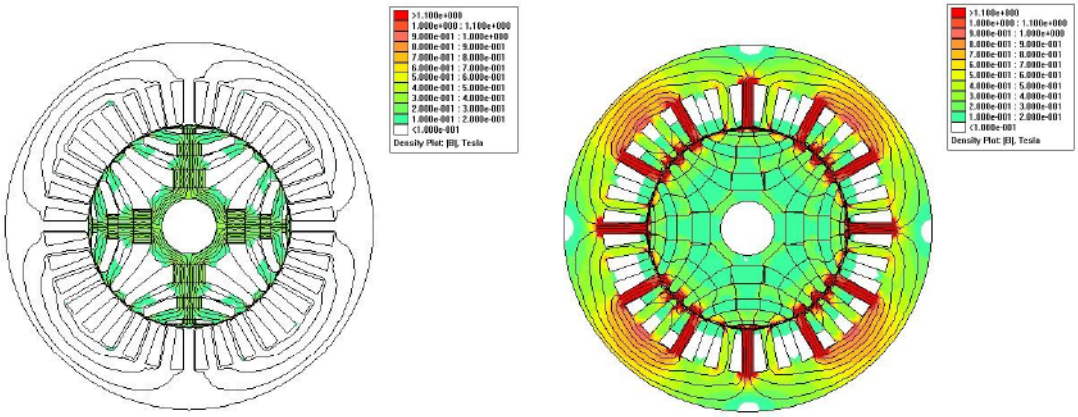

(a) Flux density map of PMAREL motor at no-load operating condition.

(b) Flux density map of REL motor fed by q-axis current only (i.e., a demagnetizing current).

Figure 2.14: Flux density map at different operating conditions.

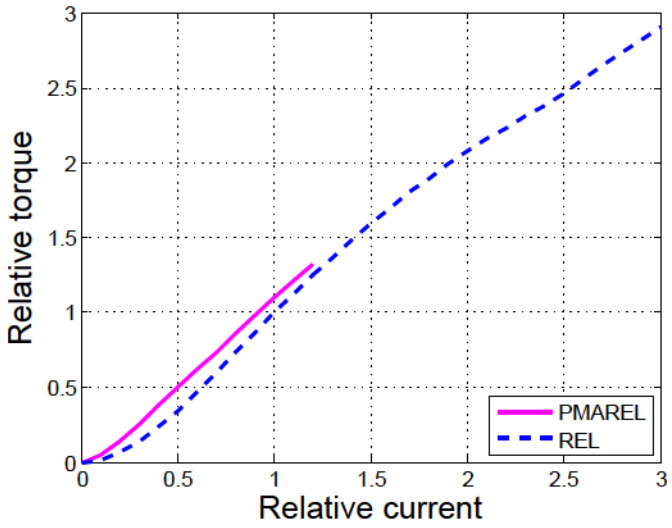

Figure 2.15: Overload capability comparison of the PMAREL and REL motors.

(0.020 T at 100 °C), and no irreversible PM demagnetization occurs. It is notable that the PMs in the most external barrier are the most stressed, as confirmed in [31, 32], special attention should be paid on them.

It is also verified that the maximum demagnetizing current is only 1.2 times over the rated current (by following the upper steps to calculate the minimum flux density in PMs), which obviously limits the overload capability of the PMAREL motor. Fig. 2.15 shows the comparison of the overload capability of the REL and PMAREL motors. Torque and current are compared with the rated values of the REL motor. Due to the absence of PMs, the REL machine is expected to achieve very high overload capability. When the PMAREL machine is used for high overload conditions, it is suggested to properly increase the PM thickness in order to reduce the risk of irreversible PM demagnetization.

2.9. Conclusion

This Chapter firstly deals with the analysis of the rotor geometry of both REL and PMAREL machines. An automatic procedure to properly draw the rotor structure is described, according to past research on this kind of machine. Smooth barrier ends are introduced and useful equations are given for use. Some tricks are also suggested in order to overcome some geometric issues. All steps are described in detail so as to allow an easy implementation by the interested readers.

After that, as an applicative example, such a drawing procedure is used to rapidly analyze the impact of some rotor parameters on the machine performance. The results obtained with the proposed rapid procedure form a practical design guideline for this kind of motors. Among the others, it is pointed out that some results agree with those found in literature, but others have to be carefully considered. Useful suggestions are given all over the Chapter.

Chapter 3

REL Motors for EV Applications

This Chapter proposes a design procedure to develop a high-torque-density, low-torque-ripple and high-efficiency REL motor. The objective is to design a REL motor according to the dimension of commercial Lexus LS 600h motor, so as to achieve a detailed performance comparison between the two motor topologies. The preliminary design of the REL motor is carried out keeping the same stator, while the rotor is replaced by an optimized reluctance one. By combing the automatic design procedure with differential evolution (DE) algorithm, reluctance rotors with three and four flux-barriers per pole are optimized. After that, the stator is redesigned, and the optimization procedure is carried out in terms of split ratio, slot-pole combination and rotor optimization. An analytical calculation of slot area is innovatively derived. Finite element analysis simulations are then combined to obtain the optimal split ratio. Some design parameters are kept constant in order to make a fair comparison. The performance comparison between the optimized REL motor and an IPM motor (similar to LS 600h motor) is then carried out. Finally, performance improvements with PMs inset into the optimized REL rotor are investigated, exhibiting some attractive features with the PMAREL motor.

3.1. Introduction

WITH the growing of energy crisis, air pollution and global warming, the electrical traction system is gaining more and more interest in both academic and industrial fields. It is remarkable that the popularity of electric vehicles (EVs) and hybrid electric vehicles (HEVs) is expanding significantly in the last decade. The electric motor, being one of the key devices, determines the main performance of the electrical mobility. Compared to conventional industrial machines, traction electrical motors require the merits of cost saving, high efficiency, high torque density, high overload capability, wide constant power speed range, high reliability, low noise and vibration, etc.

Among various machine topologies, the IPM motor has been recognized as the most promising candidate [33–35]. It accounts for over 80% of EV and HEV market at present, and even a higher percentage is expected in the near future. On the other hand, some challenges are related to IPM motors, *i.e.*, high production cost, vulnerability to short-circuit fault, high back electromagnetic force (EMF) at high speed and high risk

Table 3.1: Power Density Comparison of Several Hybrid/Electric Vehicle Motors [41]

	Peak power (kW)	Power density (kW/L)	Specific power (kW/kg)
2004 Prius	50	3.3	1.1
2006 Honda Accord	12	1.5	0.5
2007 Camry	70	5.9	1.7
2008 Lexus LS 600h	110	6.6	2.5
2010 Prius	60	4.8	1.6
2011 Sonata	30	3.0	1.1
2012 Sonata HSG	8.5	2.7	0.7
2012 Leaf	80	4.2	1.4
2020 DOE targets	55	5.7	1.6

of irreversible PM demagnetization. Most importantly, a worldwide concern about the price volatility and availability of rare-earth magnets is growing. Therefore, many researchers are focused on investigating alternative non-rare-earth traction drives.

IM firstly comes up the researches' mind, mainly due to its low cost, robust structure and well–established manufacturing techniques [36, 37]. Besides, the wide flux-weakening range makes it very suitable for EV application. Nevertheless, the low power density and inferior efficiency are potential challenges of IMs. The switched reluctance machine (SRM) is also a candidate in terms of simple and robust rotor structure, possible operation with high temperatures or high rotational speeds [38, 39]. The major disadvantage of SRM is acoustic noise and vibration, which becomes very significant at high speeds and heavy loads [40].

On the other hand, the REL motor attracts more and more attention in recent years, even though it has not been widely used in traction drive field. Without magnets and rotor bars, the rotor construction is more robust than either PM or IM machines. With the development of over 30 years, it achieves the merits of low cost, high efficiency, low maintenance, and high reliability. In addition, it is also characterized by no back EMF, leading to a inherent fault tolerance capability. All these features reveal the REL motor to be an attractive candidate for electrical mobilities.

As a consequence, this Chapter aims to investigate the performance characteristics of the REL motor for EV applications. The REL motor is designed according to one commercial IPM motor (Lexus LS 600h motor). Some design parameters and inverter limitations are kept constant, in order to make a fair performance comparison. Detailed procedures are given in the following.

3.2. The Lexus LS 600h motor

The 2008 Lexus LS 600h is the third hybrid car in the Toyota luxury vehicle division – Lexus. Its motor performance was deeply evaluated and tested in [42]. Comparing

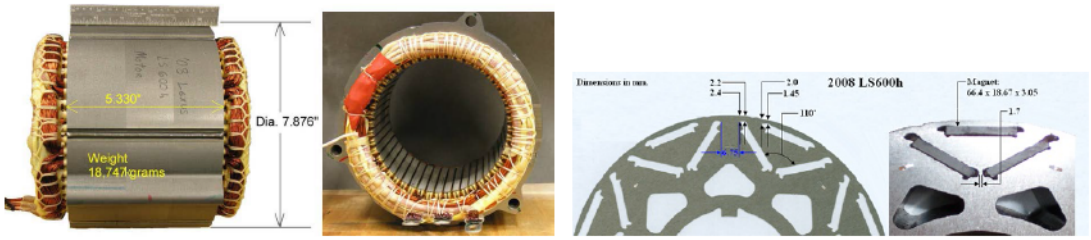

(a) Picture of the stator. (b) Rotor laminations.

Figure 3.1: Lexus LS 600h motor [42].

Table 3.2: Main Dimensions of the Lexus LS 600h Motor

Design parameters	Symbol	Value	Unit
Number of stator slots	Q_s	48	–
Number of pole pairs	p	4	–
Stator outer diameter	D_e	200	mm
Stator inner diameter	D	130.86	mm
Shaft diameter	D_{sh}	53	mm
Active stack length	L_{stk}	135.4	mm
Airgap thickness	g	0.89	mm
Tooth width	w_t	6	mm
Back iron height	h_{bi}	13.32	mm
Slot opening	w_{so}	1.88	mm
Rib thickness	t_{tib}	1.45	mm
Magnet Width	w_{pm}	18.67	mm
Magnet thickness	h_{pm}	3.05	mm

to the other commercial traction motors (as shown in Table 3.1), the Lexus LS 600h motor exhibits quite high power density and specific power. Therefore, it is selected as the reference for the REL motor design.

The stator assembly of the Lexus LS 600h motor is shown in Fig. 3.1(a), while the rotor lamination is shown in Fig. 3.1(b). One of the most notable features of this motor is the rotor geometry, with an additional magnet to the previous "V" configuration of the Prius. This triangular-shape of magnets create a more uniform flux distribution in the airgap.

As measured in [42], the main dimension of the Lexus LS 600h motor is listed in Table 3.2. These dimensions are the starting points of the REL motor design in the following. It is noticed that the Lexus LS 600h motor achieves 110 kW within the stator temperature limit of 150 °C for a transient time of 18 s (with current of 330 A_{peak} and speed of 4500 rpm) [42]. As a consequence, the current limit is set to be 330 A_{peak}, and the corresponding current density is 25 A/mm^2. The calculated stator slot fill factor k_{fill} is 0.4247. The DC bus voltage of the inverter is 650 V. The experimental efficiency

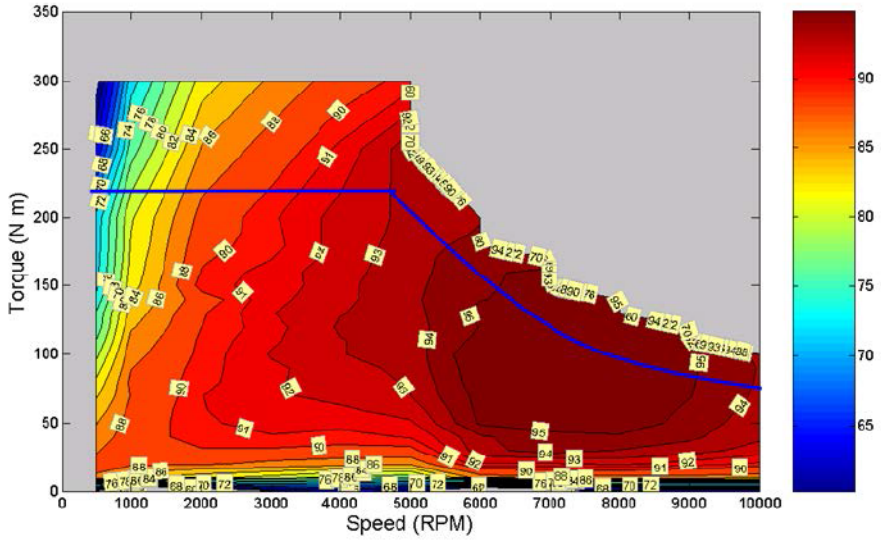

Figure 3.2: The experimental LS 600h motor efficiency map [42].

map is shown in Fig. 3.2 [42]. It is observed that the maximum achievable efficiency is 95 % and a large portion of the operation region achieves the efficiency above 90 %. Since the motor exhibited about 110 kW within the stator temperature limit of 150 °C in 18 s, the blue curve is recognized as the peak torque behavior.

3.3. REL rotor optimization with DE algorithm

In order to make a fair comparison with the IPM motor, the REL motor is constrained to satisfy some dimension limits of the Lexus LS 600h motor. For the design of REL machines, the most challenging and creative aspect lies on the rotor design, by increasing dramatically the rotor anisotropy to improve the torque density and selecting proper barrier end angles for torque ripple suppression. Key efforts to achieve these objectives include parametric machine modeling and optimization strategy. In Chapter 2, an automatic drawing and simulation procedure has been developed. Hereafter, it is combined with differential evolution (DE) algorithm to achieve the optimal REL rotor design.

3.3.1. DE algorithm

As is well-known, DE algorithm is a population-based stochastic searching method, suitable for combinatorial optimization problems [43–45]. It is firstly proposed in the mid-1990s, and has been applied for machine optimization problems in recent years [46–48].

The algorithm includes the processes of initialization, mutation, crossover and selection. At the beginning, the initial parameter vectors of the individuals are randomly generated, which should cover the entire parameter space; After evaluating the fitness of each member, parameter vectors of a new generation are created through the operators of mutation and crossover; Then, an explicit one-to-one survivor selection is carried out; Once the new population is generated, the process of mutation, crossover and selection

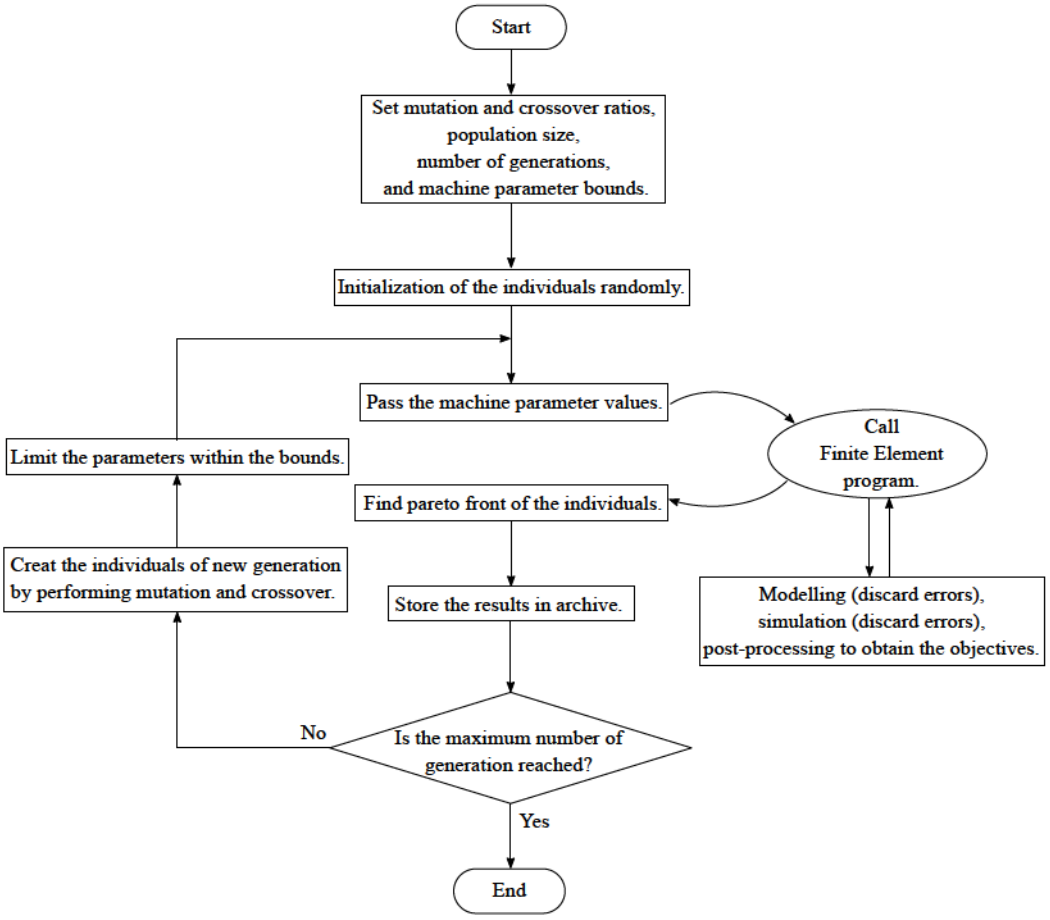

Figure 3.3: Optimization procedure using FEA and DE algorithm.

is repeated till the convergence of the algorithm or a specified number of generations is reached. Detailed explanation of this algorithm is referred to [43, 44].

The process of mutation expands the search space by using a scale factor F (*i.e.* mutation ratio) to recombine random vector differential with the base individual. High value of F helps to avoid the local optimum, while it sacrifices the speed of convergence. Therefore, the value of F is seldom greater than 1.0.

The process of crossover, which is performed with a probability of CR (*i.e.* crossover ratio), mixes successful solutions from the previous generation with current donors. In the extreme circumstance, $CR = 1$ means a fully consideration of the current donors, which certainly increases the population diversity but makes the difference between the donor vector and the previous vector large.

The rule of thumb values of the mutation and crossover ratios is recommended as $F \in [0.5, 1.0]$ and $CR \in [0.5, 1.0]$ [44]. In this problem, they are set to be $F = 0.9$ and $CR = 0.7$, respectively.

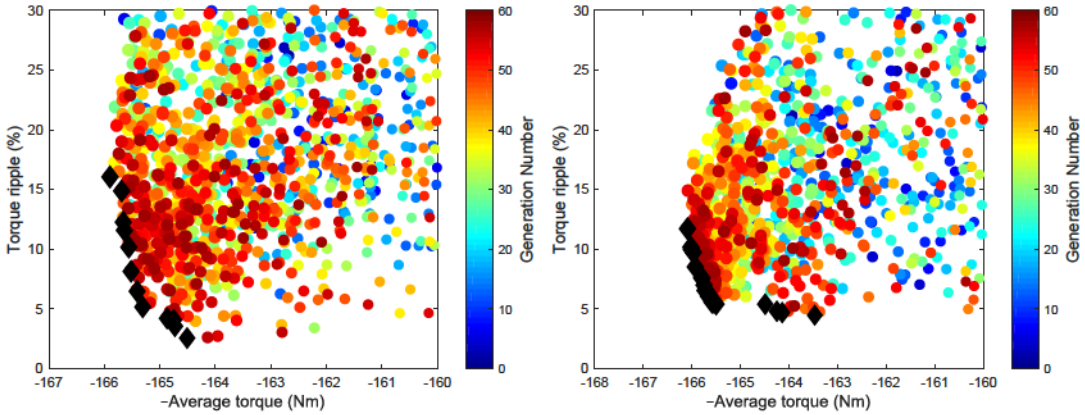

(a) Three barriers per pole in the rotor.

(b) Four barriers per pole in the rotor.

Figure 3.4: Optimization results with different numbers of rotor flux-barriers.

3.3.2. Rotor optimization with three and four flux-barriers per pole

The preliminary design of the REL motor is carried out by fixing the same stator as the Lexus motor. DE algorithm is utilized for the rotor optimization, which makes it easy to obtain a low-torque-ripple high-torque design. Detailed optimization procedure is illustrated in Fig. 3.3.

For the optimization of the REL rotor, key design parameters are flux-barrier numbers, barrier end angles and insulation ratio k_{air}, as indicated in Chapter 2. The design objectives are focused on average torque and torque ripple. The torque ripple is defined as the ratio of peak-to-peak value to the average torque.

Based on the results in Section 2.5, three and four flux-barriers per pole are investigated, respectively. As far as three-barrier rotor is considered, the optimization result is plotted in Fig. 3.4(a). Meanwhile, the corresponding result of four-barrier rotor is shown in Fig. 3.4(b). The black diamond points form the Pareto front. Once the Pareto front is obtained, the designer can select the preferred compromise solution among the ones on the front, with a clear view of how each objective is penalized by the improvement of the other ones.

The results show that the torque ripple of REL machine can be significantly reduced by using optimization algorithm. The maximum torque of the four-barrier machine is very close to the three-barrier machine, which is around **166** Nm (about **70%** of the Lexus LS 600h motor). In the following parts, only three-barrier rotor is considered. In order to fully inspire the potential of the REL machine, the stator is redesigned in the next Section.

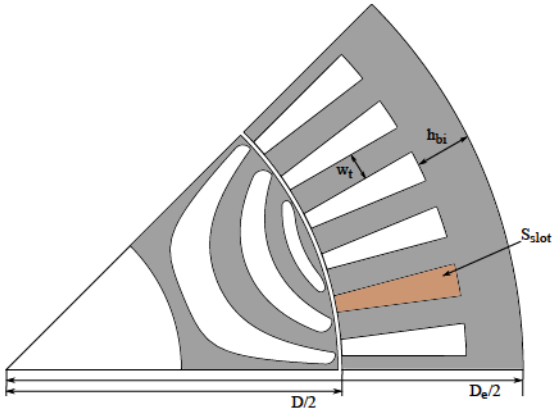

Figure 3.5: Simplified drawing of the REL machine.

3.4. Redesign of the REL machine

To improve the performance of the REL machine, the stator is redesigned with respect that of the LS 600h motor. The design has several degrees of freedom, but still with some constrains. In particular, the stator outer diameter, stack length, slot fill factor, voltage limit, and current limit are taken directly from the LS 600h motor. Hereafter, the design procedure is discussed.

3.4.1. Split ratio optimization

The split ratio (χ) is defined as the ratio between stator inner and outer diameter, *i.e.*, χ=D/D_e. The torque of an electric machine can be expressed as

$$T = \frac{1}{4} k_w Q_s n_{cs} \hat{I} \hat{B}_g L_{stk} D_e \chi \tag{3.1}$$

where k_w is the winding factor, Q_s is the number of stator slots, n_{cs} is the number of series conductors per slot, $\hat{I}$ is the phase current peak value, $\hat{B}_g$ is the amplitude of the fundamental harmonic of airgap flux density, L_{stk} is the stack length, and D_e is the stator outer diameter. From (3.1), it is observed that the output torque is affected by the split ratio. The focus of this optimization lies on finding the optimal split ratio that achieves the highest torque.

In this analysis, the rotor parameters (barrier number, barrier end angles and k_{air}) are kept constant. The stator slot is considered trapezoidal shape, as shown in Fig. 3.5. The slot opening is determined by the stator tooth width, while the slot wedge height is neglected.

The flux density ratio β is defined as the ratio of airgap flux density $\hat{B}_g$ and stator teeth flux density B_t ($\beta = \hat{B}_g/B_t$). Then, the stator teeth width w_t is computed as

$$w_t = \beta \frac{\pi D_e}{Q_s} \chi \tag{3.2}$$

The stator back iron height h_{bi} can be calculated as

$$h_{bi} = \frac{1}{2\pi} \frac{Q_s}{p} \frac{B_t}{B_{bi}} w_t = \frac{1}{2\pi} \frac{Q_s}{p} \alpha w_t \tag{3.3}$$

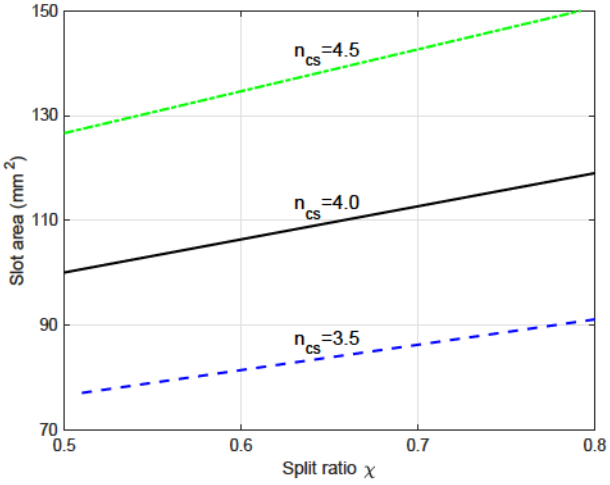

Figure 3.6: Variation of slot cross-area section with split ratio for a 48-slot 8-pole REL machine (n_{cs} is assumed to be 3.5, 4, and 4.5, respectively).

where B_{bi} is the flux density of the stator back iron. Here, another parameter $\alpha = B_t/B_{bi}$ is introduced. Considering the knee point of the iron laminations, this ratio is assumed to be constant and equal to 1.16. Finally, the slot area S_{slot} is represented as

$$S_{slot} = \frac{\pi D_e^2}{4Q_s}(f_a\beta^2 + f_b\beta + f_c) \tag{3.4}$$

where f_a, f_b and f_c are

$$\begin{aligned} f_a &= \frac{2\alpha}{p}\left(\frac{\alpha}{2p}+1\right)\chi^2 \\ f_b &= 2\left[\chi^2 - \left(\frac{\alpha}{p}+1\right)\chi\right] \\ f_c &= 1-\chi^2 \end{aligned} \tag{3.5}$$

Therefore, S_{slot} is found to be related to α, β, χ, Q_s, p and D_e. The next step is to determine the variation of slot area S_{slot} with split ratio χ, which is based on the assumption of constant copper loss.

The copper loss can be represented as:

$$P_{cu} = \frac{3}{2}R\hat{I}^2 = \frac{3}{2}\rho_{cu}\frac{L_{cond}}{S_{slot}k_{fill}}(n_{cs}\hat{I})^2\frac{Q_s}{m} = const \tag{3.6}$$

where ρ_{cu} is the copper resistivity, L_{cond} is the copper conductor length and m is the number of phases. L_{cond} is considered to include the stack length and the end-turn length, which is also related to the split ratio:

$$L_{cond} = L_{stk} + 2.5\frac{D_e\chi}{p} \tag{3.7}$$

From (3.6), all the parameters are constant except n_{cs}, χ and S_{slot}. Therefore, the variation of slot area S_{slot} with χ can be directly obtained once n_{cs} is given. The

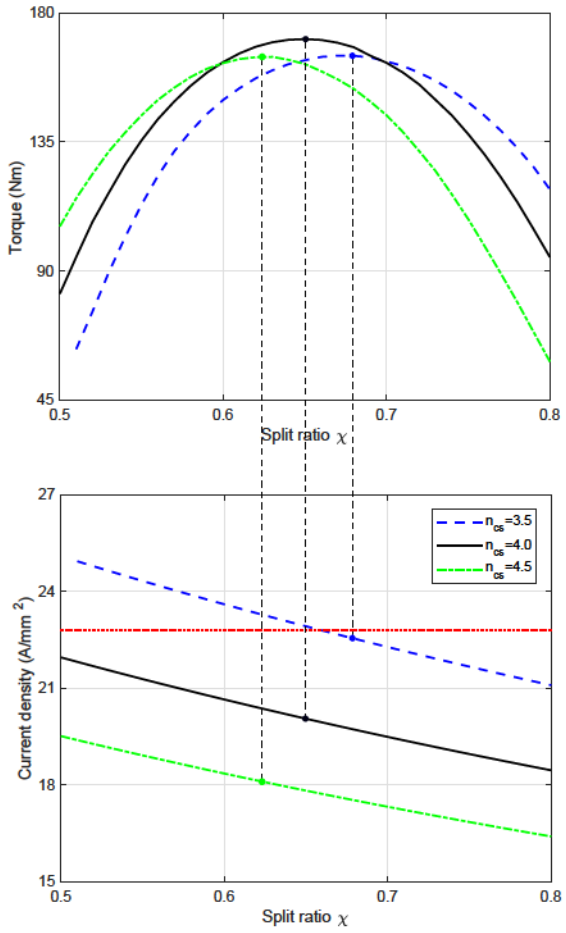

Figure 3.7: Variations of torque and current density with split ratio for a 48-slot 8-pole REL machine (n_{cs} is assumed to be 3.5, 4, and 4.5, respectively).

relationship of S_{slot}, n_{cs} and χ for a 48-slot 8-pole REL machine is plotted in Fig. 3.6. The results show that slot cross-area increases with both split ratio χ and n_{cs}.

After determining S_{slot}, (3.4) and (3.5) are combined together to calculate β, which results in

$$\beta = \frac{-f_b - \sqrt{f_b^2 - 4f_a f_c'}}{2f_a} \tag{3.8}$$

where

$$f_c' = f_c - \frac{4Q_s}{\pi D_e^2} S_{slot} \tag{3.9}$$

After that, w_t and h_{bi} are computed from (3.2) and (3.3), respectively. Finally, the stator geometry is obtained, and the torque is computed through FEA simulation. By using the automatic drawing and analyzing procedure, it is very fast to investigate the torque behavior for different split ratios.

The variation of torque with split ratio is shown in the upper plot of Fig. 3.7, while the corresponding current density in the windings is plotted below. Evidently, there

Table 3.3: The Selected Slot-pole Combinations

Q_s	p	q	winding factor	$n_{cs_{opt}}$	χ_{opt}	T_{max}
24	2	2	0.966	7.5	0.54	154.5
36	2	3	0.960	5	0.54	161.9
48	2	4	0.958	3.5	0.56	158.9
36	3	2	0.966	5	0.61	171.5
54	3	3	0.960	3.5	0.60	179.0
72	3	4	0.958	2.5	0.62	176.3
48	4	2	0.966	4	0.65	170.9
72	4	3	0.960	2.5	0.66	177.5
96	4	4	0.958	2	0.65	176.8

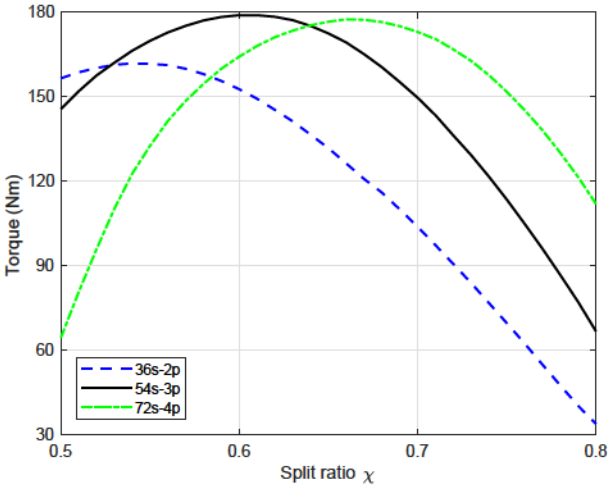

Figure 3.8: Variations of torque with split ratio for slot-pole combinations with $q = 3$.

exists an optimal split ratio to achieve the highest torque, and this optimal split ratio changes with n_{cs}. On the other hand, the split ratio is constrained by the current density limit (shown by the dotted line in the lower plot of Fig. 3.7), which is fixed to 22.8 A/mm^2 (reduced from 25 A/mm^2 due to the trapezoidal slot shape). With the decrease of n_{cs}, the current density tends to overcome this limit. Consequently, the calculation of current density is required during the optimization process, and the candidates with current density beyond the limit are discarded. The maximum torque obtained from Fig. 3.7 is 170.9 Nm, with $n_{cs} = 4$ and $\chi = 0.65$.

3.4.2. Slot-pole combinations

In this analysis, different slot-pole combinations are taken into consideration, as listed in Table 3.3. They are selected when the number of slots per pole per phase q is 2, 3 and 4, in addition, the pole-pair is 2, 3 and 4, respectively.

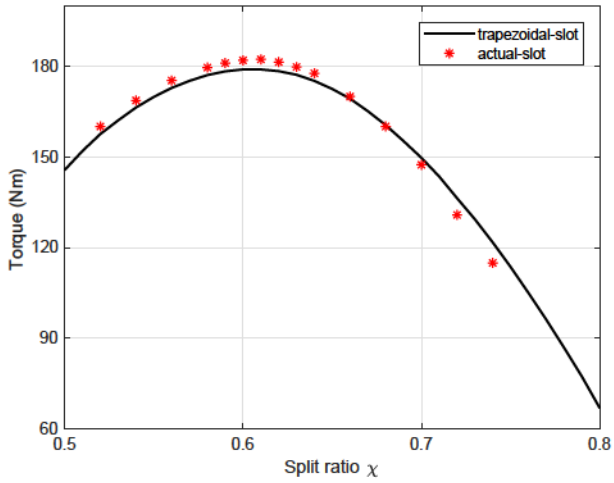

Figure 3.9: Torque versus split ratio comparison between the ideal "trapezoidal-shape" slot and the "actual-shape" slot.

For each slot-pole combination, the split ratio optimization is carried out with the aforementioned procedure. After plenty of calculations, the maximum torque for each slot-pole combination is reported in Table 3.3, and the optimal n_{cs} and χ are also shown. It is interesting to find that the optimal split ratio is almost constant corresponding to the same pole-pair, while the optimal n_{cs} is inversely proportional to the slot number. The results also show that the slot-pole combinations with $q = 3$ exhibit the highest torque capability. The torque variations versus split ratio with the optimal n_{cs} of these combinations are plotted in Fig. 3.8. The optimal split ratio increases with the number of pole-pairs. The maximum torque of the 54s-3p combination, though not significantly different from the 72s-4p combination, is the highest. Besides, low number of pole-pair reduces the operating frequency, leading to low iron losses in the stator. Overall, the 54s-3p combination is chosen as the optimal competitor in this case.

Since this optimization process is based on a trapezoidal slot shape, the slot opening and wedge are then added to the stator geometry (the same values as the LS 600h motor). The slot area is no longer the same, and β has also to be changed to achieve the same copper loss. Fig. 3.9 shows the torque versus split ratio comparison between the ideal "trapezoidal-shape" slot and the "actual-shape" slot (including wedge and slot opening). As expected, the trend of torque variation is almost the same. Finally, the optimal split ratio is selected to be 0.6.

3.4.3. Rotor optimization

The rotor optimization process is the same as that described in Section 3.3. Additionally, efficiency is considered as the third objective, which is obtained from the loss calculation. The copper loss is always the same, since it is kept constant. For simplicity, the iron losses are calculated as follows

$$P_{fe} = k_{magg_t} p_{sp_t} G_t + k_{magg_{bi}} p_{sp_{bi}} G_{bi} \tag{3.10}$$

where k_{magg_t} and $k_{magg_{bi}}$ are manufacturing loss increase factor in teeth and back iron, respectively. G_t and G_{bi} are weight of teeth and back iron, and the specific losses (in

Table 3.4: Values of the Optimal REL Rotor Parameters

Parameters	k_{air}	θ_{b1}	θ_{b2}	θ_{b3}
Values	0.44	15.0^o	21.5^o	27.2^o

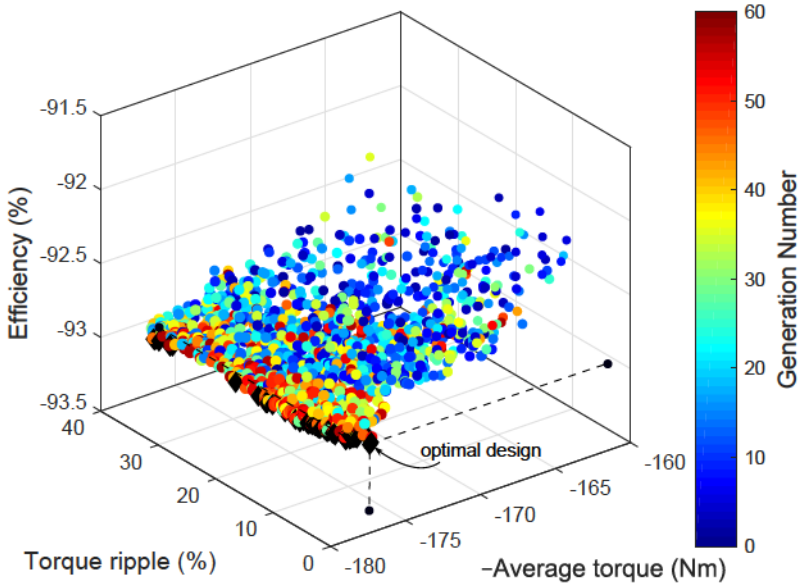

Figure 3.10: Optimization results with 54s-3p combination.

teeth and back iron, respectively) are computed as

$$
\begin{aligned}
p_{sp_t} &= p_{sp_{fe}} \left(\frac{B_t}{B_{ref}}\right)^2 \left[k_{hy}\left(\frac{f}{f_{ref}}\right) + k_{ec}\left(\frac{f}{f_{ref}}\right)^2\right] \\
p_{sp_{bi}} &= p_{sp_{fe}} \left(\frac{B_{bi}}{B_{ref}}\right)^2 \left[k_{hy}\left(\frac{f}{f_{ref}}\right) + k_{ec}\left(\frac{f}{f_{ref}}\right)^2\right]
\end{aligned}
\tag{3.11}
$$

where the specific iron loss of iron laminations $p_{sp_{fe}}$ is the value at reference flux density B_{ref} and reference frequency f_{ref}. k_{hy} and k_{ec} are iron hysteresis loss coefficient and eddy current loss coefficient. f is the operating frequency, which is 225 Hz at the speed of 4500 rpm. B_t and B_{bi} are maximum flux density of teeth and back iron, which are obtained from the FEA simulations. The stray loss is considered as 10 % of the total losses ($P_{cu} + P_{fe}$).

Finally, a three-dimensional view of the results is plotted in Fig. 3.10. The black diamond points form the Pareto front. Since the average torque and efficiency variations on the Pareto front are not as significant as torque ripple, the optimal point is selected to achieve the minimum torque ripple. The projections of this optimal point on each plane are drawn by the black points in Fig. 3.10. The optimal REL rotor parameter values are shown in Table 3.4.

Table 3.5: Comparison of Main Design Characteristics

	IPM motor	REL motor	Unit
Number of stator slots	48	54	–
Number of pole pairs	4	3	–
Stator outer diameter	200	200	mm
Stator inner diameter	130.86	120	mm
Airgap thickness	0.89	0.89	mm
Shaft diameter	53	44	mm
Active stack length	135.4	135.4	mm
Tooth width	6	4.45	mm
Back iron thickness	13.32	14.81	mm
Slot opening	1.88	1.88	mm
Active volume	4.25	4.25	dm^3
Stator core mass	14.90	15.69	kg
Copper mass	3.03	4.51	kg
Rotor mass	9.67	5.93	kg
Magnet mass	1.35	0	kg
Total mass	28.95	26.13	kg
Material cost	184	58	€

3.5. Performance comparison between REL and IPM motors

Following the previous steps, the optimal REL machine has been determined. The IPM motor, on the other hand, is built according to the Lexus LS 600h motor dimension [42]. The remanent flux density of the rare-earth magnets is obtained from the back EMF test [42], which is 1.068 T. Hereafter, a detailed performance comparison between the REL and IPM motors is presented.

3.5.1. Design features

Table 3.5 summarizes the main design characteristics of the two motors. Despite of the same external dimensions, the machine geometries are totally different, as sketched in Fig. 3.11. It should be stated that the IPM rotor is a little bit different from Lexus LS 600h rotor, mainly on the shape of air slot in the rotor.

The copper consumed in the REL motor is considerably higher than that of the IPM motor, which is attributed to the higher slot area and longer end winding due to the lower pole-pair number. The mass of IPM rotor is higher, whereas it can be further reduced by introducing some holes.

The unit prices for iron lamination, copper, and NdFeB magnet are assumed to be 1, 8 and 100 €/kg, respectively. Comparing the total cost, the IPM machine is over

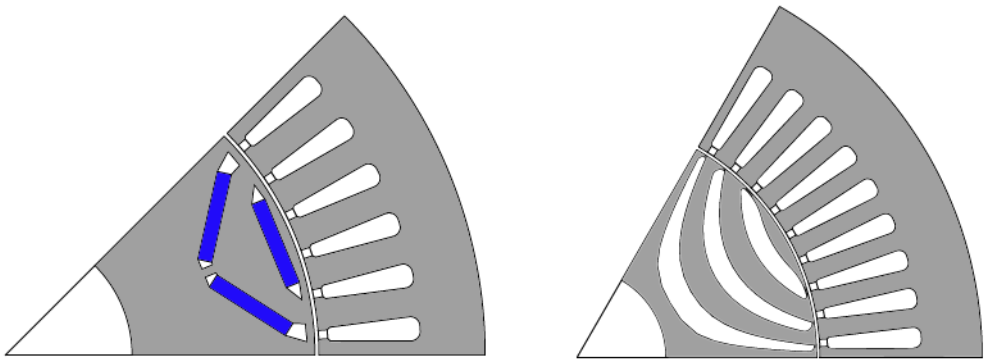

(a) The IPM motor. (b) The REL motor.

Figure 3.11: Cross-sections of the IPM and REL motors.

Table 3.6: Performance Comparison at Certain Condition

	IPM motor	REL motor	Unit
Current	330	330	A_{peak}
Operating speed	4500	4500	rpm
Current density	25.05	20.55	A/mm^2
Torque	241.5	176.0	Nm
Torque ripple	25%	4.1%	–
Power	113.8	82.9	kW
Torque density	56.8	41.4	Nm/L
Power density	26.8	19.5	kW/L
Specific power	3.9	3.2	kW/kg
Power factor	0.78	0.57	–
Efficiency	94.7%	93.6%	–

3 times of the REL one, which is mainly due to the high price of rare-earth magnets. More precisely, the rare-earth magnets contribute over 70% of the total cost, while they account for only small fraction of the total mass (less than 5%). As a consequence, the REL motor achieves a very low cost electric drive technology.

3.5.2. Torque and power capabilities

Generally speaking, the maximum torque and power capabilities of a motor is limited by both inverter maximum Volt-Amps rating and machine temperature rise. According to [42], the phase current peak value is set to be 330 A, and the maximum speed of constant torque operation is 4500 rpm. Table 3.6 shows the performance comparisons of the IPM and REL motors at this condition. The torque and power are regarded as the maximum torque and power of the motors. The corresponding torque waveform comparison is shown in Fig. 3.12. The REL motor exhibits quite low torque compared

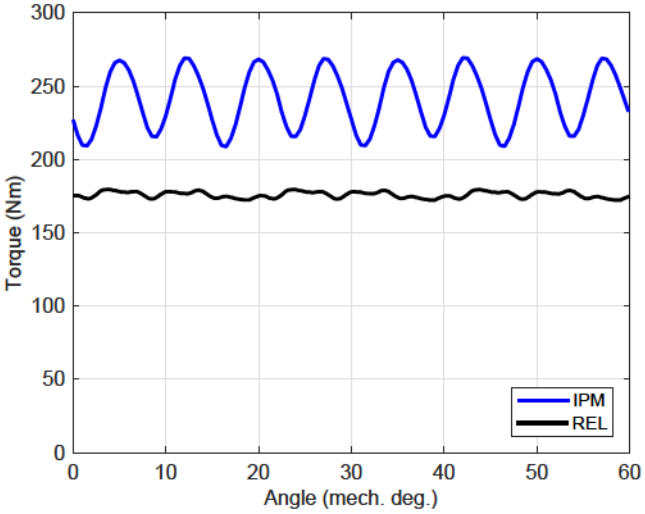

Figure 3.12: Comparison of torque waveform at maximum current.

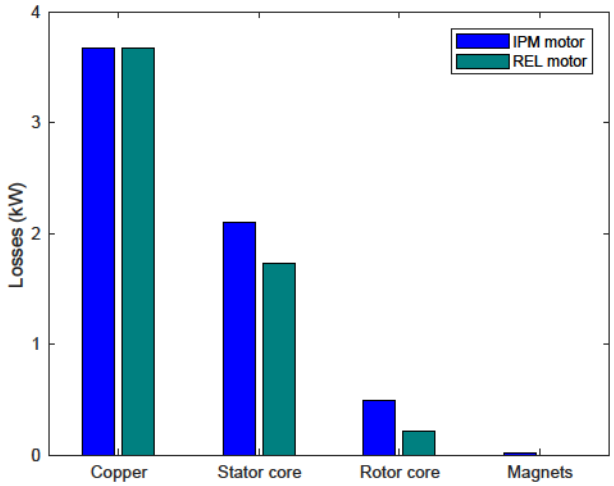

Figure 3.13: Comparison of loss components at the speed of 4500 rpm and maximum current.

to the IPM motor, which accounts for only 73%. Consequently, the power density and specific power of the REL motor are lower. The torque ripple of the IPM motor is quite high, which is due to the improper shape of air slots in the rotor. Thanks to the optimization process, the peak-to-peak torque ripple of the REL motor is considerable low even without rotor or stator skewing. One of the key problems with REL machine is the low power factor. As reported in Table 3.6, the power factor of the REL motor is only 0.57, while the IPM counterpart is 0.78. The low power factor will increase the inverter power rating.

It is worth noticing that the REL motor achieves comparable efficiency as the IPM motor. For a detailed inspection, loss components, including copper loss, stator core loss, rotor core loss and magnet loss are computed. The calculation method [49] considers a number of harmonics in the motor. It is achieved by a series of simulations with different rotor positions. When the PM loss is calculated, the reaction field of the induced eddy

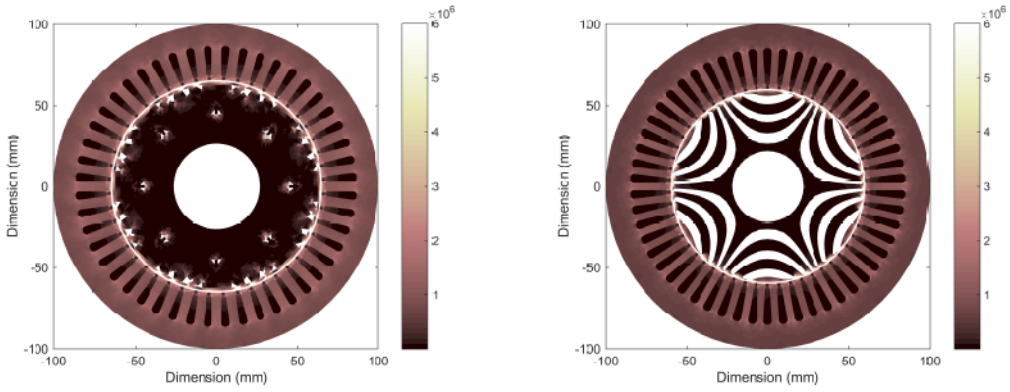

(a) The IPM motor. (b) The REL motor.

Figure 3.14: Comparison of loss density (W/m^3) distribution at the speed of 4500 rpm and maximum current.

currents is neglected [50].

A brief comparison of loss components is displayed in Fig. 3.13. The REL motor has lower iron losses both in the stator and rotor, and also has no magnet losses. As a consequence, the total produced losses in the REL motor is less, and a lower machine temperature rise is expected. Therefore, the output torque of REL motor can be further improved by using higher current within the same temperature rise. The loss density distribution of these two motors is plotted in Fig. 3.14. Low or no loss is represented by a dark color, while high loss is displayed in white. Overall, the REL motor shows a lower loss density distribution.

3.5.3. High speed flux-weakening capabilities

As far as the high speed FW capability is considered, the voltage rating of the inverter is quite important. The higher the voltage limit, the higher the operation speed. However, the DC bus voltage of the EVs is usually limited, and some control methodologies have to be adopted at high speed. The optimal current vector trajectory is achieved by means of FW control and MTPV control. Detailed explanations of these control algorithms are referred to Section 1.5. The obtained current vector trajectory is plotted in Fig. 3.15. Within the speed limit of 10000 rpm, the IPM motor follows only FW operation, while the operation of the REL motor covers both FW and MTPV.

The comparison of torque and power capabilities at different speeds of the two motors are plotted in Fig. 3.16. For high speed operations (over 4500 rpm), the constant power speed range (CPSR) of the IPM motor is wide, while the REL motor is quite limited. The results show that the power of the REL motor drops considerably and the power difference between the two motors increases with the speed. More specifically, the IPM motor delivers more than 130 kW at 10000 rpm, whereas the REL motor outputs only 45 kW. Therefore, the REL motor is not suitable for applications that require a wide CPSR.

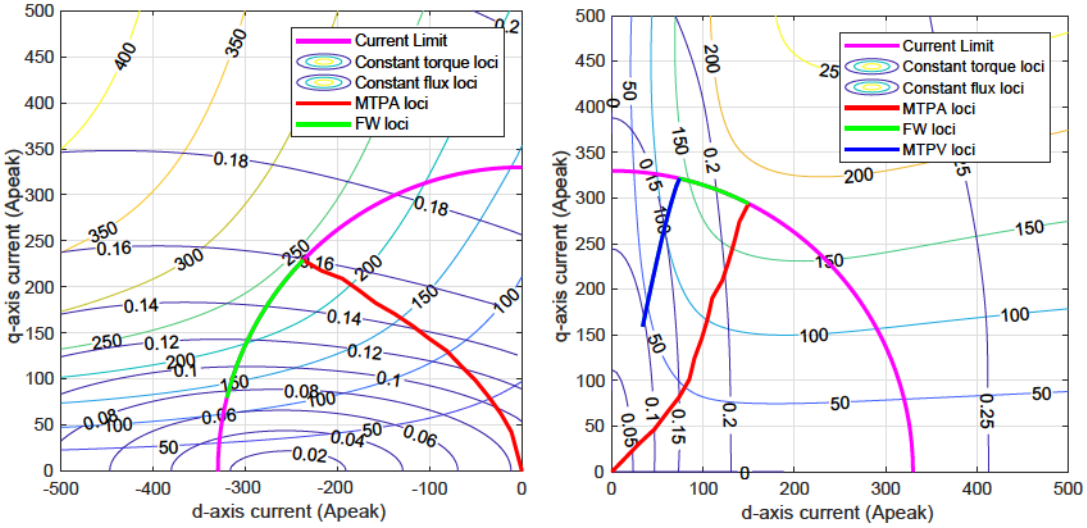

(a) Mapping of the IPM motor. (b) Mapping of the REL motor.

Figure 3.15: Comparison of current vector trajectory of the two motors.

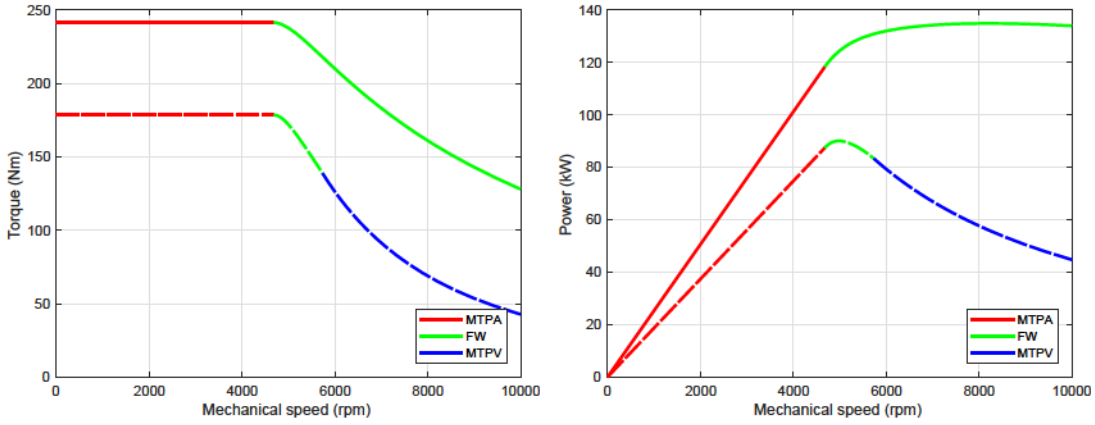

(a) Torque versus speed. (b) Power versus speed.

Figure 3.16: Comparison of torque and power variations versus speed of the two motors (the IPM motor: solid lines; the REL motor: dashed lines).

3.5.4. Efficiency

The efficiency maps of the two motors are compared in Fig. 3.17. They are obtained by considering copper loss, iron loss and also stray loss. The effect of temperature rise on the stator resistance is neglected. From the plots, some useful conclusions can be drawn.

Firstly, the maximum achievable efficiency is comparable between the two motors, which is 95% in the IPM motor and 94% in the REL motor. In addition, a large portion of the operating region achieves the efficiency above 90% in the REL motor. It is also worth noticing that the efficiency of the REL motor is higher than the IPM counterpart at high-speed low-torque conditions, which is highlighted by the dashed

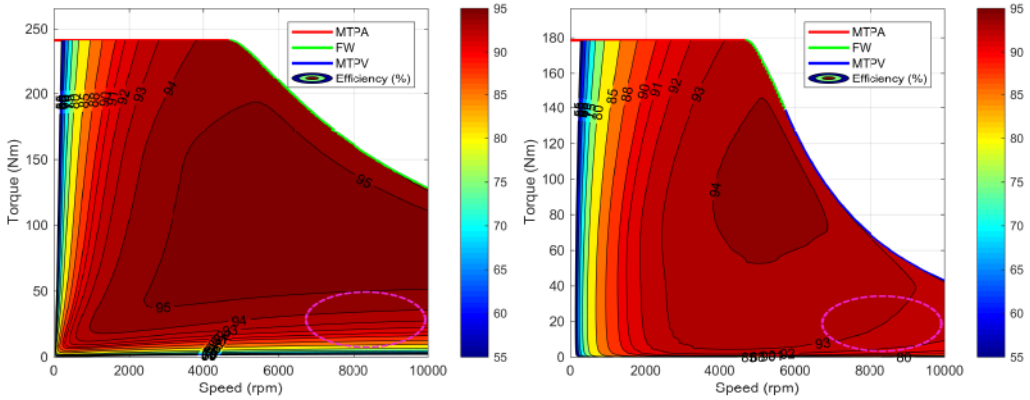

(a) Efficiency map of the IPM motor.

(b) Efficiency map of the REL motor.

Figure 3.17: Comparison of efficiency maps of the two motors.

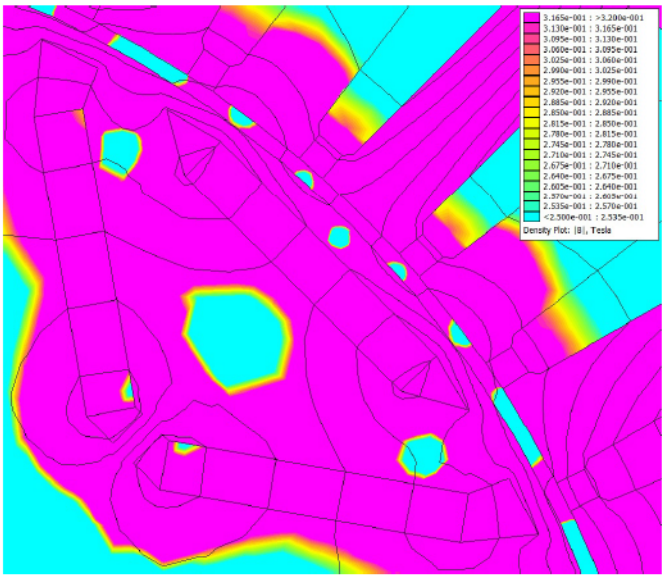

Figure 3.18: Flux density distribution of the IPM motor fed by d-axis current only ($I_d = -500$ A).

ellipses in Fig. 3.17. This is mainly due to the lower flux density of the REL motor at this condition.

3.5.5. PM demagnetization

Generally speaking, the PMs of the IPM machine has the risk to be demagnetized, which requires careful design. As reported in [42], the magnets used in the Lexus LS 600h is likely NMX-S41EH. The knee point of irreversible demagnetization is around 0.3 T at 150 °C. Fig. 3.18 shows the flux density distribution of the IPM motor fed by a demagnetizing current of 500 A. It is noticed that partial demagnetization occurs at this condition. Since this current is really high, it is demonstrated that the Lexus

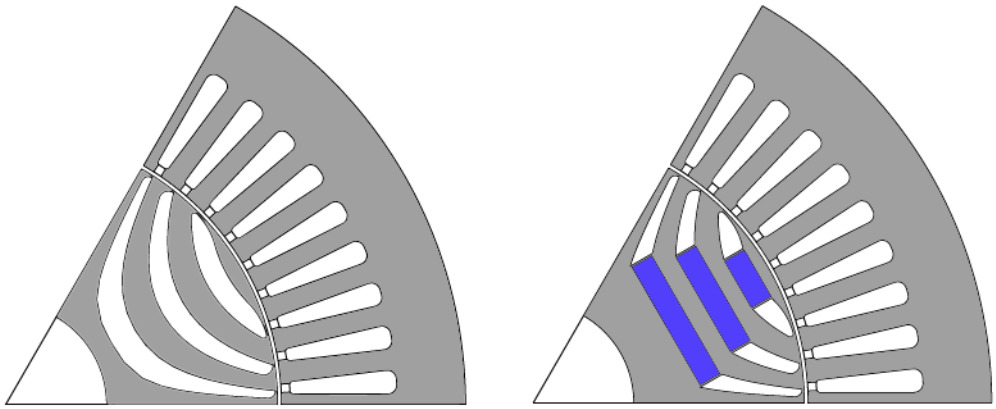

(a) The REL motor. (b) The PMAREL motor.

Figure 3.19: Cross-sections of the REL and PMAREL motors.

Table 3.7: Comparison of Main Design Characteristics

	IPM motor	REL motor	PMAREL motor	Unit
Number of stator slots	48	54	54	–
Number of pole pairs	4	3	3	–
Stator outer diameter	200	200	200	mm
Stator inner diameter	130.86	120	120	mm
Airgap thickness	0.89	0.89	0.89	mm
Shaft diameter	53	44	44	mm
Active volume	4.25	4.25	4.25	dm^3
Stator core mass	14.90	15.69	15.69	kg
Copper mass	3.03	4.51	4.51	kg
Rotor mass	9.67	5.93	6.20	kg
Magnet mass	1.35	0	1.39	kg
Total mass	28.95	26.13	27.79	kg
Material cost	184	58	79	€

motor is well designed. Anyway, the risk of irreversible demagnetization brings some challenges to the IPM machine.

3.6. Performance improvement with inset PMs

From the above analysis, it is concluded that the efficiency, torque density, power factor, and CPSR of REL motors are poorer than well-designed IPM motors. Referring to the analysis in Section 2.7, the added PMs in rotor flux-barriers not only increases the torque and power factor, but also improves the flux weakening capability of the REL machine. Therefore, ferrite magnets are used to improve the performance of the designed REL

Table 3.8: Performance Comparison at Certain Condition

	IPM motor	REL motor	PMAREL motor	Unit
Current	330	330	330	A_{peak}
Operating speed	4500	4500	4500	rpm
Current density	25.0	20.6	20.6	A/mm^2
Torque	241.5	176.0	192.8	Nm
Torque ripple	25%	4.1%	7.7%	–
Power	113.8	82.9	90.9	kW
Torque density	56.8	41.4	45.4	Nm/L
Power density	26.8	19.5	21.4	kW/L
Specific power	3.9	3.2	3.3	kW/kg
Power factor	0.78	0.57	0.67	–
Efficiency	94.7%	93.6%	94.3%	–

machine.

The residual magnetic flux density of the used ferrite magnet is **0.4** T, and the relative permeability is **1.05**. The unit price of the ferrite magnet is assumed to be **15** €/kg. For manufacture simplicity, the PM thickness in each flux-barrier is designed to be the same, which is **5** mm. The PM widths are **12**, **24** and **30** mm, from outer to inner flux-barriers. Finally, the cross-section of the PMAREL motor is shown in Fig. 3.19. As a comparison, the designed REL motor is again shown in Fig. 3.19. Due to the rectangular shape of the magnet, the iron channels are different between the two motors.

Similar to Table 3.5, the design characteristics of the PMAREL motor are compared with the IPM and REL motors in Table 3.7. Since the PMAREL motor is obtained from the REL motor, the stator keeps exactly the same. The main difference is the introduced PMs in the rotor. This increases the total rotor weight, and also the material cost of the machine. Comparing to the IPM motor, however, the total price of the PMAREL motor accounts for a proportion of only **43** %, which means a significant price advantage of the PMAREL machine.

The performance comparison at the peak current condition is shown in Table 3.8. Obviously, the torque of the PMAREL machine is higher than the REL one, with an improvement of around **10** %. Although this torque is still lower than the well-designed IPM motor employing rare-earth magnets, it can be further improved by enlarging the flux-barrier and insetting more ferrite magnets. Since this will lead to a new optimized PMAREL motor, it is skipped in this analysis. The added PMs may create some new harmonics interacting with the stator MMF, which causes a higher torque ripple in the PMAREL motor (from **4.1** % to **7.7** %). Anyway, the torque ripple can be even reduced by rotor step skewing or redesigned rotor flux-barriers. Regarding to the power factor, it is improved form **0.57** to **0.67**. It is interesting to notice that the efficiency of the PMAREL is also improved, which is only slightly lower than the IPM motor. This implies a high efficiency alternative with the PMAREL topology.

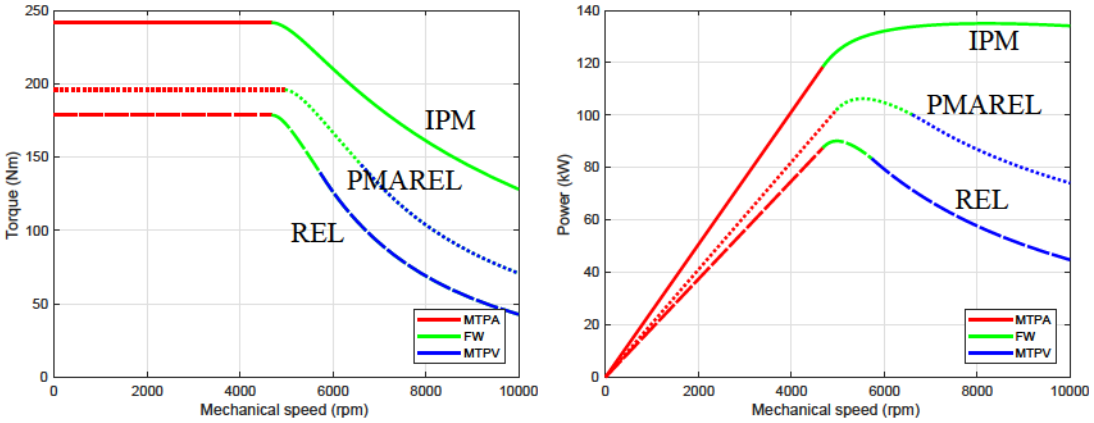

(a) Torque versus speed.

(b) Power versus speed.

Figure 3.20: Comparison of torque and power variations with speed.

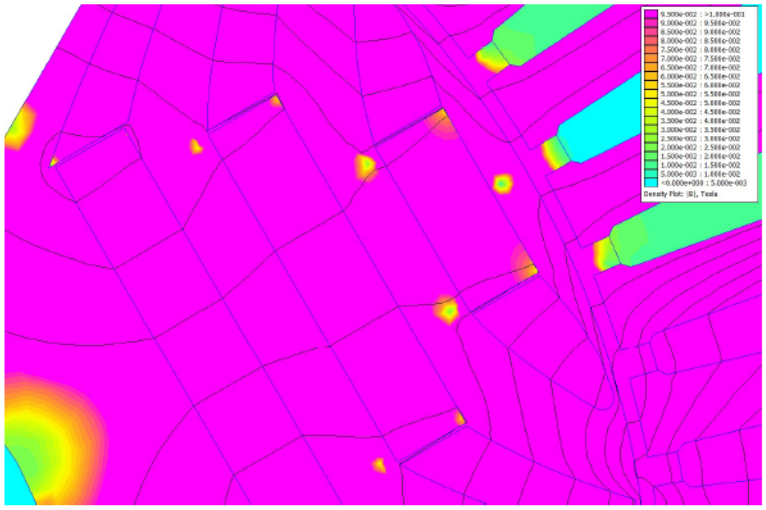

Figure 3.21: Flux density distribution of the PMAREL motor fed by q-axis current only (i.e., a demagnetizing current).

The comparison of the high speed flux-weakening capability is shown in Fig. 3.20. As expected, the CPSR of the REL motor is extended by insetting PMs, achieving better high speed flux weakening capability. On the other hand, the CPSR of the PMAREL motor is still not comparable with that of a well-designed IPM motor.

Due to the low coercivity of the ferrite magnets, the PMAREL machine may experience irreversible PM demagnetization problem at heavy load conditions. In any case, the risk of PM demagnetization should be carefully considered in the design. The flux density distribution of the PMAREL motor fed by fully q-axis current (**330** A_{peak}) is plotted in Fig. 3.21. Since the knee point of the ferrite magnetic curve is **0.02** T at **100** ^{o}C, no irreversible PM demagnetization occurs in this design.

3.7. Conclusion

In this Chapter, a design procedure of the REL motor is proposed, based on the dimension and performance of Lexus LS 600h motor. An analytical calculation is innovatively derived, and combined with FEA simulations to determine the optimal split ratio. The performance of the optimal REL design is also compared with the IPM motor.

The results of these comparisons show that the REL motor achieves the characteristics of significant cost saving (30 % of IPM), excellent efficiency (maximum 94 %), low torque ripple (4.1 %) and considerable power density (73 % of IPM). Despite of the low power factor, the REL motor has the potential to operate at higher temperature, due to the absence of magnets in the rotor and low rotor losses. Although the CPSR is very limited, it is capable of operating at high speed. It achieves reduced power instead of constant power, but with high efficiency.

To improve the performance of the REL design, ferrite magnets are inset into the rotor flux-barriers. With added PMs in the PMAREL motor, the torque density, efficiency and power factor are improved. Most importantly, it achieves better high speed flux weakening capability. The ferrite magnets may have the risk of demagnetization, but such a problem can be solved by improving the design of flux-barriers and PM thickness.

In conclusion, the PM motors will continue to dominate the traction market in the near future, while the REL and PMAREL motors show some attractive features. The REL motor can be possibly used for low-cost light-weight vehicle applications, and the potential competitive performance as rare-earth PM machines makes the PMAREL motors very promising.

Chapter 4

Investigation of Self-Excited Reluctance Generators

From this Chapter, attention will be paid on self-excited synchronous reluctance generators (SERGs). First of all, an analytical model in the d-q reference frame is developed to recognize the steady-state of SERG, considering no-load and resistive load conditions. Experiments are carried out to verify the analytical results. After that, some conditions which ensure a stable self-excitation in SERG, including required capacitance, rotor residual magnetism, rotor acceleration and pre-charging capacitors, are discussed. In addition, the effect of PM assisting on the SERG, i.e. self-excited PM-assisted reluctance (PMAREL) generator, is investigated. The characteristics of the self-excited PMAREL generator are presented analytically and experimentally. The effects of some design parameters (including stator resistances, d- and q-axis inductances) on the generator performance are also studied. Finally, the performance comparison of the self-excited PMAREL generator with SERG is carried out, highlighting the improvements of SERG by introducing PMs.

4.1. Introduction

IN recent years, the consecutive increase of energy demand and growing concern over air pollution have aroused great interest in renewable energy sources, such as wind, solar, tidal and hydroelectric. This has also led to extensive researches on suitable energy conversion devices in such generation schemes. For remote areas, in particular, an isolated stand-alone generating scheme is required. The conventional isolated power supply is the synchronous generator equipped with an external excitation system [51,52], which is not convenient for remote area applications.

The feasibility of using IMs as stand-alone generators by means of self-excitation was investigated and demonstrated in [53–55]. Self-excitation can be achieved with the capacitors, which are connected across the stator terminals [53]. When the machine is driven by a prime motor or other energy sources, a relatively insignificant voltage will be induced due to the rotor residual magnetism. The magnetizing current is then supplied by the capacitors and flows in the stator windings. This current helps to

increase the flux, and induces more voltages [56]. If this process continuously occurs, the machine will be saturated gradually. Then the machine will be operated at a stable condition. Comparing to the conventional synchronous generator system, the self-excited induction generator (SEIG) exhibits certain advantages, such as robustness, low cost, reduced size, high reliability, absence of DC source for excitation, and low maintenance requirements [57, 58].

Although the SEIG has been increasingly investigated for isolated applications, the frequency of terminal voltage is not fixed, which makes the prediction of its performance characteristics much more difficult [55]. The self-excited reluctance generator (SERG) has been demonstrated to be an alternative solution [59–62]. It achieves almost all the advantages of SEIG and, in addition, it owns the merits of fixed frequency at constant rotational speed and lower losses in the rotor [62].

According to the studies in the existing literature, some analytical models were built to analyze the performance of SERG. An approximate analysis was presented by Abdel-Kader [59]. He attempted to develop an equivalent circuit for the REL generator in the same manner as SEIG, without considering the effect of saliency ratio. Therefore, considerable error was resulted at load conditions. In [63], a two-axis theory was used to model and analyze a three-phase SERG which supplied an isolated *R-L* load. This theory was employed to account for the saliency effect and core losses. Mohamadien *et al.* [60,62,64,65] developed a model based on Park's *dq* axes transformation and demonstrated its validity both theoretically and experimentally. The predicted results show good agreement with experiments at open-circuit conditions, while visible discrepancy occurs at load conditions. A *dq* axes equivalent-circuit model based on eigen techniques was proposed in [66, 67], which was used to derive the dynamic equations of SERG. A simplified mathematical model was presented in [68].

In the following section, a simplified analytical model in the *dq* reference frame is developed to predict the steady-state performance of the SERG, considering no-load and resistive load conditions, respectively. Experiments by using a laboratory REL machine are also carried out to verify the analytical results.

4.2. Steady-state performance predictions of SERG

4.2.1. Analytical model of the SERG system

Referring to the motoring mode of the REL machine, the voltage equations are the same as (1.1). The flux linkage equations, on the other hand, are written as

$$\begin{cases} \lambda_d = L_d i_d + \Lambda_{res} \\ \lambda_q = L_q i_q \end{cases} \tag{4.1}$$

where Λ_{res} represents the rotor residual flux linkage.

Usually, REL machines are used as motors. They convert electric active power into mechanical power, and require reactive power for their magnetization. When they work as generators, they convert mechanical power into electric active power, but again require reactive power to magnetize their magnetic paths. Motoring operations are carried out when i_d and i_q exhibit the same sign, while generating operations when

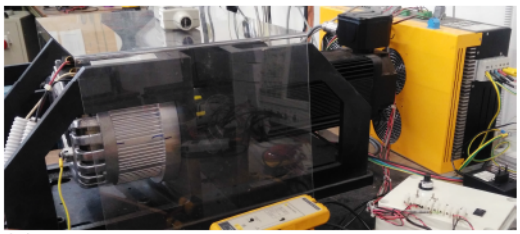

(a) The generator and the drive motor with inverter.

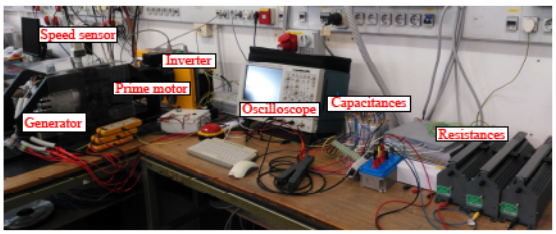

(b) Full view of the test bench.

Figure 4.1: The test bench of SERG experiment.

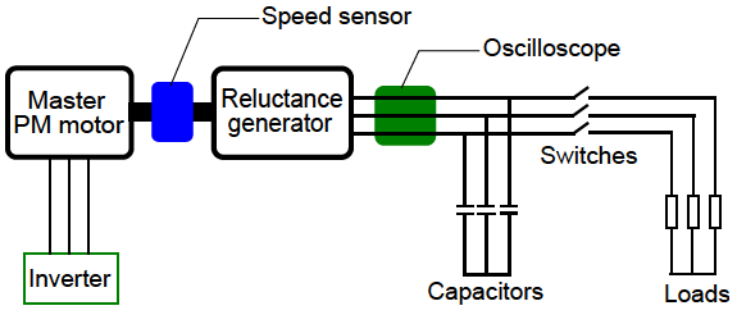

Figure 4.2: Scheme of the test bench.

they exhibit opposite sign. Referring to the (i_d, i_q) plane, motoring operations are in the first and third quadrant, conversely, generating operations are in the second and fourth quadrant.

Combining (1.1) with (4.1), the voltage equations of the REL generator are

$$\begin{cases} v_d = R_s i_d + L_d \dfrac{di_d}{dt} - \omega(L_q i_q) \\ v_q = R_s i_q + L_q \dfrac{di_q}{dt} + \omega(L_d i_d + \Lambda_{res}) \end{cases} \tag{4.2}$$

At resistive load conditions, both excitation capacitors and load resistors are connected to the generator terminals. After *abc* to *dq* transformation, dynamic equations of the capacitors and resistors are represented as:

$$\begin{cases} i_d = -C\dfrac{dv_d}{dt} - \dfrac{v_d}{R_L} + \omega C v_q \\ i_q = -C\dfrac{dv_q}{dt} - \dfrac{v_q}{R_L} - \omega C v_d \end{cases} \tag{4.3}$$

4.2.2. Experimental implementation

In order to investigate the SERG features, a test bench is set up in the laboratory, as shown in Fig. 4.1. The scheme of the test bench is described in Fig. 4.2. The generator is driven by a prime synchronous PM motor which is controlled by an inverter. The speed of the PM motor can be smoothly adjusted and measured. In order to provide

Table 4.1: Main Parameters of the Tested Reluctance Generator

Parameters	Symbol	Value	Unit
Stator outer diameter	D_{os}	200	mm
Stator inner diameter	D	125	mm
Airgap thickness	g	0.35	mm
Active stack length	L_{stk}	40	mm
Pole pairs number	p	2	–
Number of slots	Q_s	36	–
Number of barriers	N_b	3	–
Number of series conductors per phase	N_s	804	–
Base speed	n	1000	rpm
Rated current	I	6	A
Resistance per phase	R_s	4.6	Ω
Unsaturated d-axis inductance	L_{d0}	0.48	H
Saturated q-axis inductance	L_{qs}	0.04	H

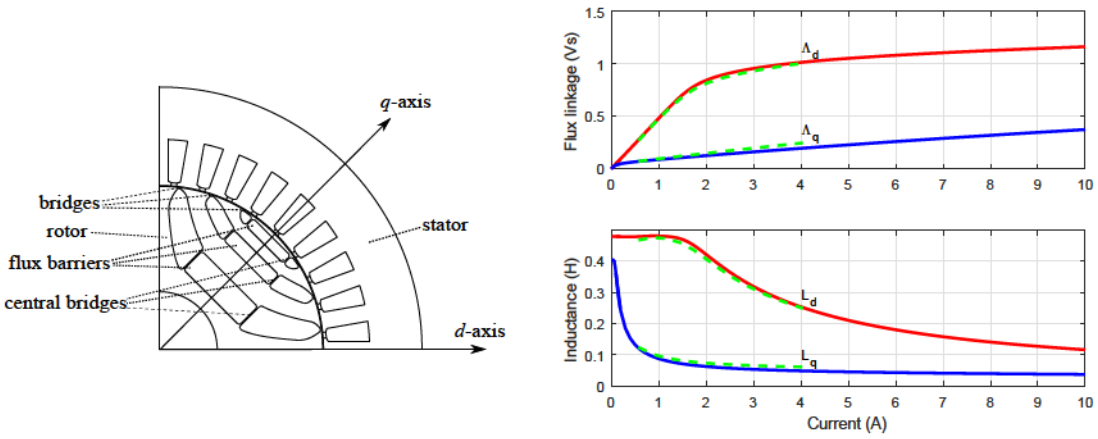

(a) Cross-section of the REL machine.

(b) d- and q-axis magnetizing curve.

Figure 4.3: Cross-section of the experimental REL machine and its d- and q-axis magnetizing curves (solid lines: simulations, dashed lines: experiments).

the REL generator with sufficient reactive power, a bank of three phase capacitors (C) are connected to the terminals of the stator windings, as shown in Fig. 4.2. Resistive loads are prepared to be connected through switches for load conditions. The capacitors and resistors can be either star or delta connected. In this test, all the capacitors and resistors are star connected.

The stator winding of the REL generator is also star connected. Main parameters of the generator are given in Table 4.1, with the cross-section shown in Fig. 4.3(a). Fig. 4.3(b) plots the d- and q-axis flux linkages and apparent inductances versus the d-

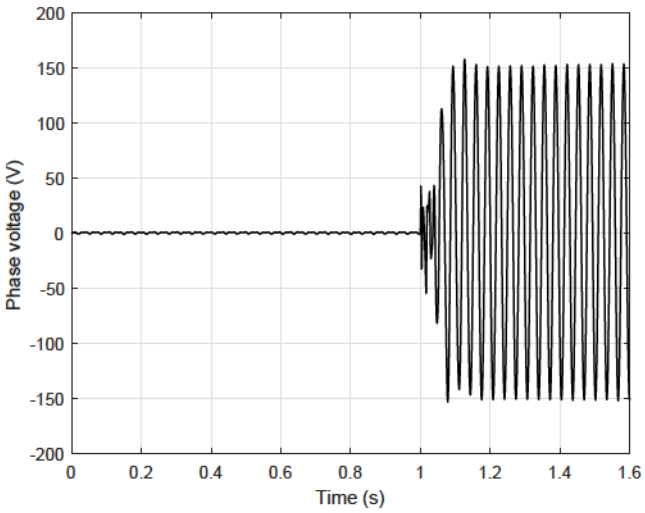

Figure 4.4: The experimental starting process of self-excitation in the REL generator with $C = 70$ μF at 915 rpm (capacitors are connected at $t = 1.0$ s).

and q-axis currents (peak phase value), respectively. The solid lines are obtained from two-dimensional (2D) FEA simulations, while the dashed lines are achieved by experiments. L_d keeps constant at low current while it decreases gradually when the current is higher than 1.2 Ampere (because of the iron saturation). Due to the existence of the bridges in the rotor, L_q is of high value at very low current (which is completely different from the conventional salient-pole REL machine), and then, it reduces significantly after the saturation of the bridges. It keeps almost constant when the phase current is higher than 2.0 A.

By using this test bench, experiments at no-load and resistive load conditions of the SERG have been carried out. Fig. 4.4 shows the experimental starting process of self-excitation in the REL generator with $C = 70$ μF at the speed of 915 rpm. Before $t = 1.0$ s, the bank of capacitors are disconnected. It is notable that a really negligible voltage is induced, due to the low residual magnetism in the rotor. At $t = 1.0$ s, the capacitors are suddenly connected to the stator terminals. The generated voltage rises rapidly, until certain saturation condition of the generator is reached. The process of self-excitation is achieved in a very short time.

4.2.3. Steady-state performance analysis

Under steady-state conditions, the time derivative terms in (4.2) and (4.3) are set to zero. Since the residual magnetism in the rotor is really low, it is neglected in the steady-state analysis. For simplicity, only the d-axis inductance is assumed to be affected by magnetic saturation in this analysis, while the q-axis inductance is considered to be constant. The saturated value of L_q is given in Table 4.1.

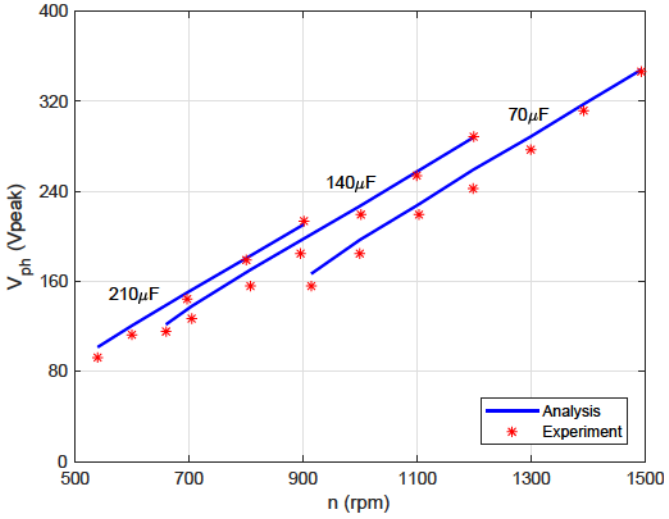

Figure 4.5: The no-load generated voltage against speed for different capacitors (70 μF, 140 μF and 210 μF, respectively).

A. No-Load Condition

At no-load condition, the terminals of the REL generator are connected to a bank of capacitors. The steady-state voltage equations are resulted as:

$$\begin{cases} V_d = R_s I_d - X_q I_q = -X_c I_q \\ V_q = R_s I_q + X_d I_d = X_c I_d \end{cases} \tag{4.4}$$

where X_d, X_q and X_c are the d-, q-axis inductive reactances and capacitive reactance, with $X_d = \omega L_d$, $X_q = \omega L_q$, and $X_c = 1/(\omega C)$.

When self-excitation of the SERG occurs with given capacitors, the main concern is the computation of the generated voltage. It starts from the calculation of the d-axis reactance, which can be directly derived from (4.4):

$$X_d = \frac{R_s^2}{X_c - X_q} + X_c \tag{4.5}$$

Under the assumption of constant q-axis inductance, X_d is obtained for given capacitive reactance X_c. Then the d-axis inductance is calculated by $L_d = X_d/\omega$. According to the d-axis magnetizing curve (shown in Fig. 4.3(b)), the d-axis current can be obtained by interpolation. After that, the d- and q-axis voltages are calculated again from (4.4), and the generated voltage is computed. It should be noticed that this calculation is carried out at given operating speed. Actually, different speeds drive the generator into different saturation conditions, and thus the generated voltage are different.

Fig. 4.5 shows the comparison of the voltages versus speed curves between the analytical and experimental results. Different capacitances are considered, which are 70 μF, 140 μF and 210 μF, respectively. V_{ph} refers to the peak value of phase voltage. The solid lines represent the analytical results, while the star points indicate the experimental results. Although the analytical values are slightly higher than the experimental ones, the differences are acceptable.

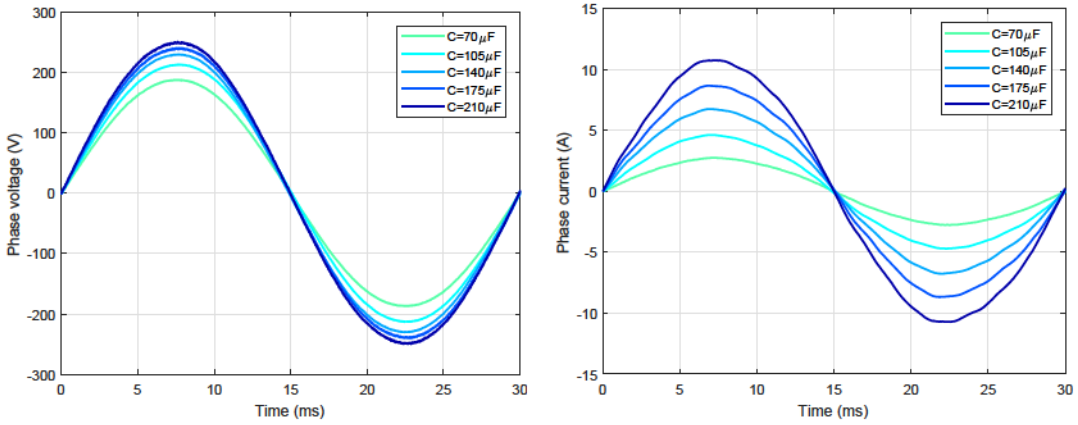

(a) Voltage waveform. (b) Current waveform.

Figure 4.6: The experimental no-load generated voltage and current at constant speed 1000 rpm with different capacitors.

It is also observed from Fig. 4.5 that with the increase of the speed under constant capacitor, the output voltage increases accordingly. Besides, larger excitation capacitance also leads to higher output voltage at the same speed. More specifically, Fig. 4.6 shows the experimental no-load voltage and current at 1000 rpm with C = 70, 105, 140, 175 and 210 μF, respectively. Sinusoidal waveforms are verified for both voltages and currents. It is worth noticing that their amplitudes increase with the capacitances. From the electromagnetic resonance point of view, the d-axis inductance reduces with the increase of capacitance at given speed, in order to achieve a stable resonance condition. Referring to Fig. 4.3(b), lower L_d means a higher amplitude of d-axis flux, and thus, a higher q-axis voltage. Since V_q is dominant in the output voltage, a higher terminal voltage is obtained with the higher capacitance.

This provides a method to maintain the generated voltage for varied speeds in wind power applications. When the driven speed is reduced, a corresponding reduction in the generated voltage occurs. However, it is possible to recover the voltage by increasing capacitances. Therefore, a stepwise-switched variable capacitor will be useful for the voltage regulation. Detailed discussion on determining the capacitance with variable speeds will be given in Section 5.3.

B. Resistive Load Condition

For resistive load condition, the capacitor C and the load R_L are parallel connected to the stator terminals, as shown in Fig. 4.7. Therefore, the impedance of C and R_L are represented as:

$$\dot{Z} = \frac{-jX_cR_L}{R_L - jX_c} = \frac{X_c^2R_L}{R_L^2 + X_c^2} - \frac{jX_cR_L^2}{R_L^2 + X_c^2} \tag{4.6}$$

Posing,

$$A = \frac{X_cR_L}{R_L^2 + X_c^2} \tag{4.7}$$

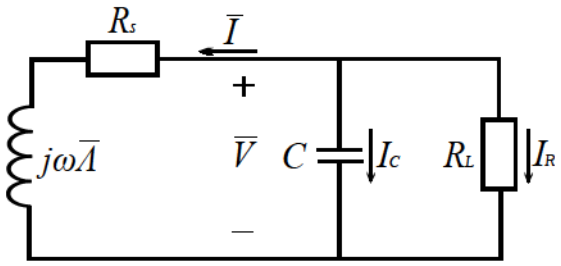

Figure 4.7: Circuit of the REL generator with capacitor C and resistive load R_L ($\bar{V}$=V_d+jV_q, $\bar{I}$=I_d+jI_q, $\bar{\Lambda}$=Λ_d+$j\Lambda_q$).

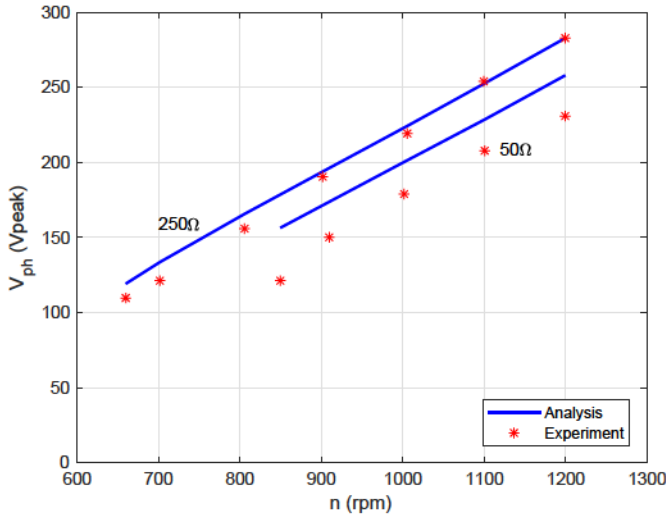

Figure 4.8: The generated voltage against speed with $C = 140$ μF, $R_L = 250$ Ω and 50 Ω, respectively.

then $\dot{Z} = AX_c - jAR_L$. Combining (4.2) with (4.3), the steady-state voltage equations are deduced to be:

$$\begin{cases} V_d = R_s I_d - X_q I_q = -A(X_c I_d + R_L I_q) \\ V_q = R_s I_q + X_d I_d = A(R_L I_d - X_c I_q) \end{cases} \tag{4.8}$$

Similar to the no-load condition analysis, the d-axis inductive reactance is expressed as:

$$X_d = \frac{(AX_c + R_s)^2}{AR_L - X_q} + AR_L \tag{4.9}$$

Therefore, the d-axis inductance at different speeds can be calculated according to the circuit parameters, and then obtained the d-axis current through interpolation of the magnetizing curve in Fig. 4.3(b). After that, the generated voltage can be computed again by using (4.8).

The comparisons of the generated voltage versus speed between analytical and experimental results are shown in both Fig. 4.8 and Fig. 4.9, considering $C = 140$ μF and $C = 210$ μF, respectively. Different load conditions, including $R_L = 250$ Ω and 50 Ω, are investigated. Actually, when the SERG is connected with load, it is really difficult to be self-excited. Due to the division of the stator current, the capacitor current

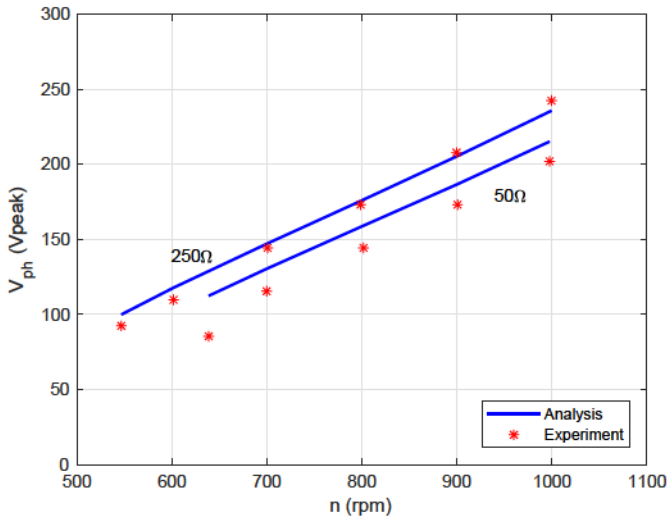

Figure 4.9: The generated voltage against speed with $C = 210\ \mu$F, $R_L = 250\ \Omega$ and $50\ \Omega$, respectively.

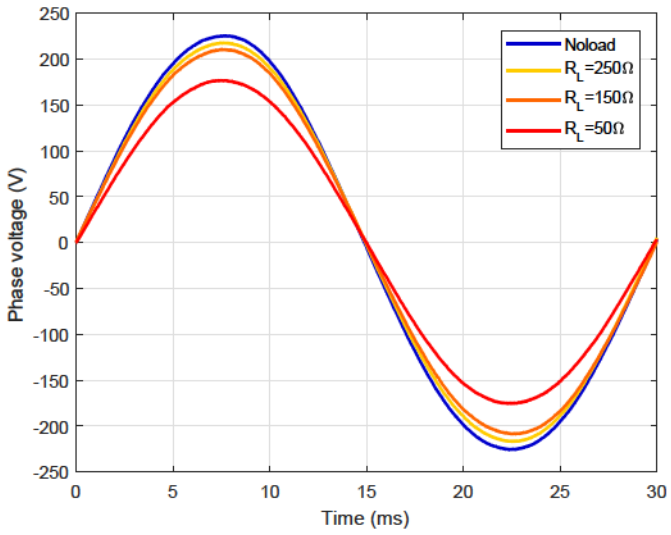

Figure 4.10: Comparison of experimental output voltage with different loads at the speed of 1000 rpm ($C = 140\ \mu$F).

is decreased, and then the induced voltage is reduced, either. Therefore, the generator is usually operated at no-load condition for initial start-up. Once self-excitation is achieved, the loads are connected to the generator terminals.

It is indicated from the figures that the analytical results are in good accordance with the experimental results at light-load conditions (that is $250\ \Omega$), while significant discrepancy is noticed at heavy-load conditions (that is $50\ \Omega$). This is mainly due to the effect of cross-saturation between d- and q-axis inductances, which will be dealt with in Chapter 5.

Besides, at the same speed, the output voltage of the REL generator connected with the same capacitor varies with load, as highlighted in Fig. 4.10. Apparent reduction is

noticed when the resistance is changed from 150 Ω to 50 Ω. This voltage drop can be attributed to the following reason. At no-load condition, the current phasor is almost along the d-axis. With the increase of load, the current phasor moves towards the q-axis. Therefore, the amplitude $|I_d|$ is reduced, while $|I_q|$ is increased. Referring to the left parts of (4.8), the amplitude $|V_d|$ is increased, while $|V_q|$ is reduced. Since V_q is dominant in the output voltage, the voltage decreases with the increase of load.

In conclusion, the amplitude of the generated voltage of SERG changes with rotor speed, capacitance and also load. It goes up significantly with increasing speed or capacitance, whereas drops with load. This simplified analytical model is useful to recognize the steady-state performance of SERG, and good agreement is obtained with experimental results.

4.3. Conditions for self-excitation in SERG

Undoubtedly, self-excitation is essential for REL generator to build up the voltage. Without self-excitation, the induced voltage of the REL generator is really insignificant even operated at extra-high speed. Hereafter, the conditions for initial self-excitation of SERG will be discussed.

4.3.1. Minimum required capacitance

Generally speaking, the process of initial self-excitation in SERG is achieved by electromagnetic resonance between capacitor and inductor. Therefore, the required capacitance is one of the most important factors for self-excitation. From (4.4), the capacitive reactance is expressed as follows:

$$X_c = \frac{(X_d + X_q) \pm \sqrt{(X_d + X_q)^2 - 4(X_d X_q + R_s^2)}}{2} \tag{4.10}$$

which indicates that there are two resonant points in SERG. Since X_d, X_q and R_s are parameters of the generator which can be known from simulations or experiments, it is convenient to obtain the minimum capacitance requirements at different speeds.

As a particular case, if R_s is neglected, (4.10) is deduced as:

$$X_c = X_d \qquad or \qquad X_c = X_q \tag{4.11}$$

Simply speaking, two resonance conditions are found: the first between the d-axis inductance and the capacitance, while the second between the q-axis inductance and the capacitance. Therefore, the required minimum capacitances at different speeds can be easily obtained as:

$$C_{min} = \frac{1}{\omega^2 L_d} \qquad or \qquad C_{min} = \frac{1}{\omega^2 L_q} \tag{4.12}$$

Due to the existence of flux-barriers in the rotor, L_d is always higher than L_q in the REL machine. Consequently, the required minimum capacitance is calculated from d-axis inductance only.

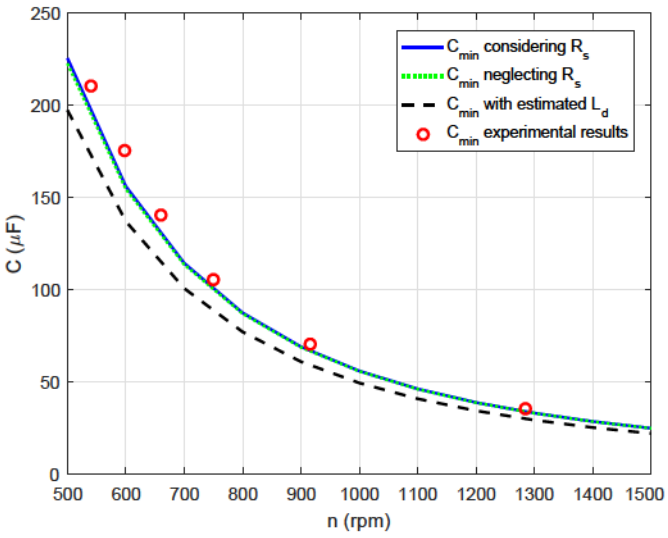

Figure 4.11: Minimum value of the capacitor for self-excitation versus speed, both analytical and experimental results.

For an analytical estimation of the resonance condition, L_d can be computed from the analytical expression, which is shown in (1.25). In this case, the required minimum capacitances are estimated from (4.12) and (1.25), even though the inductances of the generator are not measured or simulated.

Fig. 4.11 shows the comparison of the minimum capacitance obtained from the analytical model and experiments. The analytical model is used both considering and neglecting stator resistances, separately. Since the SERG has to be operated in the saturated region to guarantee self-excitation, the unsaturated d-axis inductance can not be selected. Here, L_d is chosen 0.41 H. The q-axis inductance is assumed to be constant, and equal to the saturated value (L_{qs} = 0.04 H). There is no significant difference of C_{min} considering or neglecting the stator resistances. The analytical results are verified by the experimental results. Fig. 4.11 also shows the calculated minimum capacitance through the estimation of L_d. Although this method obtains visible lower values of C_{min}, it is possible to achieve a fast estimation of the suitable capacitance for resonance.

4.3.2. Minimum rotor residual magnetism

Once the capacitor is properly selected, the circuit reaches resonance at a certain speed. However, only resonance cannot guarantee that the voltage of the REL generator increases up to the proper value. From the experimental tests, it is observed that if the residual magnetism in the rotor iron core is not high enough, the REL generator fails to reach high output voltage. Therefore, the residual flux linkage (Λ_{res}) in the rotor iron core is another key factor to assure self-excitation in SERG.

The airgap flux linkage due to residual magnetism can be calculated as:

$$\Lambda_{res} = E/\omega \tag{4.13}$$

where E is the back EMF at electric speed. The residual magnetism can then be represented by the back EMF at given speed.

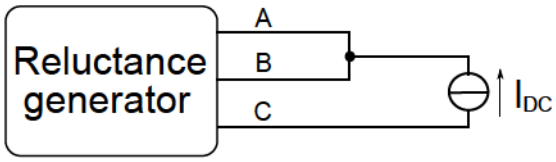

Figure 4.12: Scheme of magnetizing process.

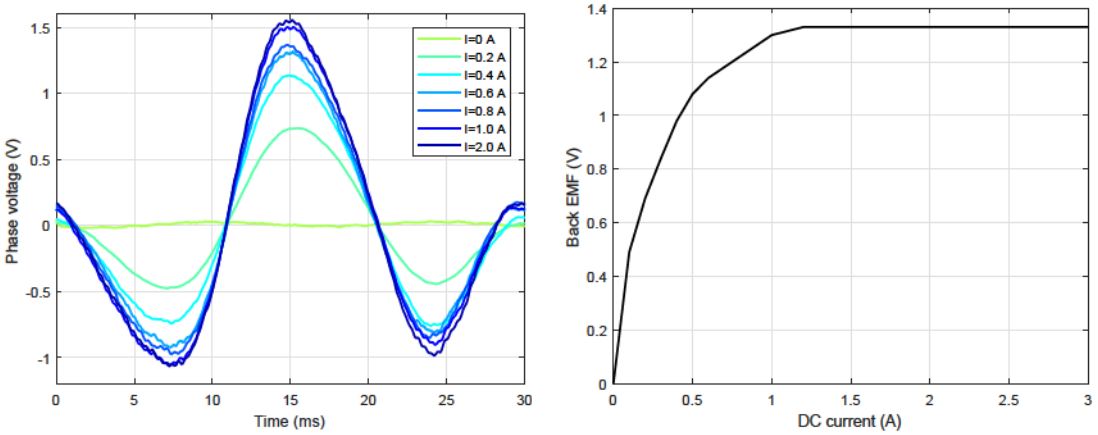

(a) Back EMF waveforms with DC current.

(b) Back EMF amplitude with DC current.

Figure 4.13: Variation of Back EMF waveforms and amplitude of the REL machine with different magnetizing DC currents at 1000 rpm.

Some experimental tests are carried out to obtain different magnetizations of the rotor paths. It is achieved by applying different amplitudes of DC current, as is shown in Fig. 4.12. For each time, the rotor is firstly demagnetized completely, and then the DC current is imported to the stator terminals. The demagnetizing process follows the property of the magnetic hysteresis loop, *i.e.*, with positive and negative current flowing through the stator winding alternately. The current value is reduced step by step until it is closed to zero.

The back EMF waveforms measured at 1000 rpm corresponding to different magnetizing DC currents are shown in Fig. 4.13(a). Their amplitudes are reported in Fig. 4.13(b) as a function of the DC current imposed during the magnetizing process. Even though the back EMF is quite low, it increases with the DC current. As a consequence, different levels of residual rotor magnetism are achieved by using different magnetizing DC currents. When the DC current is higher than 1.2 A, almost no variations are found between back EMFs, which implies that the maximum residual magnetism has been reached.

After that, the capability of SERG with different rotor residual magnetisms can be investigated. A bank of 140 μF capacitors are connected to the terminals of the SERG. Different DC currents are used to produce different residual magnetisms. The rotor speed is slowly changed during the experiments. The tested phase current versus speed are shown by the circles in Fig. 4.14. For low residual magnetism, the phase current has the maximum value at the resonance point; while for high residual magnetism, the phase current goes up rapidly until the process of self-excitation is finished and the

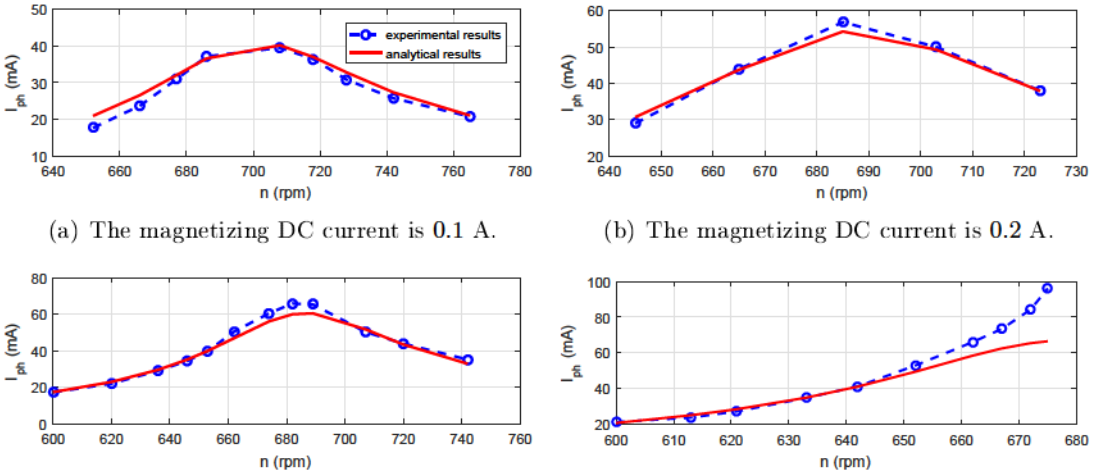

(a) The magnetizing DC current is 0.1 A.

(b) The magnetizing DC current is 0.2 A.

(c) The magnetizing DC current is 0.25 A.

(d) The magnetizing DC current is 0.3 A.

Figure 4.14: Variation of phase current versus speed after different DC magnetization ($C = 140\ \mu$F).

generator reaches high voltages. Based on these results, a simplified analytical model is proposed to compute the phase current:

$$I_{ph} = \frac{\omega \Lambda_{res}}{|R_s + j(X_c - X_L)|} \tag{4.14}$$

With this model, the behavior of phase current versus speed can be described, as shown by the solid line in Fig. 4.14. As far as the model is concerned, it is possible to observe that there is a satisfactory agreement between the predicted and experimental results. Only for phase current higher than 40 mA there is a discrepancy, since the measured currents result to be higher than the predicted ones. The reason is that the SERG starts to saturate. This model shows a rough approximation of the phase current before self-excitation.

It should be noticed that with 0.3 A magnetizing DC current, the REL generator connected with $C = 140\ \mu$F can be self-excited, as shown in Fig. 4.14(d). For $C = 70\ \mu$F, with lower residual magnetism (corresponding to the magnetizing DC current equals to 0.2 A) the generator starts to reach high voltages. While for $C = 210\ \mu$F, the minimum DC current is increased to 0.5 A, as shown in Table 4.2. Based on (4.14), an indicative value of the phase current is defined as:

$$I_{in} = \frac{\Lambda_{res}}{R_s \sqrt{LC}} \tag{4.15}$$

This value can be used to determine whether the REL generator with certain residual magnetism can be self-excited or not. Generally speaking, there is a minimum value of current, which is called I_{min}, to produce the minimum airgap flux linkage required for self-excitation [56]. In this case, I_{min} refers to the current when L_q changes rapidly, as is highlighted by point "A" in Fig. 4.15. When I_{in} is higher than I_{min}, it means the REL generator can be self-excited. According to Equation (4.15), higher capacitances

Table 4.2: Variation of Maximum Phase Current According to Different Magnetizing DC Current ($C = 210\ \mu$F)

Magnetizing DC Current (A)	I_{ph} (mA)	Statement
0.1	29.3	X
0.2	43.5	X
0.3	56.4	X
0.4	79.3	X
0.5		Self-excited

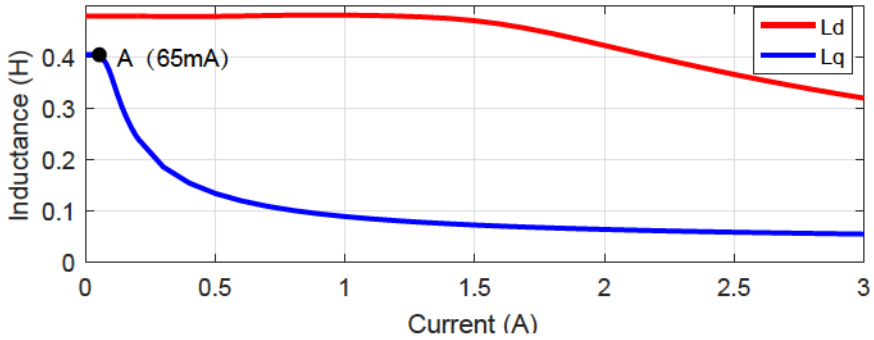

Figure 4.15: d- and q-axis inductances of the REL generator at low currents.

will cause lower I_{in} with the same residual magnetism, which means the capability of self-excitation of REL generator is decreased. This accounts for the reason that higher magnetizing DC current is required for generator with $C = 210\ \mu$F to be self-excited.

4.3.3. Rotor acceleration

During the experiment, it is also noticed that the self-excitation can be affected by the rotor acceleration. Several experiments are carried out on condition that the rotor is with the maximum residual magnetism. Rapid and slow rotor accelerations are achieved by controlling the master PM motor. The experimental results with two different rotor accelerations are shown in Fig. 4.16. The upper figures show the variation of speed, while the bottom figures refer to the variation of the generated voltage. With a rotor acceleration of 41.9 rad/s^2 (or 200 rpm/s), this generator is able to be fully self-excited. On the other hand, if the rotor acceleration is too high (doubled in this case), the REL generator fails to achieve self-excitation. It is advisable to provide a sufficient rotor residual magnetism and a low rotor acceleration in order to achieve a stable self-excitation process in the REL generator.

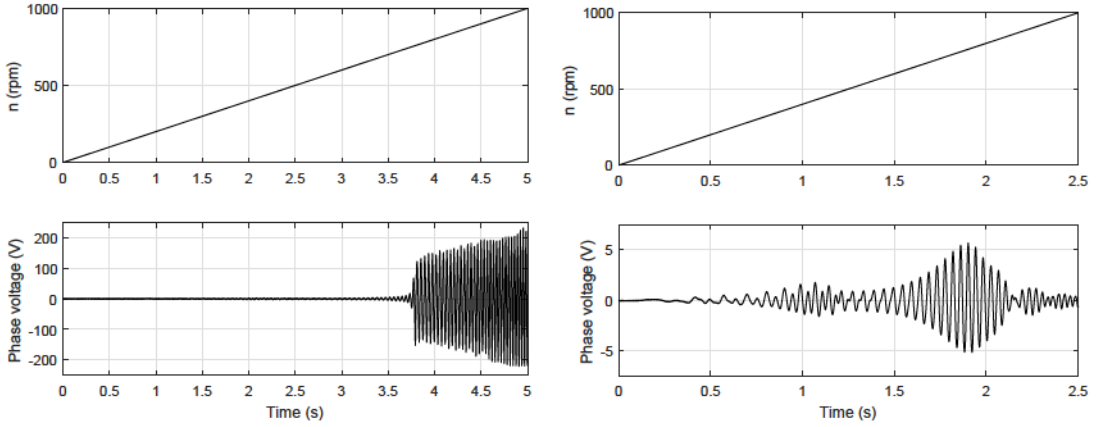

(a) The rotor acceleration is 41.9 rad/s^2. (b) The rotor acceleration is 83.8 rad/s^2.

Figure 4.16: Variation of self-excitation process with different rotor accelerations (experimental results).

Table 4.3: Line-Line Voltage with Different Charged Voltages in Capacitors ($C = 70\ \mu$F at the Speed of 951 rpm)

without C	with C	with charged C	charged voltage
0.24V	0.38V	300V	(+25V, 0V, -25V)
0.24V	0.38V	300V	(+20V, 0V, -20V)
0.24V	0.34V	300V	(+15V, 0V, -15V)
0.32V	0.64V	3V	(+10V, 0V, -10V)
0.24V	0.38V	0.38V	(+20V, +20V, +20V)

4.3.4. Pre-charging capacitors

An alternative method exists to trigger the self-excitation when there is no residual magnetism in the rotor, *i.e.*, pre-charging capacitors. Obviously, a DC voltage source or battery is required to pre-charge the capacitors. At the beginning, each capacitor is charged by the DC voltage source or battery. Then, when the generator is driven at a given speed, the charged capacitors are suddenly connected to the generator terminals. The voltage difference among each phase creates a transient current in the circuit. This current induces an initial flux in the generator, which is similar to the rotor residual magnetism. Once the induced flux is high enough, the self-excitation process will be achieved in the same manner.

The experiments are carried out with $C = 70\ \mu$F and results are shown in Table 4.3. When the charged voltages are different, the generator can be self-excited only if the voltages are high enough. As expected, if the charged voltages of the three capacitors are the same, no self-excitation will occur in the generator. This method is verified to provide a way to make the REL generator self-excite even with no rotor residual magnetism.

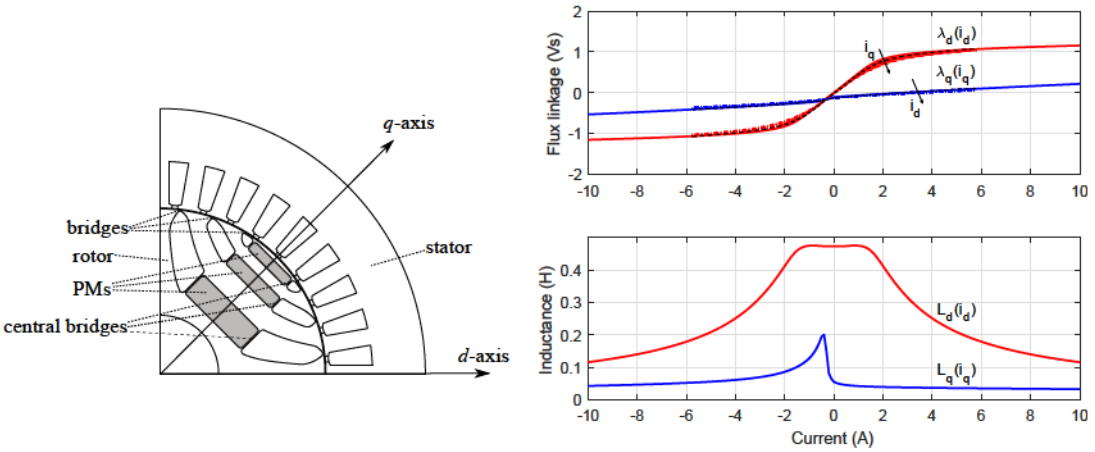

(a) Cross-section of the PMAREL machine.

(b) d- and q-axis magnetizing curve.

Figure 4.17: Cross-section of the experimental PMAREL machine and its d- and q-axis magnetizing curve (solid lines: simulated results, dashed lines: experimental results, dash-dotted lines: experimental results, almost superimposed).

4.4. Analysis of self-excited PM-assisted reluctance generators

As mentioned above, SERG has the difficulty to ensure a stable initial self-excitation process unless some conditions are satisfied. This drawback can be overcome by introducing PMs in the rotor flux-barriers of the REL machine, which is the same as PMAREL machine. In this section, the performance of self-excited PMAREL generator is investigated analytically and experimentally.

The test bench is the one shown in Fig. 4.1. The experimental PMAREL machine has the same geometry as the REL one, while the central barrier parts are inset with ferrite magnets as shown in Fig. 4.17(a). The remanent flux density of PM is **0.34** T, and the relative recoil permeability is **1.05**. Fig. 4.17(b) shows the d- and q-axis flux linkages and apparent inductances versus the d- and q-axis currents (peak phase value), respectively. The solid lines are obtained from 2D FEA simulations, while the dashed lines are achieved by experiments. The dash-dotted lines report the cross-saturation effect between the d- and q-axis, which is found to be negligible in this machine. As expected, λ_q is negative when $i_q = 0$ A, since the PM flux linkage is along the negative q-axis. L_d keeps the same trend as the REL machine, while L_q is always with low value since the iron bridges are saturated by the PMs in flux-barriers.

The back EMF versus speed curve of the PMAREL machine is plotted in Fig. 4.18. The solid line is obtained from simulation, while the crossing points are experimental results. The calculated PMs flux linkage Λ_m is **0.1123** Vs.

Fig. 4.19 shows the experimental starting process of the self-excited PMAREL generator with $C =$ **140** μF at the speed of **1000** rpm. v_{ph} represents the generated phase voltage. At the beginning, the PMAREL generator is driven to **1000** rpm, and then at $t = 1$ s, the capacitors are suddenly connected to the stator terminals. The output voltage rose to a high value rapidly, and the process of self-excitation is achieved.

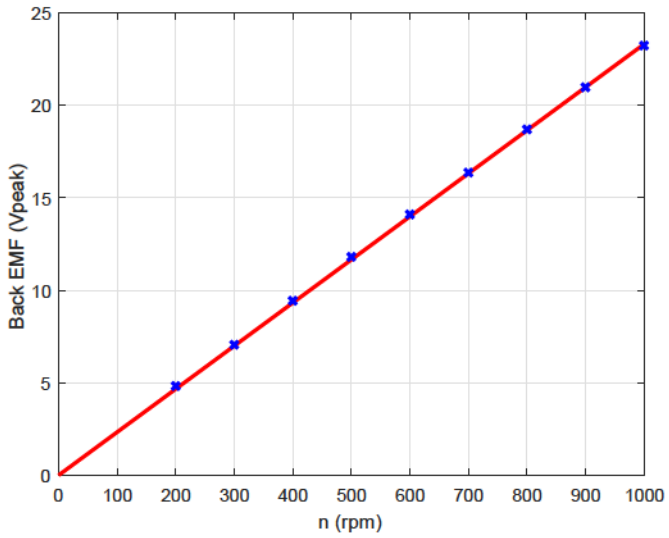

Figure 4.18: Back EMF versus speed of the PMAREL machine.

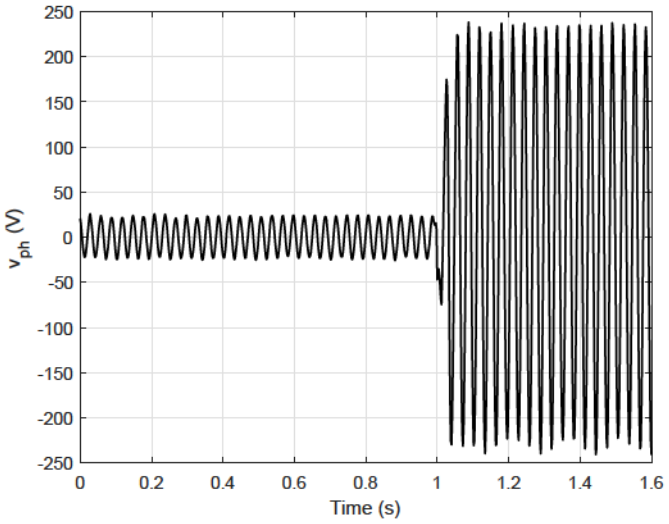

Figure 4.19: The experimental starting process of the self-excited PMAREL generator with $C = 140\ \mu$F at the speed of 1000 rpm.

4.4.1. Steady-state performance predictions

A. No-Load Condition

The no-load voltage equations of the self-excited PMAREL generator at steady-state are:

$$\begin{cases} R_s I_d - X_q I_q + \omega \Lambda_m = -X_c I_q \\ R_s I_q + X_d I_d = X_c I_d \end{cases} \tag{4.16}$$

which is very similar with (4.4).

At no-load condition, the operation of the PMAREL generator can be divided into two stages. They are distinguished by the minimum resonance speed (n_0), which is

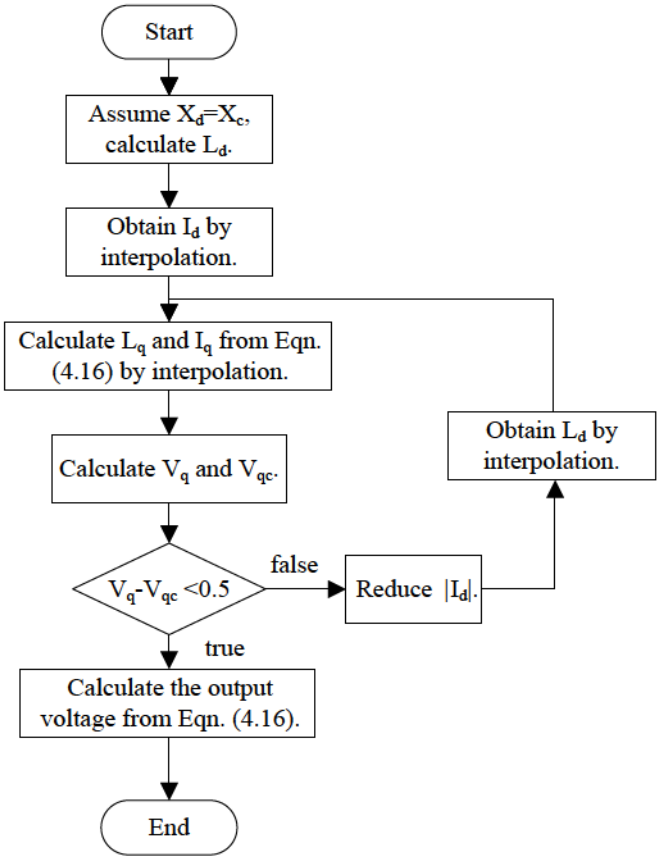

Figure 4.20: Procedure to calculate the generated voltage of the self-excited PMAREL generator.

defined as:

$$n_0 = \frac{30}{\pi p \sqrt{L_{d0} C}} \tag{4.17}$$

When the generator is driven at a speed lower than n_0, i.e., the first stage, no resonance exists. The phase current is so low that the d-axis inductance can be assumed to be constant, according to Fig. 4.17(b). Equation (4.16) is solved as:

$$(X_q - X_c - \frac{R_s^2}{X_c - X_d}) I_q = \omega \Lambda_m \tag{4.18}$$

Now, only I_q and X_q are unknown, which can be obtained from the interpolation of the q-axis magnetizing curve in Fig. 4.17(b). After that, current I_d and output voltage are calculated from (4.16).

At the second stage, the operating speed is higher than n_0, resonance happens and high output voltage can be achieved. The procedure to calculate the output voltage of the PMAREL generator is shown in Fig. 4.20. In this calculation, the q-axis inductance is not constant any more, but refers to the curve in Fig. 4.17(b). At the beginning, X_d is assumed to be equal to X_c, then L_d is calculated. I_d is obtained by using the interpolation of the d-axis magnetizing curve. With the first equation of (4.16), an equation is obtained with I_q and X_q unknown. Then, they are obtained by using the

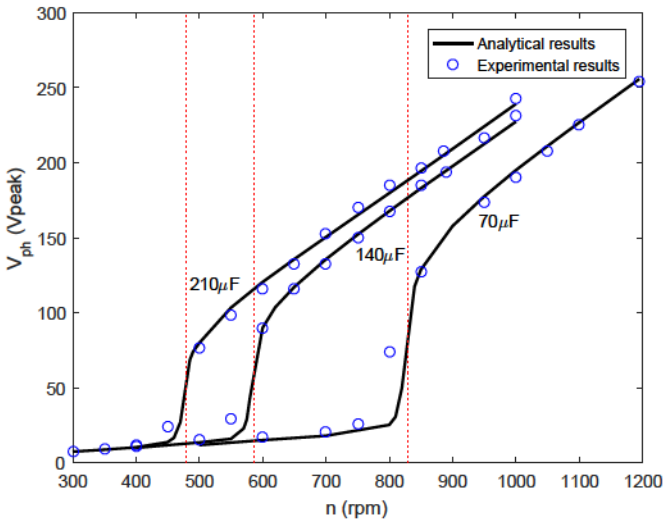

Figure 4.21: The no-load generated voltage versus speed for different capacitors (70 μF, 140 μF and 210 μF, respectively).

interpolation of the q-axis magnetizing curve. After that, V_q and V_{qc} are computed to be:

$$\begin{cases} V_q = R_s I_q + X_d I_d \\ V_{qc} = X_c I_d \end{cases} \tag{4.19}$$

The difference between V_q and V_{qc} is used to achieve a more accurate prediction of I_d and I_q. For PMAREL machines, generating operations are in the second quadrant, which means that I_d is negative. If the difference between V_q and V_{qc} is higher than 0.5 V (the threshold value), the amplitude $|I_d|$ is reduced. Then, L_d, L_q and I_q are recalculated. After several loops, the output voltage can be obtained until the difference between V_q and V_{qc} is lower than this threshold value.

Fig. 4.21 shows the no-load generated voltage versus speed for different capacitors. The solid lines represent the analytical results, while the circles indicate the experimental results. The dotted lines refer to the minimum resonance speed for each capacitor. It is verified that analytical values have no significant differences with the experimental results at the second stage. For the first stage, the analytical results are in accordance with the experimental results at low speed. When the operating speed approaches the minimum resonance speed, the difference between the two results is apparent, this may be due to the variation of the d-axis inductance at this condition.

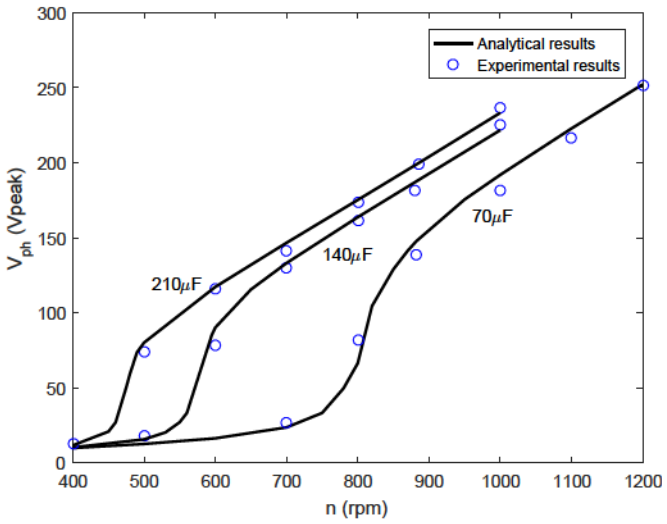

Figure 4.22: The generated voltage versus speed at resistive load conditions (R_L = 250 Ω, capacitances are 70 μF, 140 μF and 210 μF, respectively).

B. Resistive Load Condition

Similar to (4.8), the voltage equations of the self-excited PMAREL generator at resistive load condition are:

$$\begin{cases} R_s I_d - X_q I_q + \omega \Lambda_m = -A(X_c I_d + R_L I_q) \\ R_s I_q + X_d I_d = A(R_L I_d - X_c I_q) \end{cases} \tag{4.20}$$

Like the no-load condition, two stages are also identified to recognize the operation of the PMAREL generator at load condition. When the operating speed is lower than the minimum resonance speed, no resonance exists. The d-axis inductance is assumed to be constant. Equation (4.20) is modified as follows:

$$\begin{cases} I_d = \dfrac{R_s + AX_c}{AR_L - X_d} I_q = kI_q \\ (X_q - AX_c k - AR_L - R_s k) I_q = \omega \Lambda_m \end{cases} \tag{4.21}$$

Then, I_q and L_q can be calculated by interpolation, and the output voltage is obtained.

When the operating speed is higher than n_0, resonance happens and the same procedure can be used as the no-load condition to calculate the output voltage (as shown in Fig. 4.20). At resistive condition, V_{qc} becomes:

$$V_{qc} = AR_L I_d - AX_c I_q \tag{4.22}$$

After several steps, the voltage can be obtained. Fig. 4.22 shows the comparison of the output voltages between experimental and analytical results. Since no significant differences exist, the analytical model can be used to predict the performance of the self-excited PMAREL generator.

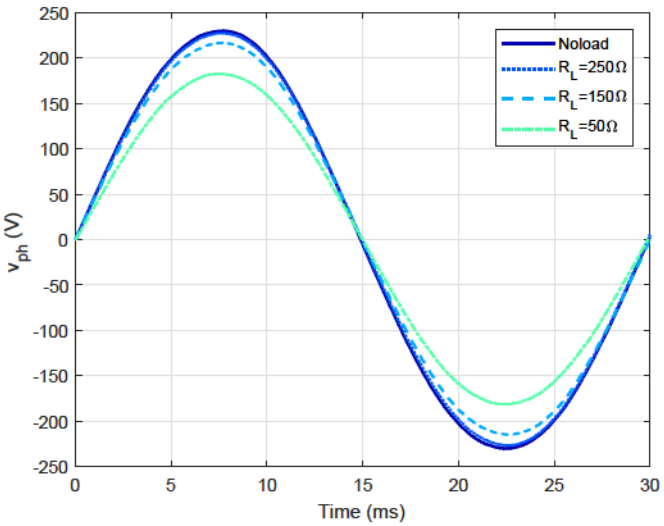

Figure 4.23: Comparison of experimental output voltage with different loads at the speed of 1000 rpm ($C = 140\ \mu F$).

4.4.2. Characteristics of the self-excited PMAREL generator

By using the test bench, a series of experiments are carried out on the self-excited PMAREL generator. A bank of three phase sliding resistors is used to change the load during the experiment, as shown in Fig. 4.1(b). The characteristics of the PMAREL generator are investigated as follows.

A. V_{ph} *Versus* n, C *and* R_L

As mentioned before, Fig. 4.21 and Fig. 4.22 show the generated voltage versus speed at no-load and resistive load ($R_L = 250\ \Omega$) conditions, respectively. It is observed that the output voltage increases with speed and capacitance, which is the same as SERG. Referring to the load, Fig. 4.23 shows the output voltage of the PMAREL generator with $C = 140\ \mu$F, $n = 1000$ rpm under different loads. The voltage waveform is very sinusoidal, and the voltage amplitude decreases with the load resistance, *i.e.*, when the load increases.

B. V_{ph} *Versus* P_{out}

Fig. 4.24 describes the load characteristics of the PMAREL generator, i.e., the variations of the generated voltage with output power (P_{out}) at the speed of 1000 rpm. The voltage variation is shown according to three values of capacitances, 70 μF, 140 μF and 210 μF, respectively.

As expected, the terminal voltage reduces continuously with load, while the output power experiences an increase first, and then decreases. Therefore, a maximum output power exists for a given capacitor. According to (4.6), with the increase of load, *i.e.*, when the load resistance decreases, the imaginary part of the impedance $\dot{Z}$ is reduced. Then the required d-axis inductance for resonance increases, which means lower d-axis

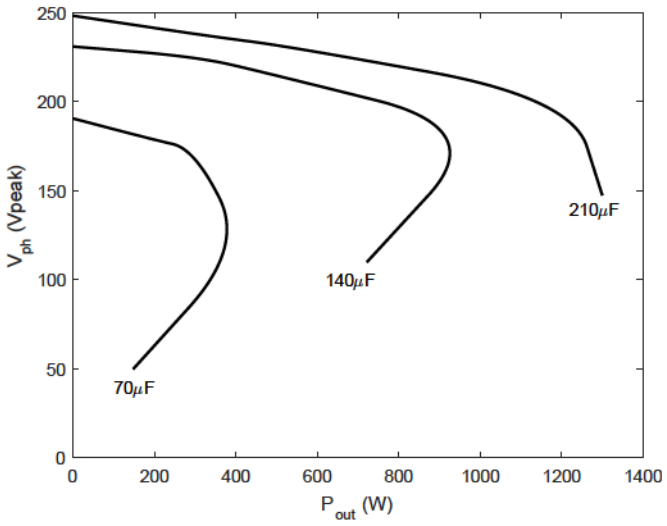

Figure 4.24: Variations of the generated voltage with output power for different capacitors at given speed (1000 rpm, experimental results).

flux and q-axis voltage. As can be seen in Fig. 4.17(b), the d-axis flux amplitude reduces slowly with increasing L_d when the current amplitude is high. This will cause a small reduction of the generated voltage, but an increase of output power (mainly due to the increase of load). When the current amplitude is small (less than 2 A for example), the d-axis flux reduces rapidly with increasing L_d, leading to a significant reduction of the generated voltage. Thus, the output power reduces. Therefore, the shape of d-axis flux limits the peak power that the REL generator can achieve with a given capacitor. Meanwhile, increasing the capacitance not only improves the output voltage, but also achieves a higher active power.

C. PF Versus P_{out}

Variations of PF with output power for different capacitors (70 μF, 140 μF and 210 μF, respectively) at the speed of 1000 rpm are shown in Fig. 4.25. It is observed that for low capacitances, the PMAREL generator is capable of achieving high power factor, but the output power is very limited. Conversely, for high capacitances, *e.g.*, $C = 210$ μF, the PMAREL generator exhibits 1301 W output power but with $PF = 0.67$.

D. PF Versus n

At constant resistive load condition ($R_L = 25$ Ω), the variations of output power and power factor with speed for constant capacitors are shown in Fig. 4.26. With the increase of speed, the output power increases while the power factor decreases. Therefore, it is difficult to achieve both high active power and high power factor.

To conclude, the self-excited PMAREL generator is capable of achieving almost sinusoidal voltage and relative high active power, which is suitable for isolated power supply applications. At given speed, the terminal voltage decreases continuously with the increase of load, while the output power is limited. High value of the capacitor helps

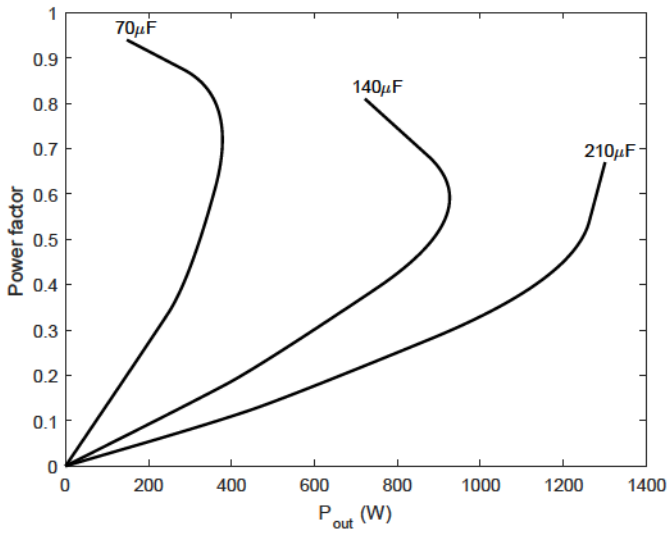

Figure 4.25: Variations of power factor with output power for different capacitors at given speed (1000 rpm, experimental results).

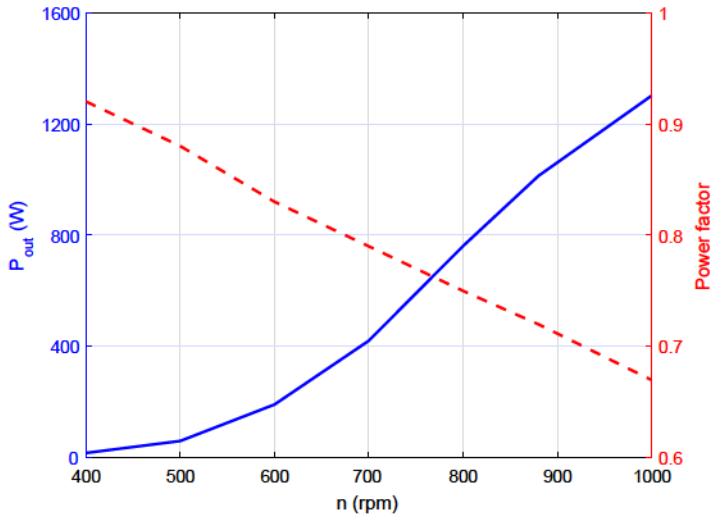

Figure 4.26: Variations of output power (solid line) and power factor (dashed line) with speed for $C = 210\ \mu$F (experimental results).

to increase the generated voltage and active power, on the other hand, the power factor is decreased. A trade off should always be made according to the operating conditions.

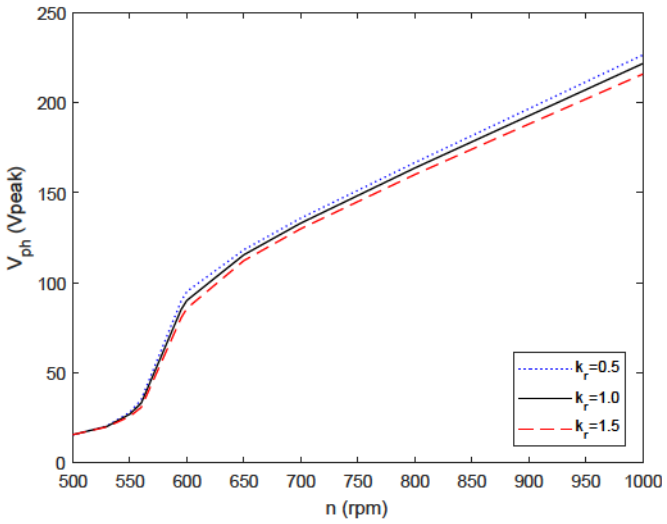

Figure 4.27: Effect of stator resistances on the generated voltage for $C = 140\ \mu F$ and $R_L = 250\ \Omega$ (analytical results).

4.4.3. Effect of design parameters on the PMAREL generator performance

In this part, the analytical model is used to investigate the effect of various design parameters on the performance of the self-excited PMAREL generator. The results may provide guidelines for the appropriate design of the PMAREL generator.

A. Effect of R_s

Fig. 4.27 shows the output voltages according to different stator resistances, which equal to $k_r R_s$. The results are provided for $k_r = 0.5$, 1.0 (the actual stator resistance) and 1.5, respectively. It can be noticed that the higher the stator resistances, the lower the generated voltage, and thus, the output power. Therefore, it is desirable to minimize the value of stator resistances, even though the effect of R_s is quite limited.

B. Effect of L_d

The effect of the d-axis inductance on the PMAREL generator performance is reported in Fig. 4.28. The behavior of the d-axis inductance is the same as in Fig. 4.17(b), but multiplied by a factor k_{Ld}, which is 0.8, 1.0 and 1.2, respectively. It is worth noticing that L_d has a significant influence on the generated voltage. At given speed, the generated voltage goes higher with increasing L_d, achieving a higher output power. Furthermore, the minimum resonance speed decreases with L_d, which can also be recognized from Equation (4.17). This means that the PMAREL generating system can be self-excited at lower speed with the same capacitor. As a consequence, in designing the PMAREL generator, high d-axis inductance is required to realize a super characteristic.

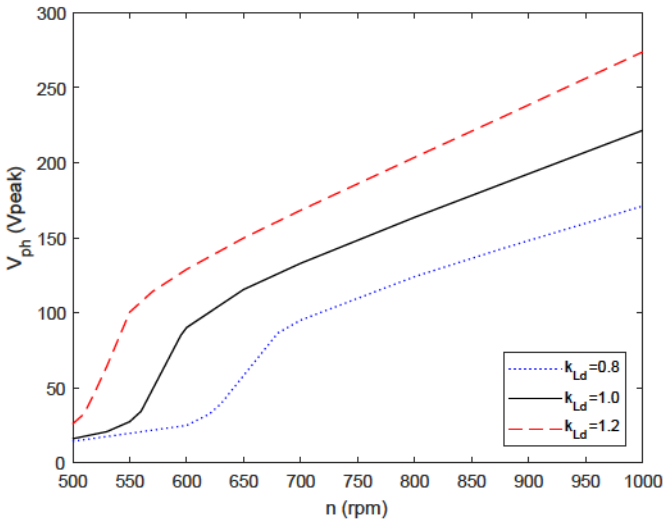

Figure 4.28: Effect of d-axis inductance on the generated voltage for $C = 140$ μF and $R_L = 250$ Ω (analytical results).

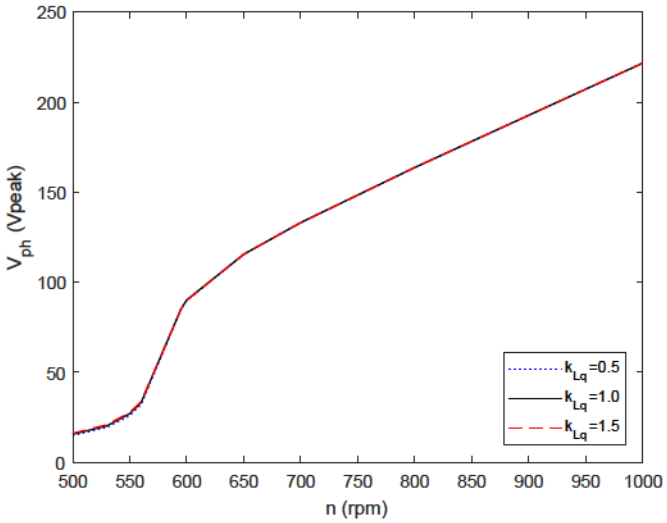

Figure 4.29: Effect of q-axis inductance on the generated voltage for $C = 140$ μF and $R_L = 250$ Ω (analytical results).

C. Effect of L_q

Fig. 4.29 shows the effect of the q-axis inductance on the performance of the PMAREL generator. A factor k_{Lq} is also used as before. Although k_{Lq} changes from 0.5 to 1.5, no variation is observed on the output voltage. As a result, no special consideration is required on the q-axis inductance when design the PMAREL generator.

In summary, it is shown that R_s and L_q contribute slightly to the generator performance, while L_d affects it significantly. The main idea for a PMAREL generator design is to increase L_d as much as possible, instead of increasing $(L_d - L_q)$ for a PMAREL motor design.

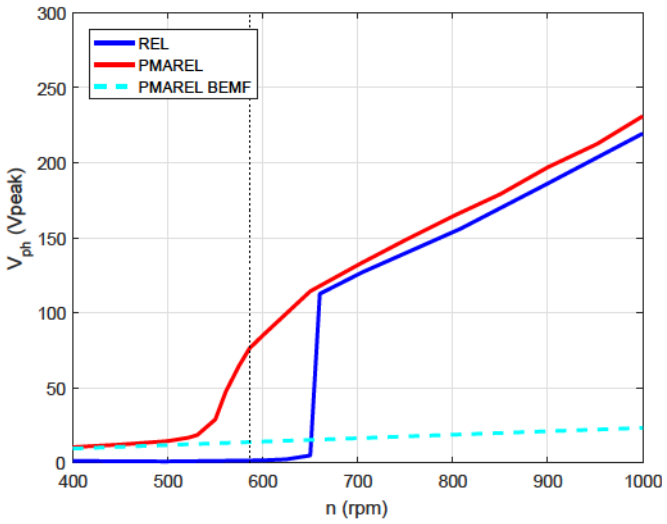

Figure 4.30: Comparison of the experimental no-load generated voltage at different speeds ($C = 140\ \mu$F).

4.5. Experimental comparison of the REL and PMAREL generators

As mentioned before, the only difference between the REL and PMAREL generators is the existence of PMs in the rotor flux-barriers. In this section, performance comparisons between the self-excited REL and PMAREL generators are presented, to highlight the improvements of the SERG system by introducing PMs.

4.5.1. No-load condition

The comparison of the no-load generated voltage of the REL and PMAREL generators is shown in Fig. 4.30. The dashed line represents the back EMF of the PMAREL generator, and the dotted line refers to the minimum resonance speed. As mentioned above, the operation of the PMAREL generator is divided into two stages by n_0. The minimum resonance speed of the REL generator should be the same as the PMAREL generator, since L_{d0} and C are the same. However, self-excitation of the REL generator occurs at a speed higher than n_0, which is mainly due to the low residual magnetism in the rotor. It is also demonstrated that if the residual magnetism is not high enough, the REL generator will fail to excite. From this point of view, the operation of the REL generator is critical and limited. On the contrary, the PMAREL generator can work at a speed around or even lower than the resonance speed, achieving a wider operating range than the REL generator.

During the transition between these two stages, the output voltage of the PMAREL generator increases slowly, while the REL one rises rapidly. For the second stage, the generated voltage of the PMAREL generator is higher when operated at the same speed.

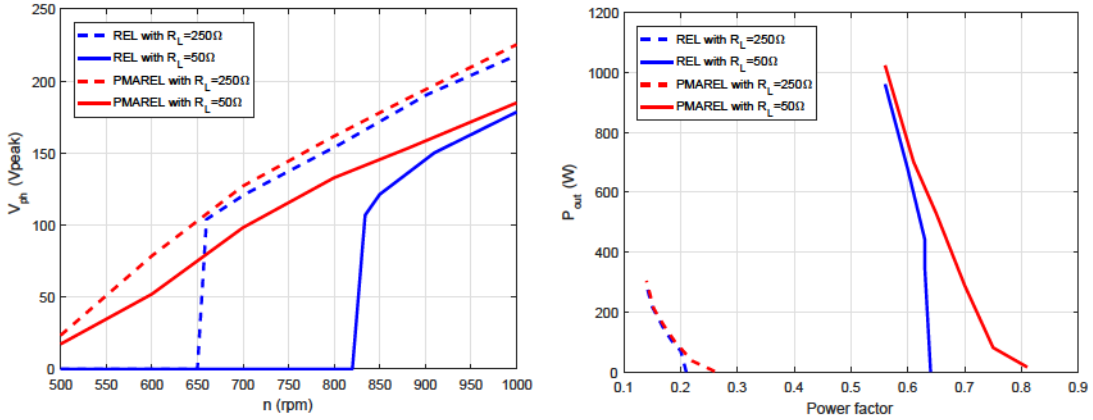

(a) V_{ph} versus n. (b) P_{out} versus PF.

Figure 4.31: Performance comparison of the REL and PMAREL generators at load conditions ($C = 140$ μF, experimental results).

4.5.2. Load condition

Fig. 4.31 shows the performance comparison of the REL and PMAREL generators at load conditions. Similar to the no-load condition, the PMAREL generator exhibits higher voltage, and thus, higher output power at given speed. Considering the same power factor, the PMAREL generator outputs more active power.

To sum up, the PMAREL generator shows the improvement of voltage, active power and power factor over the REL generator. Besides, a stable self-excitation process is inherently achieved by the inset PMs.

4.6. Conclusion

In this Chapter, the performance of self-excited REL generator, and then self-excited PMAREL generator, is investigated analytically and experimentally. It is verified that the generated voltage changes with rotor speed, capacitor and load. It goes up significantly with increasing speed or capacitor, while decreases with load. The existing problems related to successful self-excitation in SERG, such as minimum required capacitance, rotor residual magnetism, rotor acceleration and pre-charging capacitors, are also addressed. An appropriate capacitance is essential not only for self-excitation, but also for providing reactive power to the REL generator. It is also advisable to have a sufficient rotor residual magnetism and a low rotor acceleration in order to achieve a stable initial self-excitation process in the REL generator. In addition, the pre-charging capacitors provide a way to make the REL generator self-excite even with no rotor residual magnetism.

By using the analytical model, the effects of some design parameters (including R_s, L_d and L_q) on the generator performance are investigated, providing guidelines for a proper design of the PMAREL generator. Whereas small changes in the stator resistance and q-axis inductance do not affect its performance, the d-axis inductance is found to be very sensitive to determine the generated voltage.

Finally, the performance comparisons between the self-excited REL and PMAREL generators are carried out. It is highlighted that the self-excited PMAREL generator not only exhibits the improvement in terminal voltage, output power and power factor, but also achieves a stable self-excitation process. All the results are helpful for applications where REL or PMAREL machines are used as stand-alone generators.

Chapter 5

Self-Excited Reluctance Generators for Wind Applications

The SERGs have been found to be potential candidates as isolated generators. In this Chapter, the characteristics of SERG for wind turbine generation system will be focused on. The active and reactive power (PQ) balances are innovatively proposed, which helps to predict the performance of the SERG system. The FEA simulation results are employed to account for both saturation and cross magnetizing effect of d- and q-axis inductances. The procedure to determine the operating point according to PQ balances is proposed, and the influence of generator parameters, including stator resistance and inductances, is also investigated. After that, suitable capacitances for voltage regulation at variable speeds are determined by using the PQ balances. By considering a given wind turbine, the PQ balances are also used to determine the "optimal capacitor and resistor combination" that achieves the highest usage of wind power.

5.1. Active and reactive power balances

AS described in Chapter 4, the existed models provide valuable information about SERG, on the other hand, saturation on the q-axis inductance and cross-saturation effect are ignored. This leads to a significant discrepancy for the voltage prediction at heavy-load conditions. The importance of including magnetic saturation and cross magnetization in the analysis of REL machine was emphasized in [69–72]. Therefore, consideration should be taken upon them in order to achieve an accurate prediction of the REL generator performance. Guha *et al.* [73, 74] presented a linearized model of synchronous REL generator considering the effect of saturation in both d- and q-axis. It is demonstrated that the inclusion of q-axis saturation affects the generator performance at some operating conditions. However, no work by far involve the cross-saturation effect into the analysis of SERG. In the following parts, the prediction of SERG performance is achieved by using active and reactive power (PQ) balances, with the cross-saturation effect considered.

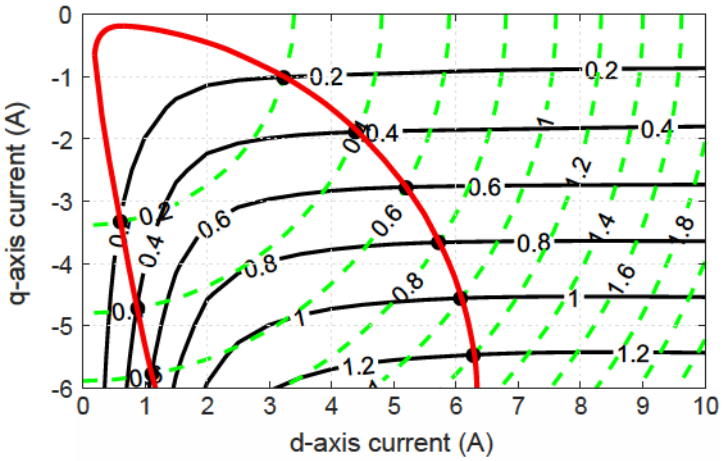

Figure 5.1: Active power (kW) map with $C = 140\ \mu$F and $R_L = 250\ \Omega$ at the speed of 806 rpm. Solid lines represent the electromagnetic power P_{em}. Dashed lines refer to the right part of (5.1). Red bold line highlights the active power balance points.

5.1.1. Active power balance

Since the generator is driven by a prime mover or wind turbine, the active power is achieved through the shaft. Subtracting mechanical and iron losses, the electromagnetic power P_{em} is produced. When the generator is connected to a resistive load, a part of active power is lost as Joule losses in the machine winding (P_J). The remanent is transferred to the load (P_{load}). Therefore, an active power balance is achieved among the electromagnetic power, the Joule losses and the output power:

$$-P_{em} = P_J + P_{load} \tag{5.1}$$

The electromagnetic power of the generator is calculated as:

$$P_{em} = \frac{3}{2}\omega(L_d - L_q)I_d I_q \tag{5.2}$$

The copper Joule losses of the stator winding are easily obtained by I_d and I_q:

$$P_J = \frac{3}{2}(I_d^2 + I_q^2)R_s \tag{5.3}$$

From (4.8), the output power is also computed by I_d and I_q, as:

$$P_{load} = -\frac{3}{2}(V_d I_d + V_q I_q) = \frac{3}{2}(I_d^2 + I_q^2)\frac{R_L X_c^2}{R_L^2 + X_c^2} \tag{5.4}$$

Since all the active powers are represented according to d- and q-axis currents, a current vector plane can be used to identify constant-power contours of the produced electromagnetic power and the consumed power ($P_J + P_{load}$).

As a particular case, Fig. 5.1 shows the constant-active-power contours of a REL generating system with $C = 140\ \mu$F, $R_L = 250\ \Omega$ at the speed of 806 rpm. The

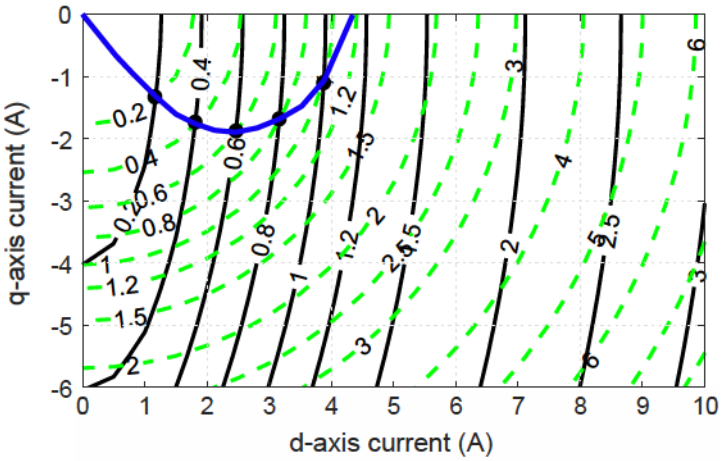

Figure 5.2: Reactive power (kvar) map with $C = 140$ μF and $R_L = 250$ Ω at the speed of 806 rpm. Solid lines represent the generator reactive power Q_{em}. Dashed lines refer to the reactive power provided by the capacitors Q_c. Blue bold line highlights the reactive power balance points.

black solid lines represent P_{em}, while the green dashed lines refer to the right part of (5.1). As mentioned before, the generating system works under a balanced active power condition, which means that it works at the crossing points between the power contours. The active power balance curve is highlighted by the red bold line in Fig. 5.1.

5.1.2. Reactive power balance

In the SERG system, the capacitors are used to provide reactive power. Therefore, the reactive power balance is expressed as:

$$Q_{em} = -Q_c \tag{5.5}$$

where Q_{em} and Q_c are the reactive power of the generator and capacitor, respectively. They are expressed as follows:

$$Q_{em} = \frac{3}{2}\omega(L_d I_d^2 + L_q I_q^2) \tag{5.6}$$

$$Q_c = -\frac{3}{2}(V_q I_d - V_d I_q) = -\frac{3}{2}(I_d^2 + I_q^2)\frac{R_L^2 X_c}{R_L^2 + X_c^2} \tag{5.7}$$

Fig. 5.2 describes the constant-reactive-power contours of the REL generating system mentioned before. The black solid lines represent the generator reactive power Q_{em}, while the green dashed lines represent the reactive power provided by the capacitors. Similar to the active power balance, the crossing points represent the reactive power balance. The resulted reactive power balance curve is denoted by the blue bold line in Fig. 5.2.

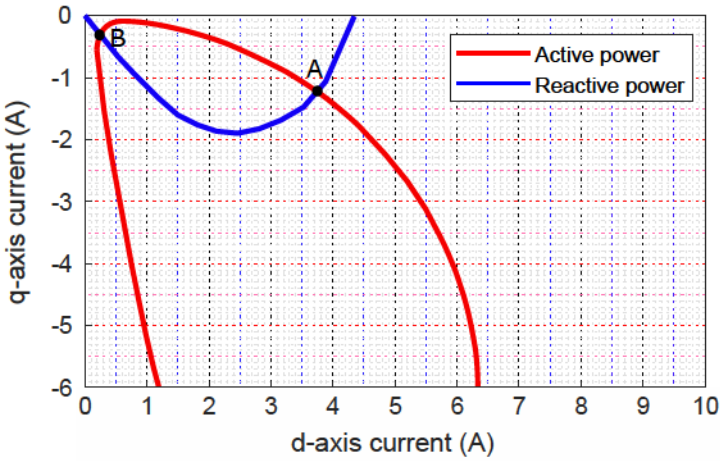

Figure 5.3: Operating points according to active and reactive power balance curves with $C = 140\ \mu$F, $R_L = 250\ \Omega$ at the speed of 806 rpm.

5.1.3. Operating point based on active and reactive power balances

When the generating system is operated at a steady-state condition, both active and reactive power balances have to be satisfied. The active and reactive power balance curves are redrawn in the same current plane, as shown in Fig. 5.3. The crossing points refer to the operating points of the generating system.

Fig. 5.3 shows that two crossing points, which satisfy the total power balances, exist (point A and B). However, only point A is the actual operating point. It is known that the operation of SERG is based on saturation effect, more specifically, the saturation in d-axis inductance. From Fig. 4.3(b), it is observed that if the d-axis current is lower than 1.2 Ampere, no saturation occurs. For point B in Fig. 5.3, the d-axis current is too low to saturate the generator, so the generator cannot work normally, exhibiting low voltage and low power. On the other hand, point A achieves high current, working in the saturation region. Therefore, the generating system has to work on point A once it is self-excited.

With the obtained I_d and I_q of point A, the performance of the generating system can be analyzed by (4.8). It should be noted that the determination of L_d and L_q comes from the interpolation of a function of 2D gridded data (I_d and I_q, as shown in Fig. 5.4), which assures that the cross-saturation effect is again considered in the calculation of the generated voltage. The results in Fig. 5.4 are obtained from 2D FEA simulations.

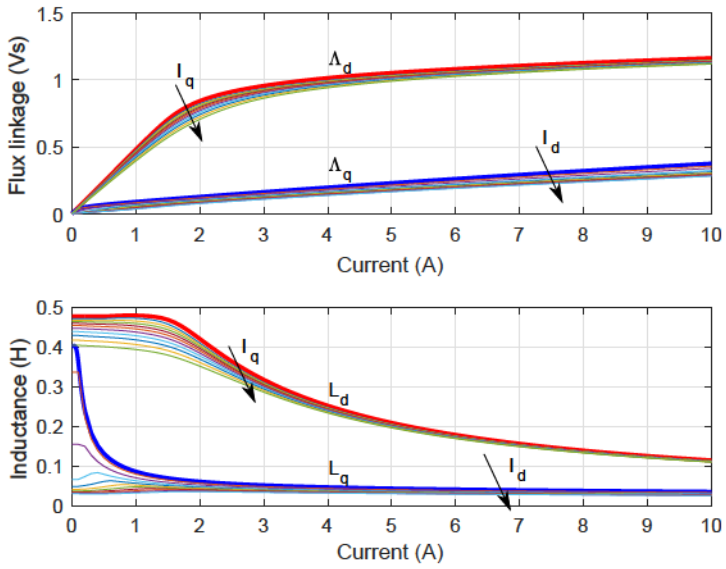

Figure 5.4: d- and q-axis flux linkages and inductances of the REL generator, considering cross-saturation effect.

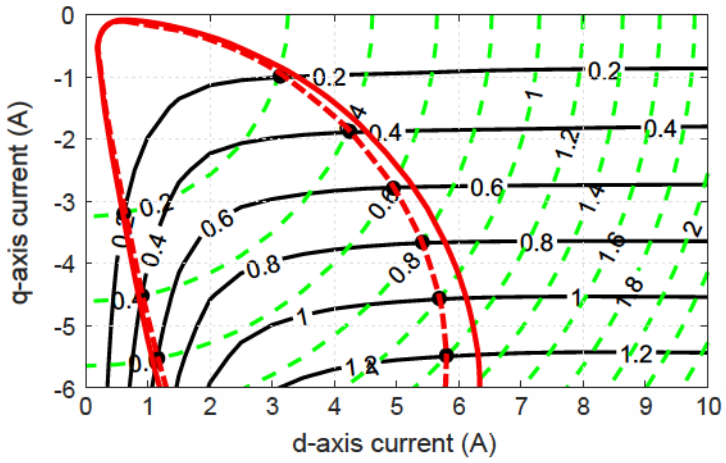

Figure 5.5: Active power (kW) map with $C = 140$ μF, $R_L = 250$ Ω at the speed of 806 rpm (with an additional stator resistance considered).

5.1.4. Impact of stator resistance and inductance on the operating point

It is noticed from (5.3) that the copper losses depends on the stator resistance. If the stator resistance varies, due to temperature rise for example, the active power balance curve changes, as shown in Fig. 5.5. In this case, the stator resistance varies from 4.55 Ω to 5.55 Ω, the active power balance curve changes from the bold solid line to the bold dashed line. From Fig. 5.7, it is seen that the operating point is moved from A to A1. Obviously, the generated voltage will be changed accordingly.

Similarly, the operating point could be different when the d- and q-axis inductances are changed. In Fig. 5.6, an additional inductance (10 mH, almost 20 % of the saturated q-axis inductance) is considered compared to Fig. 5.2. The corresponding reactive power

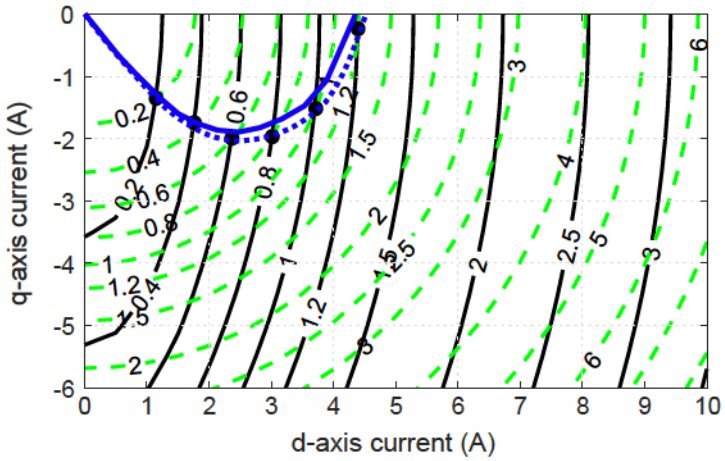

Figure 5.6: Reactive power (kvar) map with $C = 140$ μF, $R_L = 250$ Ω at the speed of 806 rpm (with an additional inductance considered).

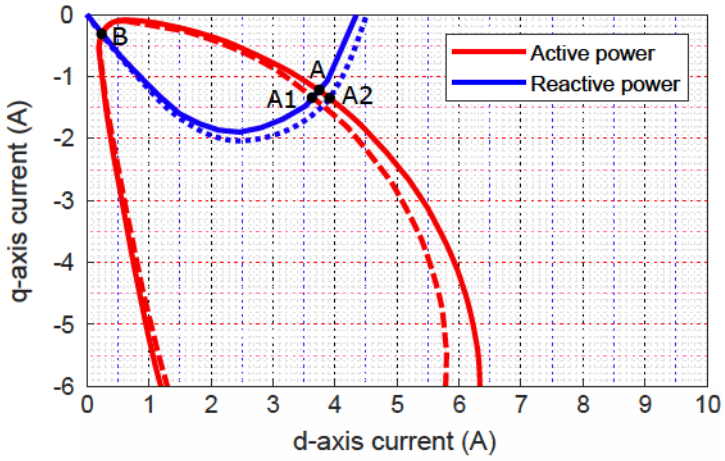

Figure 5.7: Operating points according to active and reactive power balance curves with $C = 140$ μF, $R_L = 250$ Ω at the speed of 806 rpm (with varied stator resistance and inductance).

balance curve is represented by the dashed line. The constant-reactive-power contours of the capacitor keeps the same, while the constant-reactive-power contours of the generator changes. As a consequence, the reactive power balance curve is varied. The operating point changes from point A to point A2 in Fig. 5.7.

Therefore, the accuracy of the stator resistance and inductance are of particular importance to obtain a precise result by using PQ balances.

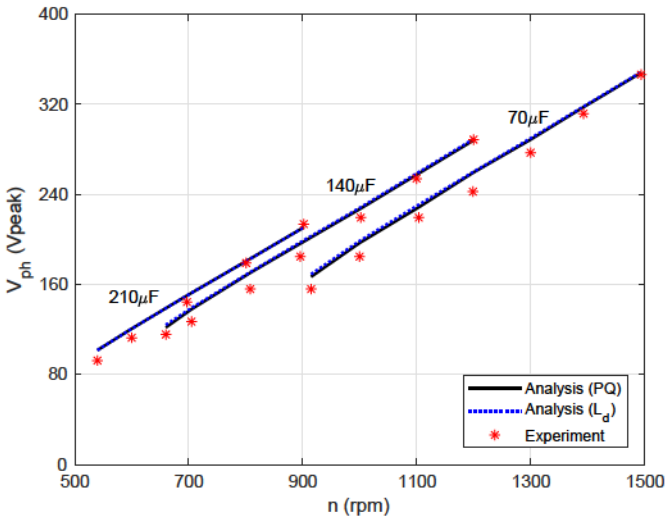

Figure 5.8: The no-load generated voltage against speed for different capacitors (70 μF, 140 μF and 210 μF, respectively).

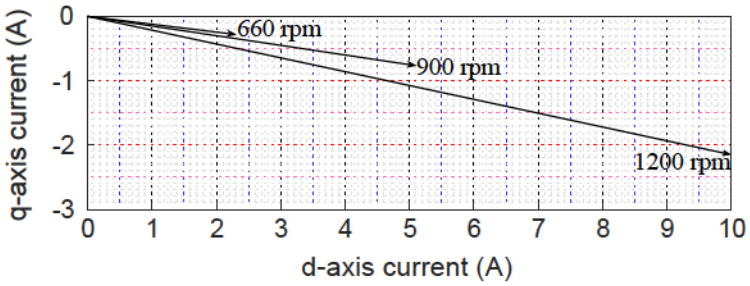

Figure 5.9: Current vectors with $C = 140$ μF at the speed of 660 rpm, 900 rpm and 1200 rpm, respectively.

5.2. Experimental verifications

5.2.1. No-load condition

The no-load condition can be regarded as a special case of the load condition, with infinite resistance connected. Therefore, the same procedure can be carried out to predict the SERG performance by using PQ balances. Fig. 5.8 shows the results of the generated voltage with the capacitance of $C = 70$ μF, 140 μF, and 210 μF, respectively. The results obtained from the PQ balances are shown by the solid lines, while the results from the interpolation of L_d in Chapter 4 are represented by dotted lines. The experimental results are again represented by the stars. It is evidenced that both methods predict very close results to the experiments, and the effect of considering cross-saturation is not significant at no-load conditions.

As the next step, it is helpful to investigate the variation of current vector with speed of the generator, as illustrated in Fig. 5.9. It is noticed that the current vector

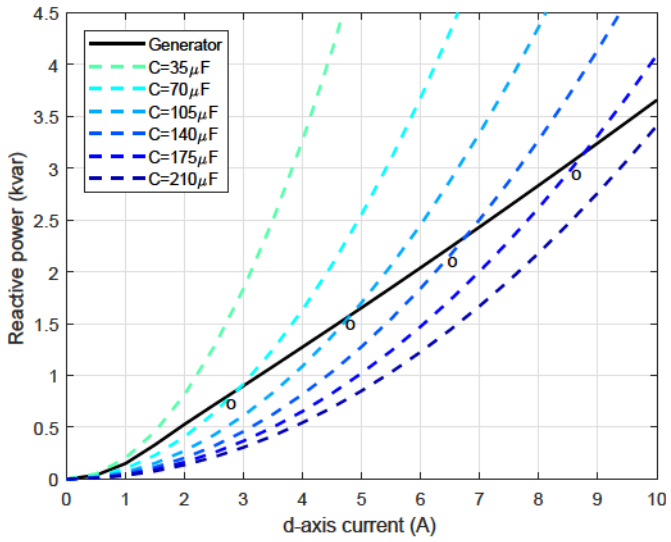

Figure 5.10: The reactive power balance between REL generator and capacitors at 1000 rpm (circles represent the experimental results).

is almost aligned with d-axis when the speed is low. With the increase of speed, the current vector moves toward the q-axis.

Since the stator resistances are quite low, the active power is negligible compared to the reactive power at no-load condition. Furthermore, if the stator resistance is neglected, no active power is generated by the generator, so that the currents vector is forced along the d-axis.

Fig. 5.10 shows the reactive power variation versus current of the REL generating system at 1000 rpm. The solid line represents the reactive power of the generator, while the dashed lines refer to the provided reactive power by the capacitor. Different values of capacitor are considered. The crossing points indicate the reactive balance, that is, the operating points. The experimental results are expressed by circles. It is observed that the analytical results match properly with the experimental results when the current is low. With the increase of current, a slight discrepancy rises. It is also noticed that with the increase of capacitances at same speed, the reactive power required for the operation of the generator increases.

5.2.2. Resistive load condition

As mentioned before, it is convenient to determine the operating point by using PQ balances at load conditions. Comparisons of the voltage versus speed curve with $C = 140\ \mu$F for different loads (250 Ω and 50 Ω) are shown in Fig. 5.11. It is observed that the results obtained from different methods are almost superposed under light-load conditions, while they are away from each other at heavy-load conditions. The results obtained from the PQ balances are more precise, especially at heavy-load conditions. This conclusion is also verified in Fig. 5.12, with $C = 210\ \mu$F, $R_L = 250\ \Omega$ and 50 Ω, respectively. The discrepancy under $R_L = 50\ \Omega$ condition between the new analytical results and experiments mainly attributes to the constant stator resistance used in the active power balance (without considering temperature effect).

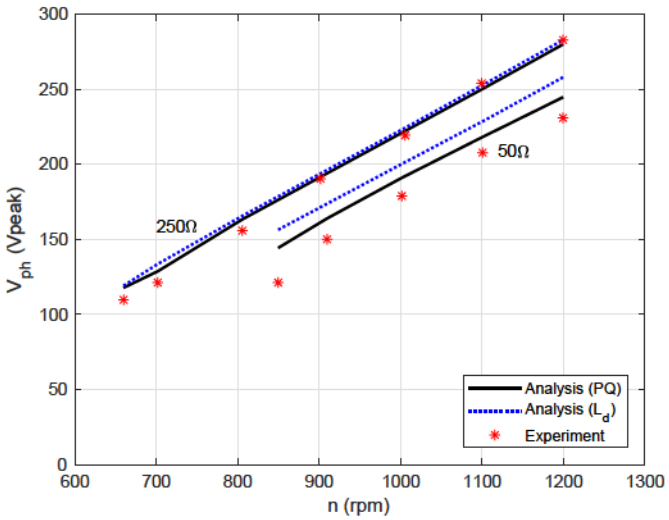

Figure 5.11: The generated voltage against speed with $C = 140$ μF, $R_L = 250$ Ω and 50 Ω, respectively).

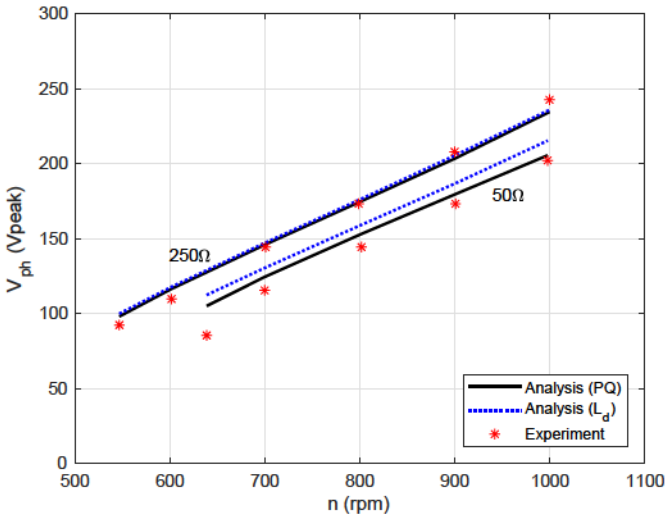

Figure 5.12: The generated voltage against speed with $C = 210$ μF, $R_L = 250$ Ω and 50 Ω, respectively.

It is also noticed from Fig. 5.11 that the output voltage of the REL generator starts from the speed around 850 rpm. If the speed is lower than 850 rpm, the generated voltage collapses. This phenomenon can also be described by the active and reactive power balance curves. Fig. 5.13 shows these curves with $C = 140$ μF, $R_L = 50$ Ω at the speed of 750 rpm and 850 rpm, respectively. The dashed lines represent the PQ balance curves when operated at 750 rpm, while the solid lines are at 850 rpm. Since no crossing point exists between the dashed curves, the generator cannot work in this condition. Similar phenomenon is observed when the load is increased ($R_L = 25$ Ω), as shown in Fig. 5.14. It is shown that increasing the load with resistance below certain critical value, the generated voltage collapses. These PQ balance curves provide a quiet easy way to verify whether the generating system works at certain conditions.

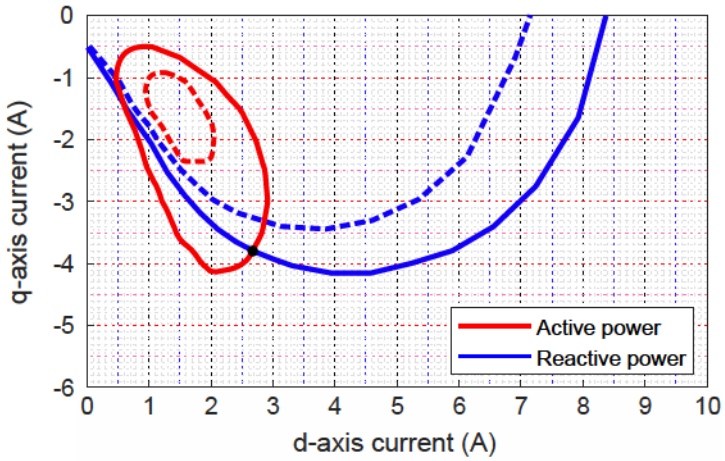

Figure 5.13: Active and reactive power balance curves with $C = 140$ μF, $R_L = 50$ Ω at the speed of 750 rpm and 850 rpm, respectively.

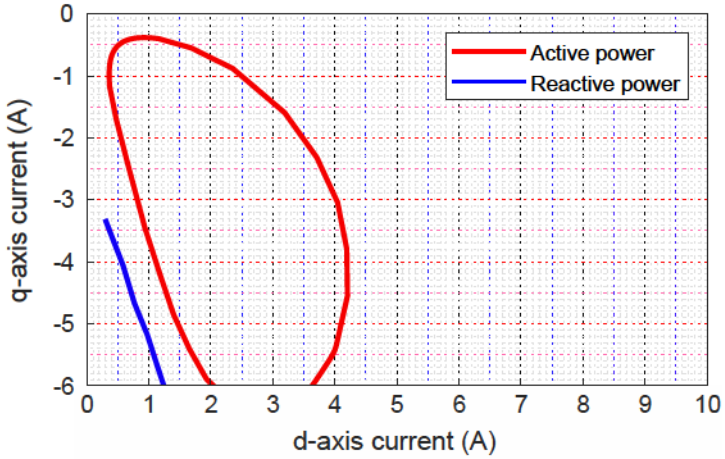

Figure 5.14: Active and reactive power balance curves with $C = 140$ μF, $R_L = 25$ Ω at the speed of 1000 rpm.

Fig. 5.15 shows the current vectors with $C = 140$ μF at the speed of 1000 rpm under no-load, $R_L = 250$ Ω, 150 Ω and 50 Ω conditions, respectively. These current vectors are obtained from active and reactive power balances, and the differences among the power balance curves under different load conditions are significant. It is noticing that the variation of the resistance has effect not only on the active power but also on the reactive power. It is also observed that with the increase of load, the current vector moves towards the q-axis. This is reasonable since, generally speaking, the q-axis current is the "torque current component". In addition, it accounts for the reason that cross-saturation effect should be considered under heavy load conditions.

Table 5.1 shows the load characteristics of SERG with $C = 140$ μF. The left two columns refer to the operating conditions of resistance and speed, the middle three columns are the experimental results, including peak value of line to line voltage ($\hat{V}_{line}$), peak phase current ($\hat{I}_{ph}$) and the shaft torque transmitted from the master motor (T_1).

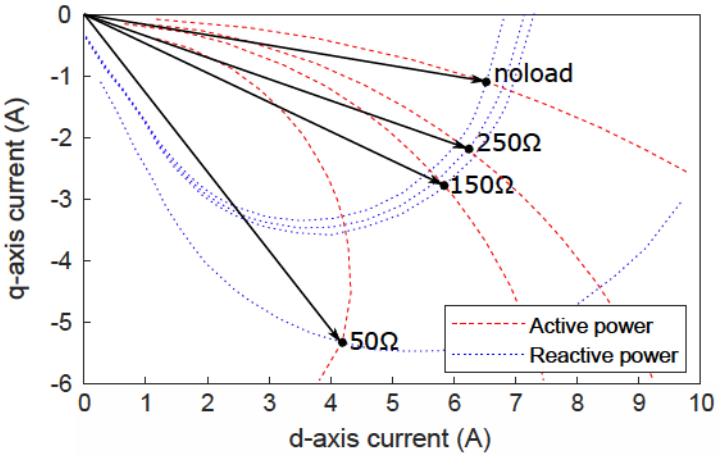

Figure 5.15: Current vectors with $C = 140$ μF at the speed of 1000 rpm at no-load, $R_L = 250$ Ω, 150 Ω and 50 Ω conditions, respectively.

Table 5.1: Load Characteristics of SERG with $C = 140$ μF (Experimental Tests)

R_L (Ω)	n (rpm)	$\hat{V}_{line}$ (V)	$\hat{I}_{ph}$ (A)	T_1 (Nm)	P_{load} (W)	PF –	η %
250	660	190	2.0	1.58	72	0.20	66
250	800	270	3.7	3.19	146	0.17	55
250	1000	380	6.4	6.28	289	0.14	44
150	660	170	1.9	2.05	96	0.33	68
150	800	260	3.7	4.39	225	0.27	61
150	1000	370	6.4	8.00	456	0.22	54
50	850	210	3.8	6.40	441	0.63	77
50	1000	310	6.2	12.30	961	0.56	75
50	1200	400	9.0	19.30	1600	0.49	66

The last three columns show the output power (P_{load}), power factor and efficiency of the generating system (η). It is seen that lower R_L, which means heavier load, leads to lower output voltage when operated at given speed. However, the output power and power factor increase. For constant capacitance and resistance, power factor decreases with the speed going up. These trends can be explained by dividing (5.4) by (5.7), which is:

$$\frac{P_{load}}{Q_c} = \frac{30}{\pi p n R_L C} \tag{5.8}$$

Therefore, the combination of R_L, C and n determines the power factor of the generating system. It is also noticed that the maximum efficiency in Table 5.1 is 77%.

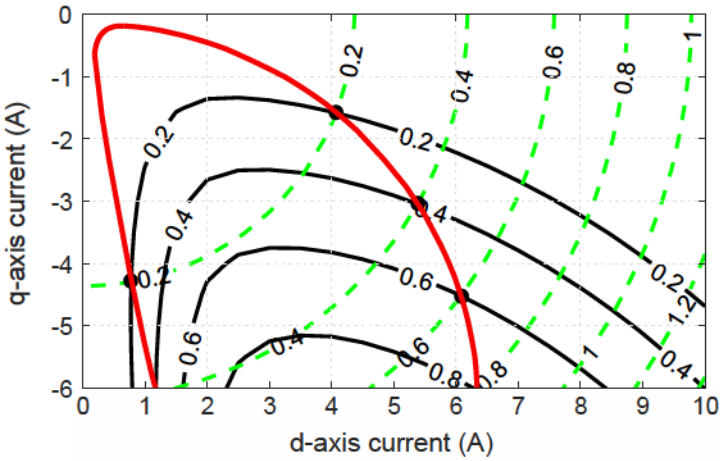

Figure 5.16: Active power (kW) map with $C = 140$ μF and $R_L = 250$ Ω at the speed of 806 rpm. Solid lines represent the generated power $(-P_{em} - P_J)$, while dashed lines refer to P_{load}.

5.3. Voltage regulation with variable capacitances at different speeds

As mentioned in [75], the variable capacitance bank is very useful to keep the generated voltage constant in SERG system. The values of capacitor at different speeds to maintain the generated voltage can be determined by using the PQ balances.

Once the output voltage is given, the output power P_{load} is easily calculated under certain load condition. Equation (5.1) is changed as:

$$P_{load} = -P_{em} - P_J \tag{5.9}$$

Then the new active power map is plotted in Fig. 5.16, where solid lines represent the generated power $(-P_{em} - P_J)$, while dashed lines refer to P_{load}. Since P_{load} is determined, only one dashed line is drawn in the new active power map. Then the operating point is directly obtained by the crossing of the dashed line and solid contour with the same value. After that, the value of capacitor can be calculated by the reactive power balance, which is (5.5).

Thanks to the PQ balances method, some further considerations can be carried out. Fig. 5.17(a) shows how the capacitance varies in order to maintain the generated voltage within the limit of $\hat{V}_{ph} = 202$ V. The load is $R_L = 100$ Ω, and hence the output power is kept $P_{load} = 613$ W. The variation of phase current and electromagnetic power are plotted in Fig. 5.17(b) and Fig. 5.17(c), respectively. The same trend is noticed for C, I_{ph} and P_{em} with the variation of speed. The decrease of phase current with increasing speed indicates reduced Joule losses. Therefore, the efficiency of the system increases with speed, as shown in Fig. 5.17(d).

Combining (1.3) and (4.3), the dynamic model of the SERG system with resistive

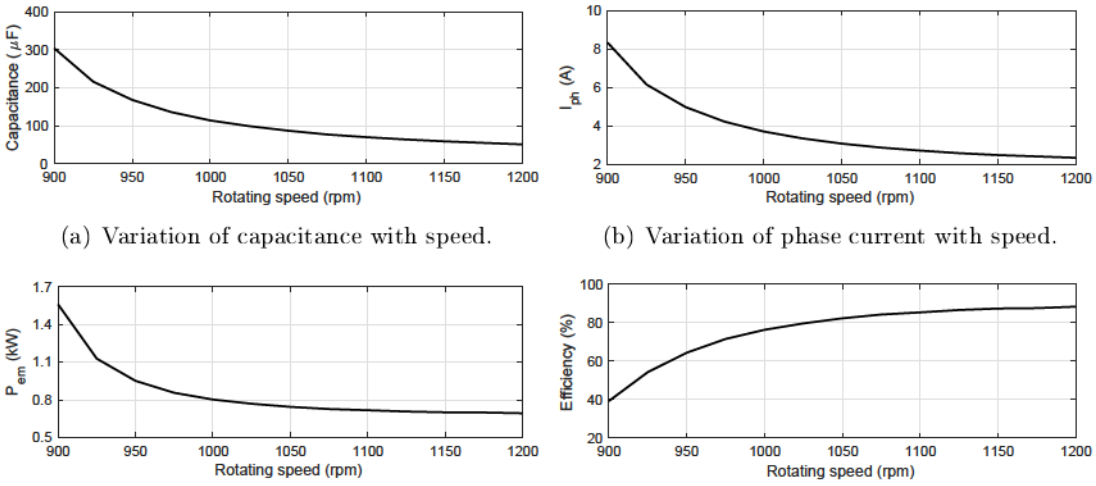

(a) Variation of capacitance with speed.

(b) Variation of phase current with speed.

(c) Variation of electromagnetic power with speed.

(d) Variation of efficiency with speed.

Figure 5.17: Variation of capacitance, phase current, electromagnetic power and efficiency with speed under constant generated voltage.

load can be written as:

$$\begin{cases} \dfrac{di_d}{dt} = -\dfrac{R_s}{L_d} i_d + \omega \dfrac{L_q}{L_d} i_q + \dfrac{1}{L_d} v_d \\ \dfrac{di_q}{dt} = -\omega \dfrac{L_d}{L_q} i_d - \dfrac{R_s}{L_q} i_q + \dfrac{1}{L_q} v_q - \dfrac{\omega \Lambda_{res}}{L_q} \\ \dfrac{dv_d}{dt} = -\dfrac{1}{C} i_d - \dfrac{1}{R_L C} v_d + \omega v_q \\ \dfrac{dv_q}{dt} = -\dfrac{1}{C} i_q - \omega v_d - \dfrac{1}{R_L C} v_q \end{cases} \tag{5.10}$$

These equations are then expressed in a compact matrix form, as

$$\dot{\mathbf{x}} = \mathbf{A}\mathbf{x}(t) + \mathbf{B} \tag{5.11}$$

where

$$\mathbf{x} = [i_d, i_q, v_d, v_q]^T,$$

$$A = \begin{bmatrix} -\frac{R_s}{L_d} & \omega \frac{L_q}{L_d} & \frac{1}{L_d} & 0 \\ -\omega \frac{L_d}{L_q} & -\frac{R_s}{L_q} & 0 & \frac{1}{L_q} \\ -\frac{1}{C} & 0 & -\frac{1}{R_L C} & \omega \\ 0 & -\frac{1}{C} & -\omega & -\frac{1}{R_L C} \end{bmatrix},$$

$$B = \begin{bmatrix} 0 \\ -\frac{\omega \Lambda_{res}}{L_q} \\ 0 \\ 0 \end{bmatrix}.$$

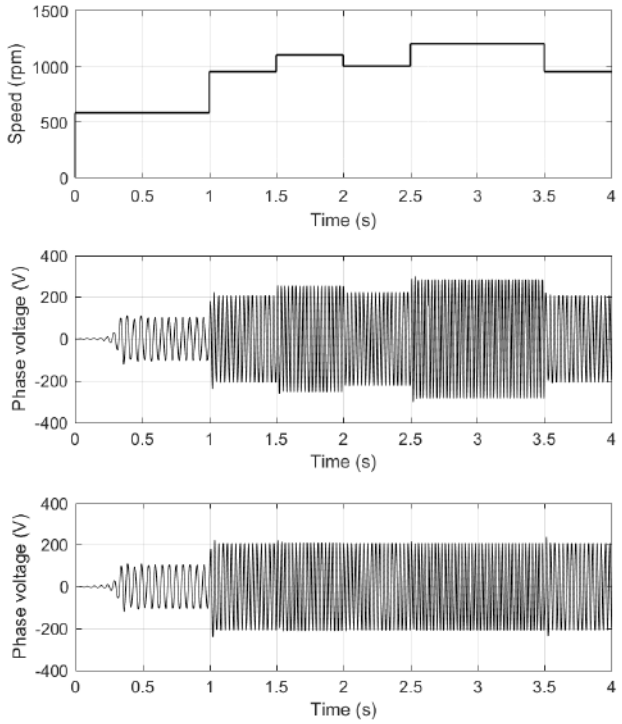

Figure 5.18: Variation of generated voltage without and with changed capacitors.

Using the backward Euler formula to discretize the model, (5.11) becomes as follows:

$$\mathbf{x}_{t+1} = \mathbf{x}_t + T_c\mathbf{A}\mathbf{x}_t + T_c\mathbf{B} = (\mathbb{1} + T_c\mathbf{A})\mathbf{x}_t + T_c\mathbf{B} \tag{5.12}$$

where T_c denotes the sampling time.

With this discrete-time model, the performance of SERG system can be simulated. It should be mentioned that L_d and L_q at each current are interpolated from the simulated d- and q-axis magnetizing curves, as shown in Fig. 5.4.

The effectiveness of the variable capacitance in maintaining constant the output voltage at different speeds is verified by this transient simulation. The results are shown in Fig. 5.18. The SERG is connected with $C = 168$ μF operated at the speed of 580 rpm for self-excitation. At $t = 1$ s, the load is connected and speed is increased to 950 rpm. After that, the operating speed is changed step by step (1100 rpm at 1.5 s, 1000 rpm at 2.0 s, 1200 rpm at 2.5 s and 950 rpm at 3.5 s), as displayed in the first figure of Fig. 5.18. The voltage variation with constant capacitor is shown in the second figure. On the contrary, the voltage variation with variable capacitors (after $t = 1$ s) is plotted in the third figure. A constant generated voltage is demonstrated in spite of the varying speeds.

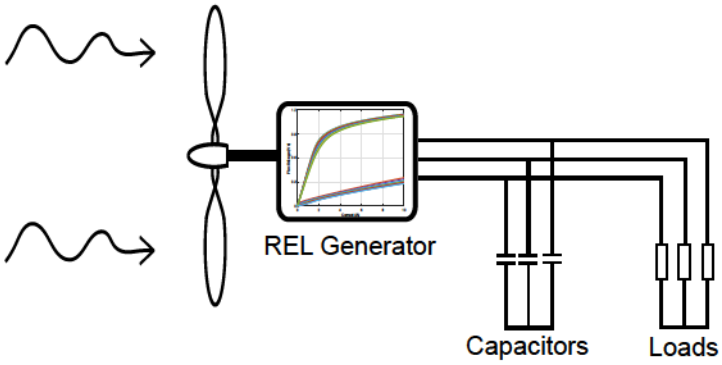

Figure 5.19: Scheme of the SERG system with wind turbine.

5.4. Optimal C and R_L to achieve the maximum power utilization

Taking advantage of the PQ balances, analysis of the capacitance and load resistance are carried out when SERG is joint with wind turbine. The scheme of wind system with SERG is shown in Fig. 5.19. The objective of this analysis is to find the "optimal capacitor and resistor combination" that achieving the maximum utilization of the mechanical power produced by wind turbine.

5.4.1. Wind turbine characteristics

The power producing capability (P_m) of a practical wind turbine has been previously developed [76], which is

$$P_m = \frac{1}{2} C_p \rho S v_{wind}^3 \tag{5.13}$$

where C_p is a "coefficient of power" depending on the type of wind turbine, ρ is the air density in kg/m^3, S is the cross–section area of the turbine in m^2, and v_{wind} is the wind speed in m/s.

As far as horizontal-axis turbine is concerned, the coefficient C_p is calculated based on the tip speed ratio λ and the pitch angle β [77]:

$$C_p(\lambda, \beta) = c_1(c_2\lambda_i^{-1} - c_3\beta - c_4)e^{-c_5\lambda_i^{-1}} + c_6\lambda \tag{5.14}$$

where

$$\lambda_i^{-1} = (\lambda + 0.08\beta)^{-1} + 0.035(\beta^3 + 1)^{-1} \tag{5.15}$$

the tip speed ratio is given by

$$\lambda = R_t \frac{\omega_m}{v_{wind}} \tag{5.16}$$

where R_t is the turbine radius, ω_m is the turbine angular speed.

Referring to (5.13), the peak power of the turbine at a given wind speed occurs where C_p is maximum. According to Betz's Law, the maximum wind power coefficient results in 0.593. The relationship between the output power and turbine speed for various wind speeds is described in Fig. 5.20. As the variation of turbine speed at a given wind speed, there exists an optimal turbine speed that produces the maximum output power. This

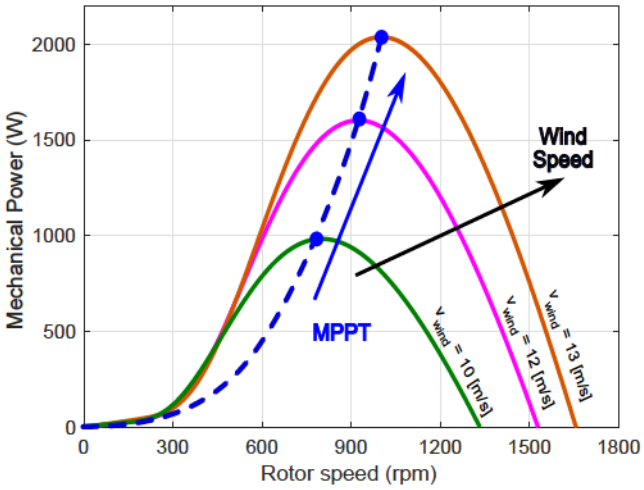

Figure 5.20: Turbine output power versus speed for various wind speeds.

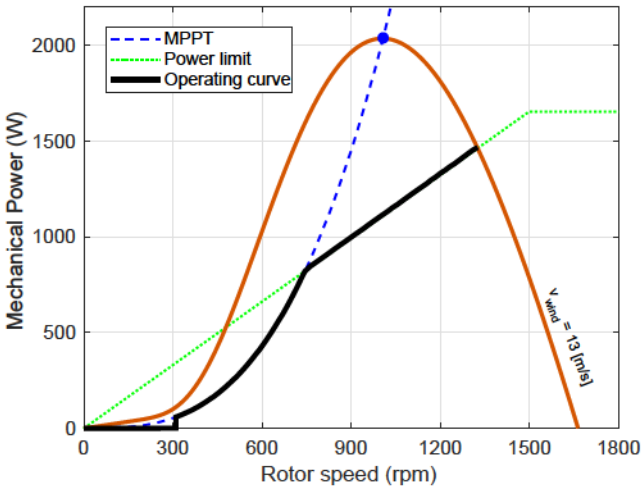

Figure 5.21: Determination of mechanical power characteristic in wind system (cut-in and cut-off wind speed of the turbine are 4 m/s and **13** m/s, respectively).

optimal turbine speed changes with wind speed. These optimal turbine speed points at each wind speed form the maximum power point tracking (MPPT) curve, highlighted by the dashed line in Fig. 5.20.

The REL generator used here is the same as the one in Chapter 4, with the main parameters shown in Table 4.1. To maximize the power utilization, it is desirable for the generator to follow MPPT trajectory. Meanwhile, the transferred power at each speed should be limited by the generator power capability, which is due to thermal limitation of the generator. Therefore, the power characteristic of the whole system is determined by the lower power limitation at each speed, as shown in Fig. 5.21. The power follows MPPT at low speed, while at high speed it is limited by generator maximum power.

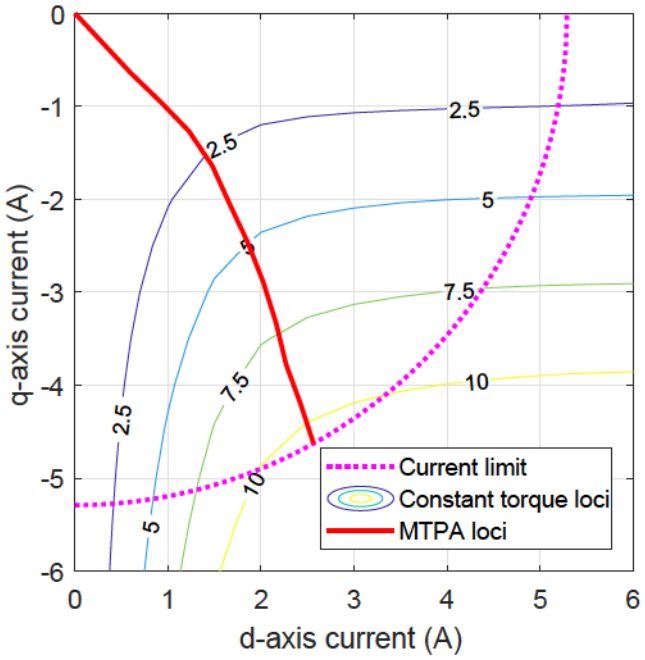

Figure 5.22: Performance map of the REL generator.

5.4.2. Methods to determine the "optimal C and R_L combination"

From the mechanical power characteristic curve in Fig. 5.21, constant power and torque are determined at given rotor speed. Considering the active power balance in (5.9), the achievable maximum output power is the value when Joule loss is minimum. This means the minimum phase current at given torque, *i.e.*, the maximum torque per current (MTPA). The operating point of the SERG system follows MTPA trajectory, plotted by the red solid line in Fig. 5.22, to achieve the maximum output power. Consequently, the operating point at given speed is exactly the crossing point of MTPA curve and constant torque locus. After that, the optimal load resistance and capacitance can be calculated from PQ balances, respectively.

The variation of "optimal capacitor and resistor combination" at different speed is shown in Fig. 5.23(a), while the corresponding efficiency and power factor are figured in Fig. 5.23(b). The results show that the optimal capacitor varies significantly with the speed. On the contrary, the optimal resistance varies slightly. If the resistor and capacitor are properly selected, the SERG system is capable of transmitting the power with an efficiency over 80 %, as verified in Fig. 5.23(b).

For instance, one "optimal capacitor and resistor combination" (109 μF and 46 Ω) at the speed of 1000 rpm is selected for simulation. The generated voltage behavior is plotted in Fig. 5.24. The system is self-excited at 740 rpm with only capacitors connected. At $t = 1$ s, the operating speed is increased up to 1000 rpm, and then the load $R_L = 46\ \Omega$ is connected at $t = 2$ s. The phase voltage is 168.5 V_{peak}, with an output power of 926 W. Since the acquired mechanical power is 1105 W at the speed of 1000 rpm, the system achieves a conversion efficiency of 83.8 %.

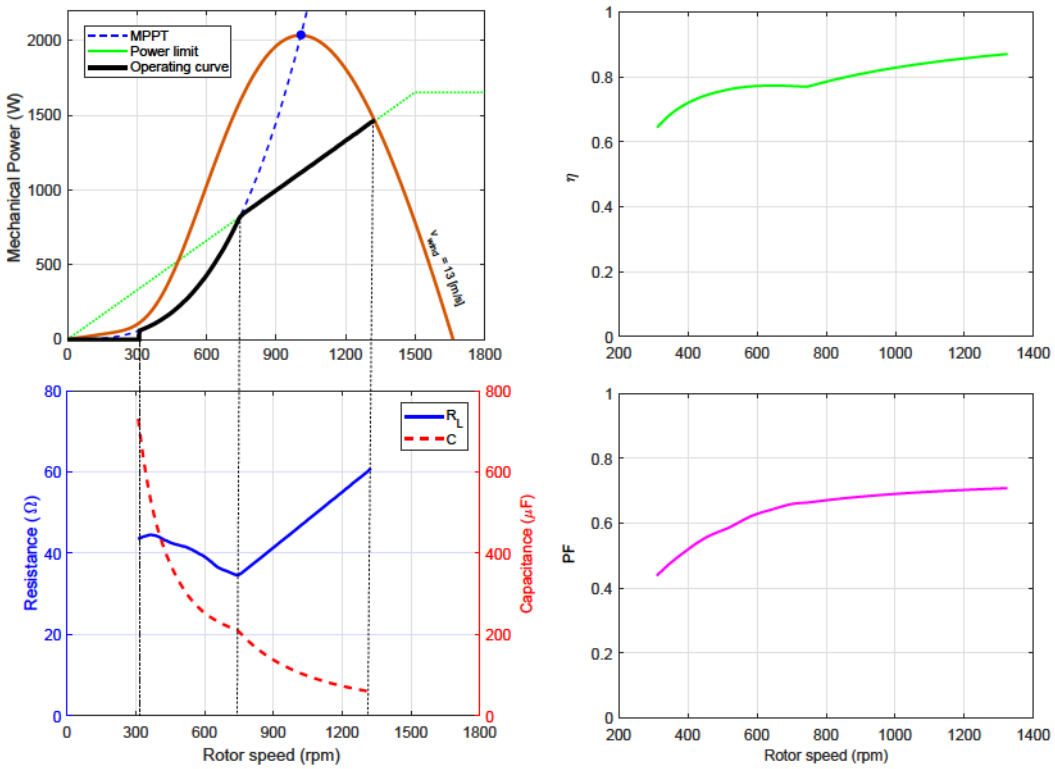

(a) Optimal C and R_L versus speed.

(b) Efficiency and power factor versus speed.

Figure 5.23: Variations of optimal resistance and capacitance, efficiency and power factor at different rotor speeds.

5.4.3. Experimental verifications

By using the test bench shown in Fig. 4.1, some experiments are carried out to verify the calculated "optimal capacitor and resistor combination". Since the available resistance and capacitance in the laboratory are **50 Ω** and **35 μF**, respectively, the experiments are designed with different combinations of these resistors and capacitors.

Table 5.2 shows the experimental results of SERG at the speed around **1000** rpm. The left three columns refer to the operating conditions (rotating speed n, connected C and R_L). The middle two columns are the measured results, including peak phase voltage ($\hat{V}_{ph}$) and peak phase current ($\hat{I}_{ph}$). The last three columns show the calculated output power (P_{load}), copper Joule losses (P_J, neglecting temperature rise) and energy conversion efficiency (η).

During the experiment, the minimum speed to generate high voltage with $C = 105$ μF and $R_L = 50$ Ω is **1043** rpm, below which the voltage collapses. The top five rows in Table 5.2 refer to the condition with the same capacitor but different load resistors. The generated voltage is slightly reduced with partial load, while a significant reduction is noticed when $R_L = 50$ Ω. This is probably attributed to the high cross-saturation effect between d- and q-axis inductances. The SERG system is preferable to work with heavy-load in terms of efficiency. However, the generated voltage collapses

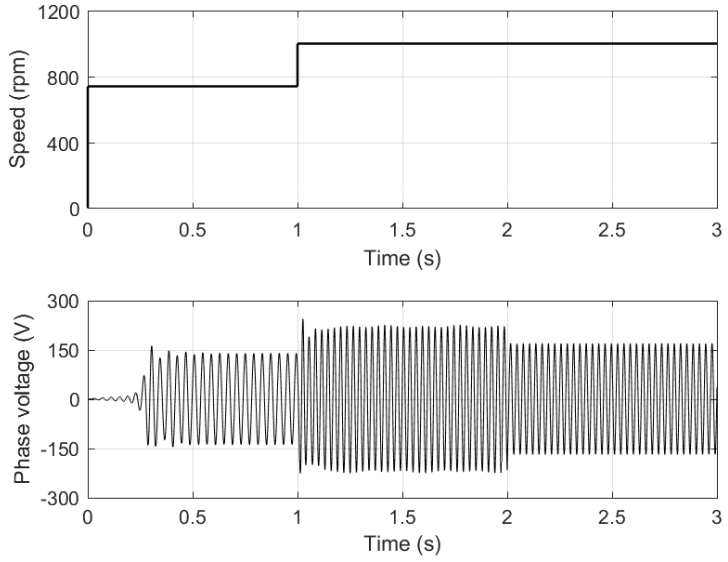

Figure 5.24: Simulated output voltage behavior of SERG with $C = 109\ \mu F$.

Table 5.2: Experimental Load Characteristics of SERG at the Speed around 1000 rpm.

n (rpm)	C (μF)	R_L (Ω)	$\hat{V}_{ph}$ (V)	$\hat{I}_{ph}$ (A)	P_{load} (W)	P_J (W)	η %
1000	105	250	208	4.6	259	144	64.3
1005	105	200	208	4.6	324	144	69.2
1004	105	150	202	4.6	408	144	73.9
1002	105	100	191	4.6	545	144	79.1
1043	105	50	144	4.2	625	120	83.9
1002	140	50	179	6.2	961	262	78.6
1006	175	50	196	8.0	1156	437	72.6
1000	210	50	202	9.0	1225	553	68.9

when $R_L = 25\ \Omega$ is connected even at 1200 rpm. The last three rows consider the condition with the same load resistor but different capacitors. Although the generated voltage and output power increase with the capacitance, the conversion efficiency is decreasing. Overall, the "optimal capacitor and resistor combination" to achieve the highest energy conversion efficiency are 105 μF and 50 Ω, which are quite close to the predictions in the last subsection (109 μF and 46 Ω, respectively).

5.5. Conclusion

This Chapter proposes the method of PQ balances to describe the SERG performance, considering the cross-saturation effect. Comparing to the method in the last Chapter, the predicted results are more precise especially under heavy-load conditions. Besides, it is possible to verify whether the generating system works at certain conditions by using the PQ balance curves. This is quite useful for heavy-load conditions of the REL generator.

With the help of PQ balances, the values of capacitor to maintain constant generated voltage at different speeds are determined. The capacitance decreases with the increasing speed, while the system efficiency improves. In addition, the prediction of "optimal capacitor and resistor combination" to achieve the highest energy conversion efficiency is addressed by the mechanical power characteristic and PQ balances. It is demonstrated that the SERG system is capable of transmitting the power with an efficiency around 80 %.

With all these characteristics presented above, the SERG exhibits an effective and low-cost solution for wind applications, especially in remote and low power systems.

Conclusions

In this work, the design and analysis of high performance REL machines have been developed and discussed. Furthermore, two particular applications have been investigated: REL motors for EV applications and SERG for isolated wind applications. Hereafter, the main conclusions of the work are reported.

To start with, the transversely-laminated anisotropy rotor type with multiple flux-barriers is chosen to be designed and analyzed, which is found to achieve relatively high saliency ratio, low rotor loss and low torque ripple. More specifically, a detailed parametric analysis of the rotor geometry has been carried out, suggesting an automatic drawing and simulation procedure. The Joukowski airfoil potential formulation and conformal mapping technique are used to describe the streamlined flux-barrier. The width of each iron part is computed according to the flux density distribution of the d-axis flux, while the width of each flux-barrier is designed according to the magnetic voltage drop across the corresponding flux-barrier. The circular arc is used to replace the parabolic line for the barrier end, so as to avoid the stress concentration points. Some tricks are also suggested in order to overcome some geometric issues.

By using the automatic design procedure, it is very fast to investigate the impact of some rotor parameters on the machine performance. The barrier end angle is noticed to have a significant effect on torque ripple, while the average torque is related to the number of flux-barriers. It is recommended to have three or four barrier layers per pole in practical design. From the point of view of torque, there is not an actual benefit in increasing the flux-barrier width. The insulation ratio is suggested to be chosen according to the stator slot width to slot pitch ratio. The inset PM contributes to the average torque, power factor and flux-weakening capability of the REL machine, while the risk of PM demagnetization should be carefully considered in design. The PMs in the most external barrier are noticed to be the most stressed. These results provide a practical guideline for the REL machine design.

The design of REL motors for EV applications is based on the dimension of the commercial Lexus LS 600h motor. The preliminary design is carried out keeping the same stator, while the rotor is replaced by a REL one. The rotor is optimized by using DE algorithm, with the objectives of high average torque and low torque ripple. The three-barrier motor is found to have similar performance with the four-barrier motor. After that, the stator is redesigned, and the optimization procedure is carried out in terms of split ratio, slot-pole combination and rotor optimization. An analytical

calculation of slot area is innovatively derived, in order to optimize the split ratio and slot-pole combination under the assumption of constant copper loss. The 54-slot 3-pole-pair combination is selected, and the optimal split ratio is 0.6.

The comparison between the REL and IPM motors shows that the REL motor achieves the characteristics of significant cost saving (30 % of IPM), excellent efficiency (maximum 94 %), low torque ripple (4.1 %) and considerable power density (73 % of IPM). Despite of the low power factor, the REL motor has the potential to operate at very high temperature, due to the absence of PMs and negligible rotor losses. In addition, it is capable of operating at high speed, with reduced power but high efficiency. Overall, the REL machine can be used for electric mobilities, especially for low-cost light-weight vehicle applications. The ferrite magnets can be inset into the rotor flux-barriers to improve the REL motor performance, making it a potential competitor with the IPM machine for EV applications.

Regarding to SERG, the performance predictions under steady-state conditions are firstly investigated. It is mainly based on two methods, which are interpolation of L_d (only a function of I_d) and PQ balances. In the latter method, the cross-saturation effect is considered. At no-load condition, both methods achieve almost the same results. Under resistive load condition, on the contrary, the predicted voltage are slightly different within the two methods. The results obtained from PQ balances are closer to the experimental results, and the significance of considering cross-saturation effect is obvious at heavy-load conditions. It is also verified that the generated voltage goes up significantly with increasing speed or capacitor, while decreases with increasing load.

The conditions related to successful self-excitation in SERG, such as required capacitance, rotor residual magnetism, rotor acceleration and pre-charging capacitors, are investigated. An appropriate capacitance is essential not only for self-excitation, but also for providing reactive power to the REL generator. It is also advisable to have a sufficient rotor residual magnetism and a low rotor acceleration in order to achieve a stable initial self-excitation process in the REL generator. Besides, the pre-charging capacitors provide a way to make the REL generator self-excite even with no rotor residual magnetism. Alternatively, the unstable self-excitation process of REL generator can be overcome by introducing PMs in the rotor flux-barriers, which is named self-excited PMAREL generator. Performance characteristics of the self-excited PMAREL generator are also investigated. The analysis of some design parameters provides guidelines for a proper design of the PMAREL generator. The main idea is to increase L_d as much as possible, instead of increasing $(L_d - L_q)$ for a PMAREL motor design. In addition, the self-excited PMAREL generator exhibits the improvement in terminal voltage, output power and power factor comparing to SERG.

The PQ balances also help to verify feasible operating conditions, determine capacitances for voltage regulation at different speeds, and calculate "optimal capacitor and resistor combination". Although capacitors are necessary for self-excitation, the SERG system is quite cheap and requires no power electronics. It is also capable of providing quite high power with an efficiency over 80 %. All the results are helpful for applications where SERG is used as stand-alone generators, especially in remote and low power systems.

In conclusion, the following most important contributions can be stated from this doctoral study:

- provide in details the drawing steps required for high performance REL design, suggesting an automatic modeling and simulating procedure,
- analyze the impact of some rotor parameters on the machine performance, providing a practical guideline for the REL or PMAREL machine design,
- develop an analytical calculation for the split ratio optimization,
- carry out a performance comparison between the optimized REL motor and the commercial product, highlighting the merits and defects of the REL motor for EV applications,
- propose two methods to predict the operating points of SERG, and verify with experiments under various operating conditions,
- investigate different conditions for initial self-excitation in SERG, including required capacitance, rotor residual magnetism, rotor acceleration and pre-charging capacitors,
- study the effect of some design parameters, providing guidelines for a proper design of PMAREL generator,
- investigate the PM assisting on the performance improvement of SERG,
- verify feasible operating conditions, determine capacitance for voltage regulation, and calculate the "optimal capacitor and resistor combination" of the SERG system.

Future prospects

Hereafter there are some suggestions for the future research:

- For the REL or PMAREL motor, the mechanical analysis of rotor structure is required, and the prototype validation is also considered in the near future.
- The future work of SERG may focus on the system installation, combined with a wind turbine. Another interesting work is to compare the performance of SERG with SEIG under the same power rating.

Bibliography

[1] J. K. Kostko, "Polyphase reaction synchronous motors," *Journal of the American Institute of Electrical Engineers*, vol. 42, no. 11, pp. 1162–1168, Nov. 1923.

[2] A. J. O. Cruickshank, R. W. Menzies, and A. F. Anderson, "Axially laminated anisotropic rotors for reluctance motors," *Electrical Engineers, Proceedings of the Institution of*, vol. 113, no. 12, pp. 2058–2060, Dec. 1966.

[3] A. Fratta, A. Vagati, and F. Villata, "On the evolution of AC machines for spindle drive applications," *IEEE Transactions on Industry Applications*, vol. 28, no. 5, pp. 1081–1086, Sept. 1992.

[4] D. A. Staton, T. J. E. Miller, and S. E. Wood, "Maximising the saliency ratio of the synchronous reluctance motor," *IEE Proceedings B - Electric Power Applications*, vol. 140, no. 4, pp. 249–259, Jul. 1993.

[5] W. L. Soong, D. A. Staton, and T. J. E. Miller, "Validation of lumped-circuit and finite-element modelling of axially-laminated brushless motors," in *1993 Sixth International Conference on Electrical Machines and Drives*, Sept. 1993, pp. 85–90.

[6] T. Matsuo and T. A. Lipo, "Rotor design optimization of synchronous reluctance machine," *IEEE Transactions on Energy Conversion*, vol. 9, no. 2, pp. 359–365, Jun. 1994.

[7] P. J. Lawrenson and S. K. Gupta, "Developments in the performance and theory of segmental-rotor reluctance motors," *Proceedings of the Institution of Electrical Engineers*, vol. 114, no. 5, pp. 645–653, May 1967.

[8] I. Marongiu and A. Vagati, "Improved modelling of a distributed anisotropy synchronous reluctance machine," in *Conference Record of the 1991 IEEE Industry Applications Society Annual Meeting*, Sept. 1991, pp. 238–243.

[9] T. J. E. Miller, A. Hutton, C. Cossar, and D. A. Staton, "Design of a synchronous reluctance motor drive," *IEEE Transactions on Industry Applications*, vol. 27, no. 4, pp. 741–749, Jul. 1991.

[10] J. J. Germishuizen, F. S. V. der Merwe, K. V. der Westhuizen, and M. J. Kamper, "Performance comparison of reluctance synchronous and induction traction drives

for electrical multiple units," in *Conference Record of the 2000 IEEE Industry Applications Conference*, vol. 1, Oct. 2000, pp. 316–323.

[11] S. Morimoto, M. Sanada, and Y. Takeda, "Performance of PM-assisted synchronous reluctance motor for high-efficiency and wide constant-power operation," *IEEE Transactions on Industry Applications*, vol. 37, no. 5, pp. 1234–1240, Sept. 2001.

[12] T. A. Lipo, "Synchronous reluctance machines-a viable alternative for AC drives?" *Electric Machines and Power Systems*, vol. 19, pp. 659–671, 1991.

[13] A. Vagati, "The synchronous reluctance solution: a new alternative in AC drives," in *Proceedings of IECON 1994 - 20th Annual Conference of IEEE Industrial Electronics*, vol. 1, Sept. 1994, pp. 1–13.

[14] M. J. Kamper, F. S. V. der Merwe, and S. Williamson, "Direct finite element design optimisation of the cageless reluctance synchronous machine," *IEEE Transactions on Energy Conversion*, vol. 11, no. 3, pp. 547–555, Sept. 1996.

[15] A. Vagati, G. Franceschini, I. Marongiu, and G. Troglia, "Design criteria of high performance synchronous reluctance motors," in *Conference Record of the 1992 IEEE Industry Applications Society Annual Meeting*, Oct. 1992, pp. 66–73.

[16] M. J. Kamper and A. F. Volsdhenk, "Effect of rotor dimensions and cross magnetisation on L_d and L_q inductances of reluctance synchronous machine with cageless flux barrier rotor," *IEE Proceedings - Electric Power Applications*, vol. 141, no. 4, pp. 213–220, Jul. 1994.

[17] A. Fratta, G. P. Troglia, A. Vagati, and F. Villata, "Evaluation of torque ripple in high performance synchronous reluctance machines," in *Conference Record of the 1993 IEEE Industry Applications Conference Twenty-Eighth IAS Annual Meeting*, Oct. 1993, pp. 163–170.

[18] A. Vagati, M. Pastorelli, G. Francheschini, and S. C. Petrache, "Design of low-torque-ripple synchronous reluctance motors," *IEEE Transactions on Industry Applications*, vol. 34, no. 4, pp. 758–765, Jul. 1998.

[19] M. Nashiki, A. Satake, Y. Kawai, T. Yokochi, and S. Okuma, "Torque ripple reduction of reluctance motor with slit rotor," *IEEJ Transactions on Industry Applications*, vol. 117, no. 8, pp. 1008–1014, 1997.

[20] M. Sanada, K. Hiramoto, S. Morimoto, and Y. Takeda, "Torque ripple improvement for synchronous reluctance motor using an asymmetric flux barrier arrangement," *IEEE Transactions on Industry Applications*, vol. 40, no. 4, pp. 1076–1082, Jul. 2004.

[21] G. Pellegrino, T. M. Jahns, N. Bianchi, W. L. Song, and F. Cupertino, *The rediscovery of synchronous reluctance and ferrite permanent magnet motors.* Tutorial Course Notes, New York, NY, USA: Springer, 2016.

[22] A. Vagati, A. Canova, M. Chiampi, M. Pastorelli, and M. Repetto, "Design refinement of synchronous reluctance motors through finite-element analysis," *IEEE Transactions on Industry Applications*, vol. 36, no. 4, pp. 1094–1102, Jul. 2000.

[23] N. Bianchi and T. M. Jahns, *Design, analysis, and control of interior PM synchronous machines.* IEEE Industry Applications Society Annual Meeting, Seattle, CLEUP, 2004.

[24] N. Bianchi, E. Fornasiero, M. Ferrari, and M. Castiello, "Experimental comparison of PM-assisted synchronous reluctance motors," *IEEE Transactions on Industry Applications*, vol. 52, no. 1, pp. 163–171, Jan. 2016.

[25] C. T. K.J. Binns, P.J. Lawrenson, *The analytical and numerical solution of electric and magnetic fields.* John Wiley and Sons copyright 1992, 1992.

[26] R. R. Moghaddam, "Synchronous reluctance machine (SynRM) in variable speed drives (VSD) applications," Ph.D. dissertation, KTH, Electrical Machines and Power Electronics, 2011.

[27] M. D. Nardo, M. Degano, M. Galea, C. Gerada, M. Palmieri, F. Cupertino, N. Bianchi, and D. Gerada, "End barrier shape optimizations and sensitivity analysis of synchrnous reluctance machines," in *IECON 2015 - 41st Annual Conference of the IEEE Industrial Electronics Society*, Nov. 2015, pp. 2914–2919.

[28] P. Guglielmi, B. Boazzo, E. Armando, G. Pellegrino, and A. Vagati, "Permanent-magnet minimization in PM-assisted synchronous reluctance motors for wide speed range," *IEEE Transactions on Industry Applications*, vol. 49, no. 1, pp. 31–41, Jan 2013.

[29] M. Ferrari, N. Bianchi, A. Doria, and E. Fornasiero, "Design of synchronous reluctance motor for hybrid electric vehicles," *IEEE Transactions on Industry Applications*, vol. 51, no. 4, pp. 3030–3040, July 2015.

[30] M. Ferrari, N. Bianchi, and E. Fornasiero, "Analysis of rotor saturation in synchronous reluctance and PM-assisted reluctance motors," *IEEE Transactions on Industry Applications*, vol. 51, no. 1, pp. 169–177, Jan. 2015.

[31] N. Bianchi, H. Mahmoud, and S. Bolognani, "Fast synthesis of permanent magnet assisted synchronous reluctance motors," *IET Electric Power Applications*, vol. 10, no. 5, pp. 312–318, 2016.

[32] N. Bianchi, S. Bolognani, E. Carraro, M. Castiello, and E. Fornasiero, "Electric vehicle traction based on synchronous reluctance motors," *IEEE Transactions on Industry Applications*, vol. 52, no. 6, pp. 4762–4769, Nov. 2016.

[33] K. Chau, C. Chan, and C. Liu, "Overview of permanent-magnet brushless drives for electric and hybrid electric vehicles," *IEEE Transactions on Industrial Electronics*, vol. 55, no. 6, pp. 2246–2257, Jun. 2008.

[34] A. Vagati, G. Pellegrino, and P. Guglielmi, "Comparison between SPM and IPM motor drives for EV application," in *2010 International Conference on Electrical Machines (ICEM)*, Sept. 2010, pp. 1–6.

[35] A. M. EL-Refaie, J. P. Alexander, S. Galioto, P. B. Reddy, K. K. Huh, P. de Bock, and X. Shen, "Advanced high-power-density interior permanent magnet motor for traction applications," *IEEE Transactions on Industry Applications*, vol. 50, no. 5, pp. 3235–3248, Sept. 2014.

[36] Z. Q. Zhu and D. Howe, "Electrical machines and drives for electric, hybrid, and fuel cell vehicles," *Proceedings of the IEEE*, vol. 95, no. 4, pp. 746–765, Apr. 2007.

[37] G. Pellegrino, A. Vagati, B. Boazzo, and P. Guglielmi, "Comparison of induction and PM synchronous motor drives for EV application including design examples," *IEEE Transactions on Industrial Applications*, vol. 48, no. 6, pp. 2322–2332, Nov. 2012.

[38] A. Chiba, Y. Takano, M. Takeno, T. Imakawa, N. Hoshi, M. Takemoto, and S. Ogasawara, "Torque density and efficiency improvements of a switched reluctance motor without rare-earth material for hybrid vehicles," *IEEE Transactions on Industry Applications*, vol. 47, no. 3, pp. 1240–1246, May 2011.

[39] K. Kiyota, T. Kakishima, and A. Chiba, "Comparison of test result and design stage prediction of switched reluctance motor competitive with 60-kw rare-earth PM motor," *IEEE Transactions on Industrial Electronics*, vol. 61, no. 10, pp. 5712–5721, Oct. 2014.

[40] K. Kiyota, T. Kakishima, A. Chiba, and M. A. Rahman, "Cylindrical rotor design for acoustic noise and windage loss reduction in switched reluctance motor for hev applications," *IEEE Transactions on Industry Applications*, vol. 52, no. 1, pp. 154–162, Jan. 2016.

[41] T. A. Burress, "Benchmarking state-of-the-art technologies," *2013 U.S. DOE Hydrogen and Fuel Cells Program and Vehicle Technologies Program Annual Merit Review and Peer Evaluation Meeting*, 2013.

[42] T. A. Burress and *et al.*, "Evaluation of the 2008 lexus LS 600h hybrid synergy drive system," Oak Ridge Nat. Lab., Oak Ridge, TN, USA, Tech. Rep. ORNL/TM-2008/185, Jan. 2009.

[43] R. Storn and K. Price, "Differential evolution - a simple and efficient adaptive scheme for global optimization over continuous spaces," in *International Computer Science Institute*, USA, 1995.

[44] U. K. Chakraborty, *Advances in Differential Evolution*. Berlin, Germany: Springer-Verlag, 2008.

[45] R. S. Prado, R. C. P. Silva, F. G. Guimaries, and O. M. Neto, "Using differential evolution for combinatorial optimization: A general approach," in *2010 IEEE International Conference on Systems, Man and Cybernetics*, Oct. 2010, pp. 11–18.

[46] G. Y. Sizov, P. Zhang, D. M. Ionel, N. A. O. Demerdash, and M. Rosu, "Automated multi-objective design optimization of PM AC machines using computationally efficient FEA and differential evolution," *IEEE Transactions on Industry Applications*, vol. 49, no. 5, pp. 2086–2096, Sept. 2013.

[47] D. Zarko, D. Ban, and T. A. Lipo, "Analytical solution for cogging torque in surface permanent-magnet motors using conformal mapping," *IEEE Transactions on Magnetics*, vol. 44, no. 1, pp. 52–65, Jan. 2008.

[48] P. Alotto, "A hybrid multiobjective differential evolution method for electromagnetic device optimization," *COMPEL - The international journal for computation and mathematics in electrical and electronic engineering*, vol. 30, no. 6, pp. 1815–1828, 2011. [Online]. Available: https://doi.org/10.1108/03321641111168129

[49] Rotating Losses in a Surface Mount Permanent Magnet Motor. [Online]. Available: http://www.femm.info/wiki/SPMLoss

[50] D. Ishak, Z. Q. Zhu, and D. Howe, "Eddy-current loss in the rotor magnets of permanent-magnet brushless machines having a fractional number of slots per pole," *IEEE Transactions on Magnetics*, vol. 41, no. 9, pp. 2462–2469, Sept. 2005.

[51] D. H. Miller and A. S. Rubenstein, "Excitation systems for small generators," *Electrical Engineering*, vol. 81, no. 6, pp. 434–440, Jun. 1962.

[52] R. S. Munoz-Aguilar, A. Doria-Cerezo, E. Fossas, and R. Cardoner, "Sliding mode control of a stand-alone wound rotor synchronous generator," *IEEE Transactions on Industrial Electronics*, vol. 58, no. 10, pp. 4888–4897, Oct. 2011.

[53] E. D. Bassett and F. M. Potter, "Capacitive excitation for induction generators," *Electrical Engineering*, vol. 54, no. 5, pp. 540–545, May 1935.

[54] J. M. Elder, J. T. Boys, and J. L. Woodward, "The process of self excitation in induction generators," *IEE Proceedings B - Electric Power Applications*, vol. 130, no. 2, pp. 103–108, Mar. 1983.

[55] M. H. Haque, "A novel method of evaluating performance characteristics of a self-excited induction generator," *IEEE Transactions on Energy Conversion*, vol. 24, no. 2, pp. 358–365, Jun. 2009.

[56] O. Ojo, "Minimum airgap flux linkage requirement for self-excitation in stand-alone induction generators," *IEEE Transactions on Energy Conversion*, vol. 10, no. 3, pp. 484–492, Sept. 1995.

[57] S. S. Murthy, O. P. Malik, and A. K. Tandon, "Analysis of self-excited induction generators," *IEE Proceedings C - Generation, Transmission and Distribution*, vol. 129, no. 6, pp. 260–265, Nov. 1982.

[58] R. C. Bansal, "Three-phase self-excited induction generators: an overview," *IEEE Transactions on Energy Conversion*, vol. 20, no. 2, pp. 292–299, Jun. 2005.

[59] F. E. Abdel-Kader, "The reluctance machine as a self-excited reluctance generator," *Electric Machines and Power Systems*, vol. 10, no. 2-3, pp. 141–148, 1985.

[60] A. I. Alolah, "Steady-state operating limits of three-phase self-excited reluctance generator," *IEE Proceedings C - Generation, Transmission and Distribution*, vol. 139, no. 3, pp. 261–268, May 1992.

[61] S. M. Allam, M. A. El-Khazendar, and A. M. Osheiba, "Steady-state analysis of a self-excited single-phase reluctance generator," *IEEE Transactions on Energy Conversion*, vol. 22, no. 3, pp. 584–591, Sept. 2007.

[62] Y. H. A. Rahim, A. L. Mohamadien, and A. S. A. Khalaf, "Comparison between the steady-state performance of self-excited reluctance and induction generators," *IEEE Transactions on Energy Conversion*, vol. 5, no. 3, pp. 519–525, Sept. 1990.

[63] T. F. Chan, "Steady-state analysis of a three-phase self-excited reluctance generator," *IEEE Transactions on Energy Conversion*, vol. 7, no. 1, pp. 223–230, Mar. 1992.

[64] A. L. Mohamadein, Y. H. A. Rahim, and A. S. Al-khalaf, "Steady-state performance of self-excited reluctance generators," *IEE Proceedings B - Electric Power Applications*, vol. 137, no. 5, pp. 293–298, Sept. 1990.

[65] A. I. Alolah, "Capacitance requirements for three phase self-excited reluctance generators," *IEE Proceedings C - Generation, Transmission and Distribution*, vol. 138, no. 3, pp. 193–198, May 1991.

[66] L. Wang and Y.-S. Wang, "Characteristics of a self-excited reluctance generator as affected by sudden connection of an induction motor load," in *1998 International Conference on Power System Technology*, vol. 1, Beijing, China, Aug. 1998, pp. 605–609.

[67] ——, "Dynamic performance and minimum loading effects of an isolated self-excited reluctance generator," in *IEEE Power Engineering Society 1999 Winter Meeting*, vol. 1, New York, NY, USA, Jan. 1999, pp. 13–18.

[68] Y. H. A. Rahim, J. E. Fletcher, and N. E. A. M. Hassanain, "Performance analysis of salient-pole self-excited reluctance generators using a simplified model," *IET Renewable Power Generation*, vol. 4, no. 3, pp. 253–260, May 2010.

[69] L. Xu, X. Xu, T. A. Lipo, and D. W. Novotny, "Vector control of a synchronous reluctance motor including saturation and iron loss," *IEEE Transactions on Industry Applications*, vol. 27, no. 5, pp. 977–985, Sept. 1991.

[70] T. Lubin, H. Razik, and A. Rezzoug, "Magnetic saturation effects on the control of a synchronous reluctance machine," *IEEE Transactions on Energy Conversion*, vol. 17, no. 3, pp. 356–362, Sept. 2002.

[71] A. Vagati, M. Pastorelli, F. Scapino, and G. Franceschini, "Impact of cross saturation in synchronous reluctance motors of the transverse-laminated type," *IEEE Transactions on Industry Applications*, vol. 36, no. 4, pp. 1039–1046, Jul. 2000.

[72] P. Guglielmi, M. Pastorelli, and A. Vagati, "Impact of cross-saturation in sensorless control of transverse-laminated synchronous reluctance motors," *IEEE Transactions on Industrial Electronics*, vol. 53, no. 2, pp. 429–439, Apr. 2006.

[73] S. Guha and N. C. Kar, "Alinearized model of saturated self-excited synchronous reluctance generator," in *2005 Canadian Conference on Electrical and Computer Engineering*, May 2005, pp. 633–636.

[74] ——, "Saturation modeling and stability analysis of synchronous reluctance generator," *IEEE Transactions on Energy Conversion*, vol. 23, no. 3, pp. 814–823, Sept. 2008.

[75] A. S. O. Ogunjuyigbe, T. R. Ayodele, B. B. Adetokun, and A. A. Jimoh, "Dynamic performance of wind-driven self-excited reluctance generator under varying wind speed and load," in *2016 IEEE International Conference on Renewable Energy Research and Applications (ICRERA)*, Nov. 2016, pp. 506–511.

[76] D. M. Eggleston and F. S. Stoddard, *Wind Turbine Engineering Design*. New York: Van Nostrand Reinhold Co., 1987.

[77] S. Heier, *Grid integration of wind energy conversion systems*, John Wiley & Sons Ltd, Ed., 1998.

List of Acronyms

2D	two-dimensional
ALA	axially-laminated anisotropy
CPSR	constant power speed range
DE	differential evolution
EMF	electromagnetic force
EV	electric vehicle
FEA	finite element analysis
FW	flux weakening
HEV	hybrid electric vehicle
IM	induction machine
IPM	interior permanent magnet
MMF	magneto motive force
MPPT	maximum power point tracking
MTPA	maximum torque–per–Ampere
MTPV	maximum torque–per–Voltage
PF	power factor
PM	permanent magnet
PMAREL	PM-assisted reluctance
PQ	active and reactive power
REL	synchronous reluctance
SEIG	self-excited induction generator
SERG	self-excited synchronous reluctance generators
SP	salient-pole
SRM	switched reluctance machine
TLA	transversely-laminated anisotropy

Acknowledgments

Finally, I should say "Time flies". I still clearly remember the first day I came to Italy, and the first time I met with my supervisor Prof. Bianchi. But now, I am going to finish the Ph.D. and leave Italy.

Firstly, I would like to express my deepest gratitude to Prof. Nicola Bianchi, for his kind help throughout my doctoral period. He keeps an optimistic and enthusiastic attitude towards both life and research. His profound thinking and abundant theoretical knowledge impress me a lot. I am sincerely grateful to him for being a supervisor not only in machine design, but also in life.

I am really lucky to spend my doctoral period at the Electric Drive Laboratory (EDLab). It has been a wonderful and unforgettable experience here. I would also like to thank Prof. Silverio Bolognani, who is always dressy but humorous, and Prof. Luigi Alberti. I am gratefully to all the past and present members in the lab, among them are Mosè, Mattia, Hanafy (from Egypt), Damiano, Mahmoud (from Egypt), Davide, Virginia, Cristian, Matteo, Emanuel, Grazia, Diego, Qian (from China), Carlos (from Spain), Ladislav (from Czech Republic), Daniele and so on. I should specially thank Giacomo Bacco and Francesco Toso, for their help on my research.

I would also like to thank my Master supervisor Prof. Ronghai Qu, for his concern about my study abroad. Thanks to China Scholarship Council for their financial support.

Lastly, but definitely not the least, I am grateful to my parents. They have been always with me, and support me continuously during my studies. I will love them forever.

Padova, 30 Sept. 2018 Yawei Wang

This Thesis is written in LaTeX.